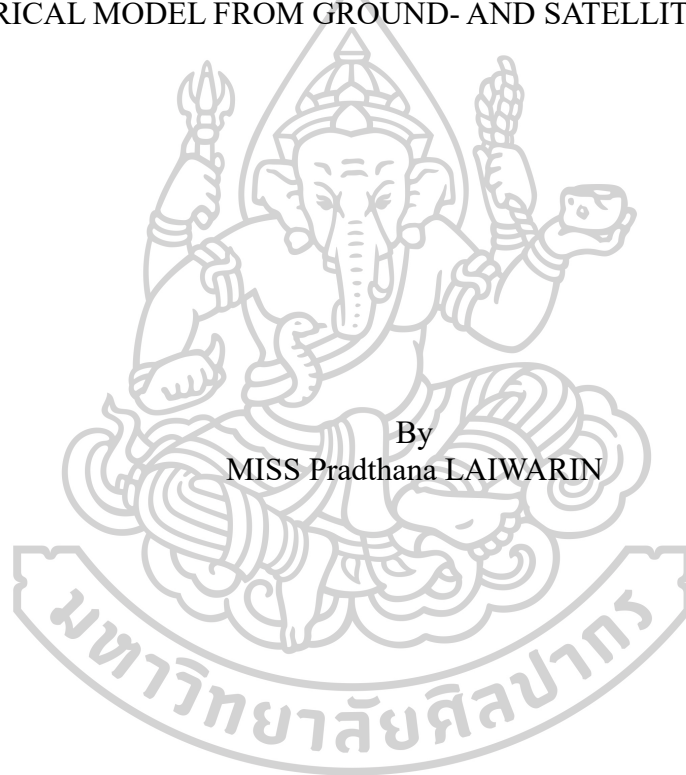




DEVELOPMENT OF MONTHLY AVERAGE HOURLY MAPS OF VITAMIN D
WEIGHTED SOLAR ULTRAVIOLET RADIATION FOR THAILAND USING AN
EMPIRICAL MODEL FROM GROUND- AND SATELLITE-BASED DATA



By
MISS Pradthana LAIWARIN

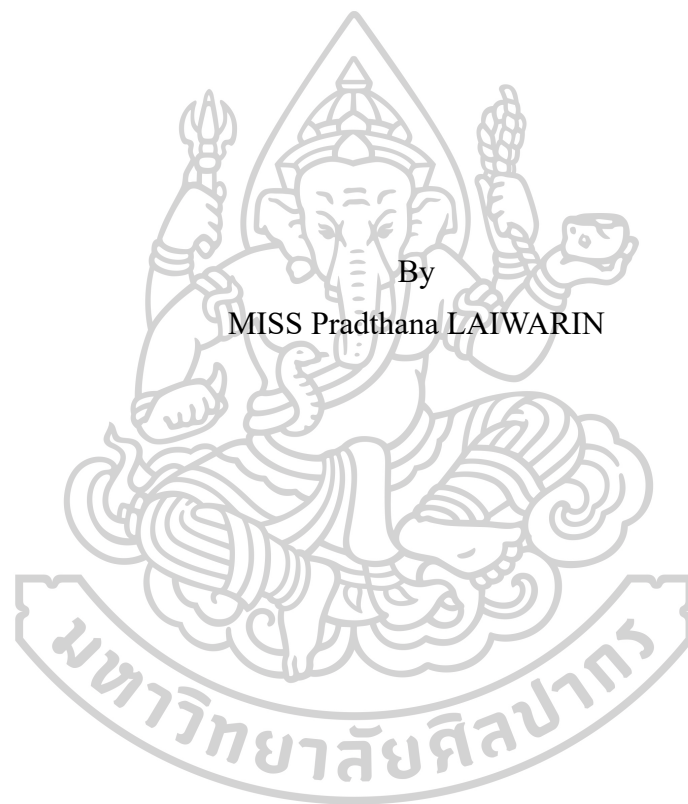
A Thesis Submitted in Partial Fulfillment of the Requirements
for Doctor of Philosophy PHYSICS
Department of PHYSICS
Silpakorn University
Academic Year 2022
Copyright of Silpakorn University

การพัฒนาแผนที่รายชั่วโมงเฉลี่ยต่อเดือนของความเข้มข้นสีอัลตราไวโอเล็ตจากดวงอาทิตย์ที่ช่วยสร้างวิตามินดีของมนุษย์สำหรับประเทศไทยโดยใช้แบบจำลองเอ็มไพริคัลจากข้อมูลภาคพื้นดินและข้อมูลดาวเทียม



วิทยานิพนธ์นี้เป็นส่วนหนึ่งของการศึกษาตามหลักสูตรปรัชญาดุษฎีบัณฑิต
สาขาวิชาฟิสิกส์ แบบ 1.1 ปรัชญาดุษฎีบัณฑิต
ภาควิชาฟิสิกส์
มหาวิทยาลัยศิลปากร
ปีการศึกษา 2565
ลิขสิทธิ์ของมหาวิทยาลัยศิลปากร

DEVELOPMENT OF MONTHLY AVERAGE HOURLY MAPS OF
VITAMIN D WEIGHTED SOLAR ULTRAVIOLET RADIATION FOR
THAILAND USING AN EMPIRICAL MODEL FROM GROUND-
AND SATELLITE-BASED DATA



By
MISS Pradthana LAIWARIN

A Thesis Submitted in Partial Fulfillment of the Requirements
for Doctor of Philosophy PHYSICS
Department of PHYSICS
Silpakorn University
Academic Year 2022
Copyright of Silpakorn University

Title Development of monthly average hourly maps of vitamin D
 weighted solar ultraviolet radiation for Thailand using an empirical
 model from ground- and satellite-based data
By MISS Pradthana LAIWARIN
Field of Study PHYSICS
Advisor Assistant Professor Dr. Sumaman Buntoung
Co advisor Professor Dr. Serm Janjai

Faculty of Science, Silpakorn University in Partial Fulfillment of the
Requirements for the Doctor of Philosophy

.....Dean of Faculty of Science
(Assistant Professor Dr. Narong Chimpalee)

Approved by

.....Chair person
(Assistant Professor Dr. Pranomkorn Choosri)

.....Advisor
(Assistant Professor Dr. Sumaman Buntoung)

.....Co advisor
(Professor Dr. Serm Janjai)

.....Committee
(Assistant Professor Dr. Rungrat Wattan)

.....Committee
(Assistant Professor Dr. Itsara Masiri)

630730003 : Major PHYSICS

Keyword : solar ultraviolet radiation, vitamin D weighted, empirical model, map

MISS Pradthana LAIWARIN : Development of monthly average hourly maps of vitamin D weighted solar ultraviolet radiation for Thailand using an empirical model from ground- and satellite-based data Thesis advisor : Assistant Professor Dr. Sumaman Buntoung

This thesis presents the development of maps of monthly average hourly vitamin D weighted solar ultraviolet radiation (DUV) for Thailand using an empirical model from ground- and satellite-based data. Spectral solar ultraviolet radiation measured by a spectrophotometer model DMc150 of Bentham Instruments installed at a roof top of Science building at Silpakorn University, Nakhon Pathom (13.82 °N, 100.04 °E) in years 2014 and 2016 were used to find a relationship between DUV and erythemal solar ultraviolet radiation (EUV). Broadband radiometers model 501A of Solar Light company installed at four stations namely, Chiang Mai (18.78 °N, 98.98 °E), Ubon Ratchathani (15.25 °N, 104.87 °E), Nakhon Pathom (13.82 °N, 100.04 °E), and Songkhla (7.20 °N, 100.60 °E) were used to measure EUV and then these values were converted to DUV using the relationship between DUV and EUV produced from the data at Nakhon Pathom station. The DUV data obtained from the radiometers at the four stations during 2014-2018 were used for modelling and validation processes. Another ground-based input data is visibility obtained from observation at 125 meteorological stations in Thailand. The visibility data was converted to aerosol optical depth. Satellite-based input data used in this thesis consist of a satellite-derived cloud index from MTSAT-2 and Himawari-8 satellites, and total ozone column from OMI/AURA satellite. In addition, solar zenith angle, air mass, and extraterrestrial DUV irradiance were also calculated. These input data were collected during 2012-2021, and were interpolated to obtain the data as grids covering the region of Thailand. An empirical model for estimating monthly average hourly DUV irradiance using the data from the four UV monitoring stations during 2014-2016 was developed as a function of aerosol, cloud index, ozone, solar zenith angle, air mass, and extraterrestrial DUV irradiance. The model was validated by calculating DUV irradiance using the proposed model and compared the values obtained from this model with those obtained from the ground-based measurement during 2017-2018. The difference between DUV irradiances estimated from the proposed model and those obtained from the measurement was presented in terms of root mean square difference (RMSD) and mean bias difference (MBD). The RMSD and MBD were found to be 12.7% and -0.2%, respectively. Afterward, this model was used to estimate monthly average hourly DUV irradiance covering the region of Thailand during 2012-2021. The result was presented as maps and these maps show diurnal, seasonal and geographical variations of DUV irradiance.

ACKNOWLEDGEMENTS

I would like to thank Thailand Science Research and Innovation (TSRI) National Science, Research and Innovation Fund (NSRF) (Fiscal Year 2022) for financial supporting this research.

I would like to thank Asst. Prof. Dr.Sumaman Buntoung, my main supervisor, from the bottom of my heart for advice, knowledge, caring, kindness, collaboration, patience, and her brilliance. She is like a mother. It gives me the strength to do research and study.

I would like to thank Prof. Dr.Serm Janjai, my assistant supervisor for advice, assistance, and impulsion throughout this difficult work.

I would like to thank Asst. Prof. Dr.Itsara Masiri and Asst. Prof. Dr.Somjet Pattarapanitchai for their expert advice and help about mapping and programming until this work was successful.

I appreciate my thesis committees: Asst. Prof. Dr.Rungrat Wattan and Asst. Prof. Dr.Pronomkorn Choosri taking the time to provide the great suggestions.

I also would like to thank all researchers in the Tropical Atmospheric Physics Research Laboratory of Silpakorn University for help everything.

Finally, I wish to thank my family especially mother and my sister including friends for their encouragement, friendship, and supporting throughout my life.

MISS Pradthana LAIWARIN

TABLE OF CONTENTS

	Page
ABSTRACT.....	D
ACKNOWLEDGEMENTS.....	E
TABLE OF CONTENTS.....	F
List of tables.....	H
List of figures.....	I
Chapter 1.....	1
Introduction.....	1
1.1 Rationale.....	1
1.2 Objectives.....	2
1.3 Organization of this thesis.....	2
Chapter 2.....	3
Theory and Literature Reviews.....	3
2.1 Solar ultraviolet radiation.....	3
2.2 Parameters affecting solar ultraviolet radiation.....	4
2.2.1 Solar zenith angle.....	4
2.2.2 Cloud.....	6
2.2.3 Ozone.....	6
2.2.4 Aerosol.....	7
2.2.5 Altitude and air mass.....	8
2.3 Measurement of ultraviolet radiation.....	10
2.3.1 Ground-based measurement.....	10
2.3.2 Satellite-based measurement.....	12
2.4 Effects of solar ultraviolet radiation on human health.....	15
2.5 Literature reviews on the UV from the measurement and UV mapping from satellite data.....	19
Chapter 3.....	25

Methodology, Result and Discussion.....	25
3.1 Measurement.....	25
3.2 Empirical model for estimating solar ultraviolet radiation for vitamin D synthesis	47
3.3 Validation of the empirical model for estimating solar ultraviolet radiation for vitamin D synthesis	49
3.4 Processing of satellite data from MTSAT and Himawari-8 satellites.....	52
3.5 Maps of monthly average hourly solar ultraviolet radiation for vitamin D synthesis	54
Chapter 4.....	58
Conclusion	58
Appendix 1.....	59
A model for estimating solar ultraviolet radiation for vitamin D photosynthesis at Nakhon Pathom.....	59
Appendix 2.....	65
Solar ultraviolet radiation for psoriasis treatment at Nakhon Pathom province.....	65
Appendix 3.....	73
Development of empirical models for calculating global and diffuse erythemal weighted solar ultraviolet radiation under clear sky conditions in Thailand.....	73
Appendix 4.....	82
Accurate surface ultraviolet radiation forecasting for clinical application with deep neural network	82
REFERENCES	100
VITA	106

List of tables

	Page
Table 1 Advanced Himawari-8 imager.	40
Table 2 The coefficient values and statistic values.	48



List of figures

	Page
Figure 1 Solar radiation spectrum and absorption of gases in the atmosphere (adapted from Wu, 2018).	4
Figure 2 Schematic diagram of solar zenith angle (adapted from Zhang et al., 2021)..4	4
Figure 3 The formation and the depletion of ozone.	7
Figure 4 The relation between altitude and pressure (adapted from Lalic et al., 2018).8	8
Figure 5 The path length when the sun is at the zenith (Z) and path length when the sun is at the actual position (S) (adapted from Iqbal, 1983).	9
Figure 6 The UV spectroradiometer model DMc150 of Bentham Instruments Ltd. at Silpakorn University, Nakhon Pathom a) input optics of the UV spectroradiometer and b) spectroradiometer.	11
Figure 7 The broadband UV radiometer model 501A of Solar Light company at Silpakorn University, Nakhon Pathom.	11
Figure 8 The multi-channel filter UV radiometer model GUV-2511 of Biospherical Instruments company at Silpakorn University, Nakhon Pathom.	12
Figure 9 The polar orbiting satellite (adapted from Panwar, 2021).	13
Figure 10 An example of erythemal dose rate from AURA satellite (adapted from Earthdata, 2006).	13
Figure 11 The geostationary satellite (adapted from Panwar, 2021).	14
Figure 12 Coverage areas for geostationary satellites (adapted from Ceamanos et al., 2021).	14
Figure 13 An example cloud free vitamin D UV dose from Meteosat satellite (adapted from TEMIS, 2023).	15
Figure 14 The ultraviolet radiation can cause erythema (adapted from Barber, 2011).	16
Figure 15 Action spectrum for erythema in human skin (adapted from McKinlay & Diffey, 1987).	16
Figure 16 The vitamin D synthesis from sun exposure (adapted from Lucas et al., 2014).	17

Figure 17 Action spectrum for the production of previtamin D ₃ in human skin (adapted from Terenetskaya et al., 2006).	18
Figure 18 The phototherapy of psoriasis.....	18
Figure 19 Action spectrum for phototherapy of psoriasis (adapted from Krzyścin et al., 2012).	19
Figure 20 The spectroradiometer model DMc150 of Bentham Instruments company at the roof top of Science building at Silpakorn University in Nakhon Pathom (a) sensor and (b) control box.....	26
Figure 21 The computer display of BenWin+.....	26
Figure 22 The location of four stations.....	32
Figure 23 Broadband UV radiometer model 501A of Solar Light company at Chiang Mai station.	32
Figure 24 Broadband UV radiometer model 501A of Solar Light company at Nakhon Pathom station.....	33
Figure 25 Broadband UV radiometer model 501A of Solar Light company at Ubon Ratchathani station.....	33
Figure 26 Broadband UV radiometer model 501A of Solar Light company at Songkhla station.....	34
Figure 27 The datalogger model DX2000 of YOKOGAWA company.....	34
Figure 28 The comparison between the solar ultraviolet radiation for vitamin D synthesis from the model (DUVmodel) and that from the measurement (DUVmeas).36	
Figure 29 The relationship between DUV and EUV using the radiative transfer model.	37
Figure 30 Locations of 125 meteorological stations and the four UV monitoring stations.	39
Figure 31 The MTSAT-2 (Multi-Function Transport Satellite).	40
Figure 32 The Himawari-8 satellite.	41
Figure 33 The calibration table of MTSAT-2 satellite showing a relation between the pseudo reflectivity (ρ SAT) and gray level.....	42
Figure 34 The calibration table of Himawari-8 satellite showing a relation between the pseudo reflectivity (ρ SAT) and gray level.....	42
Figure 35 Image of the cloud index.	44

Figure 36 Example of the variation of cloud index at Nakhon Pathom station in 2016.	44
Figure 37 The Ozone Monitoring Instrument (OMI) onboard AURA satellite.	45
Figure 38 Example of the seasonal variation of ozone at Nakhon Pathom station in 2016.....	46
Figure 39 The variation of the eccentricity correction factor (E0) in a year.....	47
Figure 40 Comparison of the DUV from the measurement (DUVmeas) and the DUV from the model (DUVmodel) at Chiang Mai station.....	49
Figure 41 Comparison of the DUV from the measurement (DUVmeas) and the DUV from the model (DUVmodel) at Nakhon Pathom station.....	50
Figure 42 Comparison of the DUV from the measurement (DUVmeas) and the DUV from the model (DUVmodel) at Ubon Ratchathani station.....	50
Figure 43 Comparison of the DUV from the measurement (DUVmeas) and the DUV from the model (DUVmodel) at Songkhla station.	51
Figure 44 Comparison of the DUV from the measurement (DUVmeas) and the DUV from the model (DUVmodel) at the four stations.	51
Figure 45 Satellite image in satellite projection.	52
Figure 46 Satellite image in cylindrical projection.....	53
Figure 47 Coordinated satellite image.	53
Figure 48 Spatial distribution maps of long-term monthly average hourly vitamin D	55
Figure 49 Spatial distribution maps of long-term monthly average hourly vitamin D weighted UV irradiance from 8:30-16:30 local time during July to December.....	56

Chapter 1

Introduction

1.1 Rationale

Solar ultraviolet (UV) radiation is an electromagnetic spectrum from the sun. The band is 100-400 nm. This band can be divided into three parts namely ultraviolet-C (UVC, 100-280 nm), ultraviolet-B (UVB, 280-315 nm), and ultraviolet-A (UVA, 315-400 nm) (Barbero et al., 2006). However, all UVC and most UVB are absorbed by the earth's atmosphere. Therefore, a small part of UVB and most part of UVA reach the earth's surface (Oh et al., 2019). Solar UV radiation that reaches the surface is changed by atmospheric components such as ozone, clouds, aerosols, and air molecules. In addition, solar UV radiation also depends on altitudes of locations, and solar zenith angle (Liu et al., 2017).

Solar UV radiation has both positive and negative effects on humans. For positive effects, solar UV radiation can stimulate skin to produce vitamin D when the human body receives sufficient solar UV radiation (Siani et al., 2013) and it can use for treatment of psoriasis (Hönigsmann, 2001). However, for negative effects, when human body receives a large amount of solar UV radiation, it can cause sunburn, skin cancer, and eye cataracts (Lui et al., 2017).

The information of solar UV radiation at the earth's surface is important because it helps people to estimate their exposure times to obtain enough solar UV radiation and to protect their bodies from the sun. Therefore, researchers from many countries have studied the effects of solar UV radiation such as in Spain, New Zealand, and France (Barbero et al., 2006; Brogniez et al., 2021; McKenzie et al., 2003). For Thailand, studying on solar erythematous ultraviolet radiation which affects redness of skin and solar ultraviolet radiation for psoriasis treatment have been already reported (Buntoung et al., 2014; Buntoung et al., 2022).

The stimulation of vitamin D production in Thailand has not been studied yet. Therefore, to fill the research gap, this work is interested in studying the solar UV radiation for vitamin D production. The work aims to develop and validate an empirical model for calculating the solar UV radiation for vitamin D synthesis from

ground-based and satellite-based data. The solar UV radiation obtained from the proposed model are provided as monthly average hourly maps.

1.2 Objectives

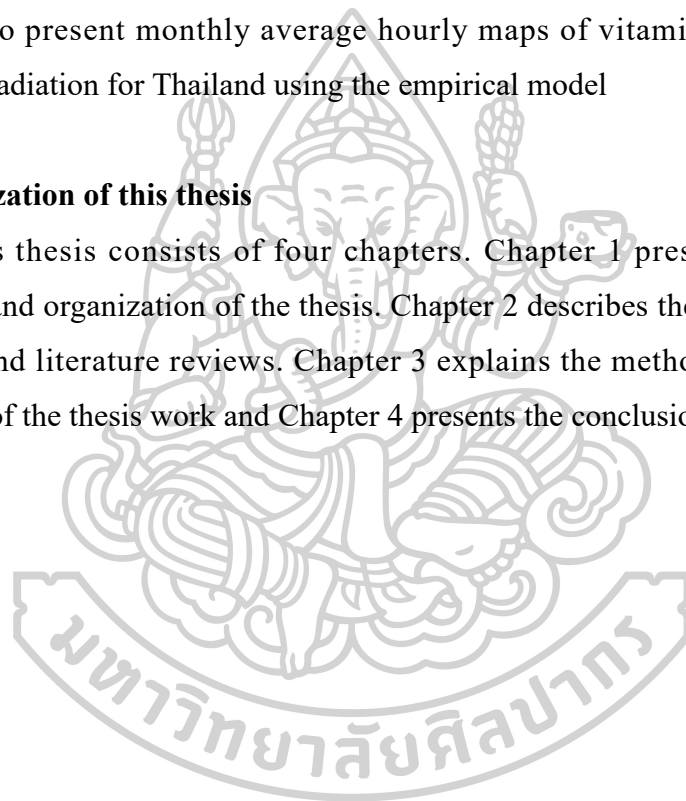
1) To develop an empirical model for estimating solar ultraviolet radiation for vitamin D synthesis in Thailand from ground- and satellite-based data

2) To validate the empirical model for estimating solar ultraviolet radiation for vitamin D synthesis

3) To present monthly average hourly maps of vitamin D weighted solar ultraviolet radiation for Thailand using the empirical model

1.3 Organization of this thesis

This thesis consists of four chapters. Chapter 1 presents the rationale, objectives and organization of the thesis. Chapter 2 describes the theory of solar UV radiation and literature reviews. Chapter 3 explains the methodology, results and discussion of the thesis work and Chapter 4 presents the conclusion of the thesis.



Chapter 2

Theory and Literature Reviews

This chapter presents the theory about solar ultraviolet radiation, parameters affecting solar ultraviolet radiation, measurement of solar ultraviolet radiation, effects of solar ultraviolet radiation on human health and literature reviews on solar ultraviolet radiation. The details are as follows.

2.1 Solar ultraviolet radiation

Extraterrestrial solar radiation is the radiation at the top of the earth's atmosphere. It consists of gamma ray, X-ray, ultraviolet radiation, visible light, infrared radiation, microwave, and radio wave (Waikato, 2018). When solar radiation enters the earth's atmosphere, it will be absorbed and scattered by compositions of the atmosphere. Therefore, the solar radiation is attenuated and only some parts of solar radiation can pass through the atmosphere to the earth's surface. The solar radiation that can reach the surface are ultraviolet radiation, visible light, and infrared radiation (GrassrootsHealth, 2021) (Figure 1).

The shortest wavelength and the highest energy of solar radiation at the earth's surface is ultraviolet (UV) radiation (Waikato, 2007). Usually, solar UV radiation has wavelength between 100 and 400 nm which can be divided into three ranges. These are ultraviolet-C (UVC), ultraviolet-B (UVB) and ultraviolet-A (UVA). UVC is in wavelength range of 100-280 nm, UVB is from 280-315 nm, and UVA ranges from 315-400 nm (Barbero et al., 2006). However, only some parts of UVB and most of UVA reach the surface because UVC and most of UVB are absorbed by the earth's atmosphere (FDA, 2020).

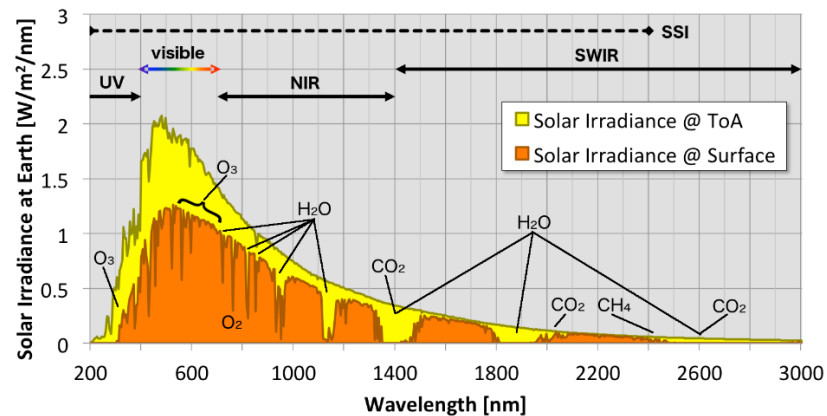


Figure 1 Solar radiation spectrum and absorption of gases in the atmosphere (adapted from Wu, 2018).

2.2 Parameters affecting solar ultraviolet radiation

Parameters that mainly affect solar UV radiation are solar zenith angle, cloud, ozone, aerosol, altitude, and air mass. The details of these parameters are described as follows.

2.2.1 Solar zenith angle

Solar zenith angle (θ_z) is the angle between the direction of rays from the sun and the vertical (zenith) direction (Figure 2). It affects solar path length and thus causes different radiation attenuation. Solar zenith angle depends on latitude, the day of the year, and time (Iqbal, 1983).

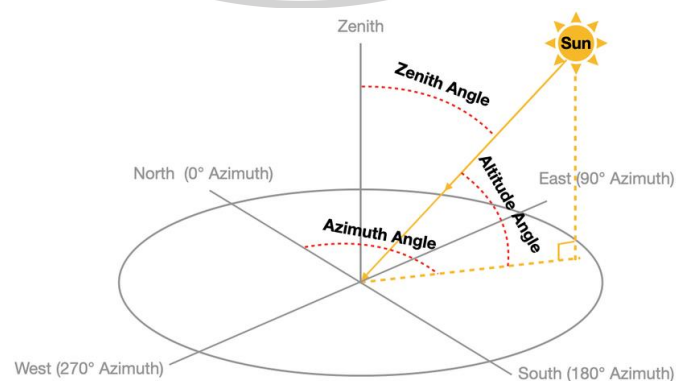


Figure 2 Schematic diagram of solar zenith angle (adapted from Zhang et al., 2021).

It can be calculated following Eq. (2.1).

$$\cos\theta_z = \sin\phi\sin\delta + \cos\phi\cos\delta\cos\omega \quad (2.1)$$

where θ_z = the solar zenith angle (degree)
 ϕ = the latitude (degree)
 δ = the solar declination (degree)
 ω = the hour angle (degree).

The solar declination has variation according to day angle (Γ) depending on the day of the year (d_n), and it can be calculated following Eq. (2.2).

$$\delta = (0.006918 - 0.399912\cos\Gamma + 0.070257\sin\Gamma - 0.006758\cos2\Gamma + 0.000907\sin2\Gamma - 0.002697\cos3\Gamma + 0.00148\sin3\Gamma)\left(\frac{180}{\pi}\right) \quad (2.2)$$

where Γ = day angle (radian).

The day angle can be calculated from Eq. (2.3).

$$\Gamma = 2\pi(d_n - 1)/365 \quad (2.3)$$

where d_n = day of the year (-).

The hour angle can be calculated from solar time (ST) following Eq. (2.4).

$$\omega = 15(12 - ST) \quad (2.4)$$

where ST = solar time (hour).

The solar time can be calculated from Eq. (2.5).

$$ST = LST + 4(L_s - L_{loc})/60 + E_t/60 \quad (2.5)$$

where LST = the local standard time (hour)

L_s = the standard longitude (degree)

L_{loc} = the local longitude (degree)

E_t = the equation of time (minute) which is the difference between solar time and mean solar time, that can be calculated from Eq. (2.6).

$$E_t = 229.18(0.000075 + 0.001868\cos\Gamma - 0.032077\sin\Gamma - 0.014615\cos 2\Gamma - 0.04089\sin 2\Gamma) \quad (2.6)$$

2.2.2 Cloud

Cloud is droplet in the atmosphere that can be in forms of water droplets, ice crystals, and semi solid and liquid (Costa et al., 2017). Its spatial distribution and vertical extent are different in different locations (Garcia et al., 2008). Cloud can attenuate solar radiation by reflection, refraction, absorption, and scattering processes (Lightle, 2008; Stopelli et al., 2015; Tzoumanikas et al., 2016). It can both enhance and deplete solar radiation (Feister et al., 2015; NOAA, 2023). Most of the ability to attenuation is expressed in terms of cloud optical thickness (COT) that depends on types of cloud that the solar radiation passes (Dissanayake et al., 2001). Generally, cloud in liquid water form can reflect the solar radiation more than cloud in solid form (CarbonBrief, 2020), and the solar radiation will decrease when cloud increases (Matuszko, 2012). In addition, solar radiation also inversely varies with size of droplet and crystals in cloud (Ewald et al., 2019). Moreover, cloud can attenuate and transmit differently radiation in different wavelengths (Schlundt et al., 2011).

2.2.3 Ozone

Ozone (O_3) is combination of oxygen molecule (O_2) and atom of oxygen (O) that are quite a few but ozone has advantages as it helps maintain balance in the atmosphere (eia, 2022). Ozone is mainly in the stratosphere which has an influence

obviously on absorption of solar ultraviolet radiation especially all UVC and parts of UVB that affect human health (EPA, 2021). For ozone formation, when oxygen molecule receives the solar ultraviolet radiation, oxygen molecule can be divided into two atoms of oxygen and the atom of oxygen can interact with other oxygen molecule to form ozone molecule in the atmosphere. For ozone depletion, the solar ultraviolet radiation will break up bonds of ozone into atoms of oxygen and oxygen molecule (Chapman, 1930). These processes are shown in Figure 3.

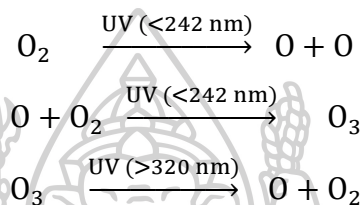


Figure 3 The formation and the depletion of ozone.

2.2.4 Aerosol

Aerosol is solid or liquid particles in the atmosphere such as dust, smoke and pollution (Kumar et al., 2007). Aerosol is an atmospheric factor affecting the solar radiation by absorption and scattering (Li et al., 2022). This depends on types of aerosols resulting from its source (Kolhe et al., 2022). Effects of aerosol can indicate with aerosol optical depth (AOD) which is a function of Angstrom's turbidity coefficient (β , unless unit) representing amount of aerosol, and Angstrom's wavelength exponent (α , unless unit) representing magnitude or density of aerosol (Iqbal, 1983). Aerosol optical depth can be calculated using Eq. (2.7) which depends on wavelength (Kaskaoutis & Kambezidis, 2006).

$$\text{AOD} = \beta \lambda^{-\alpha} \quad (2.7)$$

where AOD = the aerosol optical depth (-)

λ = the wavelength (μm)

β = Angstrom's turbidity coefficient (-)

α = Angstrom's wavelength exponent (-).

2.2.5 Altitude and air mass

Altitude (z) is the height of a point in the atmosphere above mean sea level. Higher altitude will have lower pressure than lower altitude because air pressure or number of air molecules decreases as altitude increases (Figure 4). When the solar radiation passes gas molecules and air molecules known as air mass (m_a , unitless) in the atmosphere, it can reduce depending on quantity of air molecules and path length.

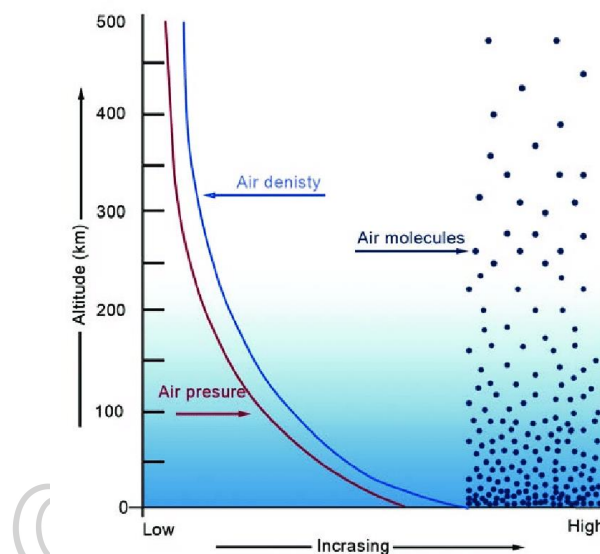


Figure 4 The relation between altitude and pressure (adapted from Lalic et al., 2018).

To indicate air column, relative air mass (m_r , unitless) is generally used, which can consider as a ratio between path length when the sun is at the zenith ($m_{act,v}$) and path length when the sun is at the actual position ($m_{act,s}$) as shown in Figure 5.

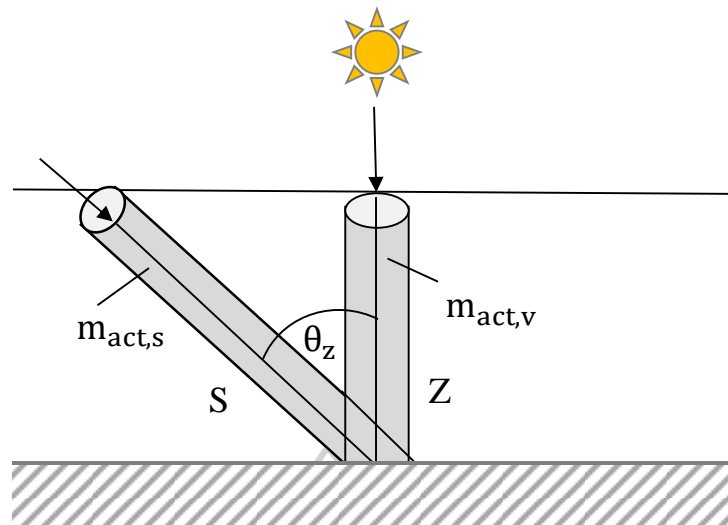


Figure 5 The path length when the sun is at the zenith (Z) and path length when the sun is at the actual position (S) (adapted from Iqbal, 1983).

Due to the relative air mass indicates air mass at mean sea level (101.325 kPa), the air mass (m_a) at a height above mean sea level can be calculated using the following equation of Iqbal (1983).

$$m_a = m_r \left(\frac{P}{101.325} \right) \quad (2.8)$$

where m_a = the air mass (-)
 m_r = the relative air mass (-)
 P = the atmospheric pressure (kPa).

The relative air mass can be calculated from an equation presented by Kasten (1965).

$$m_r = [\cos\theta_z + 0.15(93.885 - \theta_z)^{-1.253}]^{-1} \quad (2.9)$$

where θ_z = the solar zenith angle (degree).

The atmospheric pressure can be obtained from an equation presented by Lunde (1980).

$$\frac{P}{P_0} = \exp(-0.0001184z) \quad (2.10)$$

where P = the atmospheric pressure (kPa)
 P_0 = the standard pressure (101.325 kPa)
 z = the altitude (m).

2.3 Measurement of ultraviolet radiation

UV measurements can be performed directly using ground-based instruments and can be measured indirectly using satellite-based instruments as the following details.

2.3.1 Ground-based measurement

There are three main types of ground-based measurements. These instruments are installed in the fields to continuously measure solar ultraviolet radiation. The details of these instruments are described as follows.

1) UV spectroradiometer

It measures UV radiation at each wavelength. The operating principles are as follows. The solar radiation is received by sensor. Afterward, monochromator will select the ray into narrow bands of wavelengths and these wavelengths are controlled by a controller. An example of the spectroradiometer is shown in Figure 6.

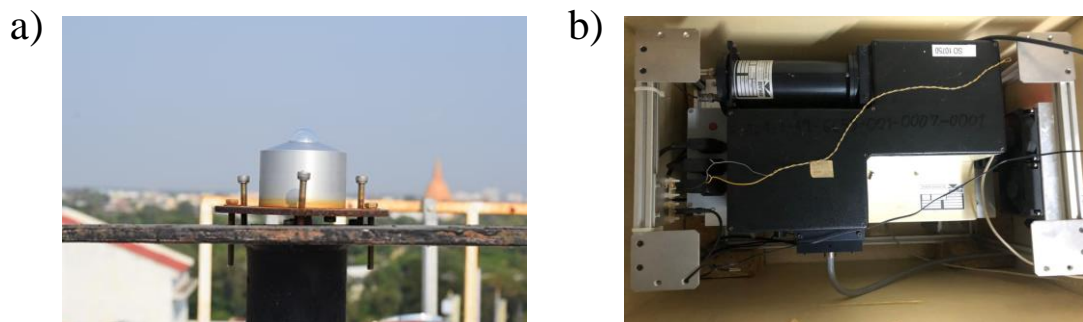


Figure 6 The UV spectroradiometer model DMc150 of Bentham Instruments Ltd. at Silpakorn University, Nakhon Pathom a) input optics of the UV spectroradiometer and b) spectroradiometer.

2) Broadband UV radiometer

It measures broadband UV radiation and it consists of quartz dome, receiver, filter, detector, and amplifier. The solar radiation passes through the glass dome into the receiver and the filter that responds the UV radiation. The detector will measure the UV radiation and the amplifier will amplify the signal to voltage value. An example of broadband UV radiometer is presented in Figure 7.

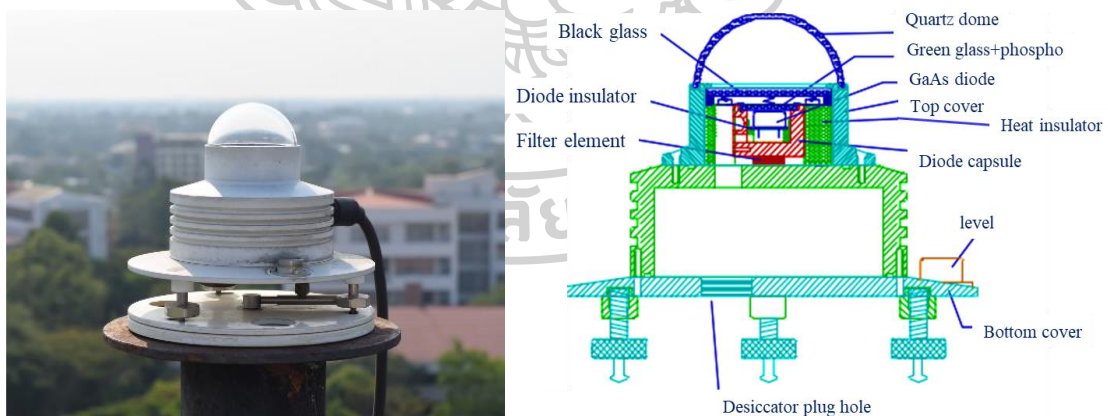


Figure 7 The broadband UV radiometer model 501A of Solar Light company at Silpakorn University, Nakhon Pathom.

3) Multi-channel filter UV radiometer

It measures some wavelengths in UV radiation such as 305, 313, 320, 340, 380 and 395 nm with the band width of about 10 nm. The instrument consists of diffuser, filter, detector, and controller. Data from this instrument can be also used to calculate UVA, UVB, erythemal irradiance, UV Index, and total ozone. An example of multi-channel filter UV radiometer is shown in Figure 8.

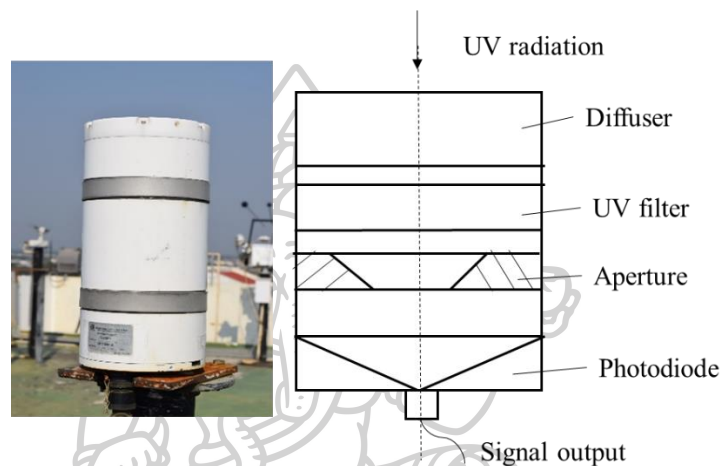


Figure 8 The multi-channel filter UV radiometer model GUV-2511 of Biospherical Instruments company at Silpakorn University, Nakhon Pathom.

2.3.2 Satellite-based measurement

There are two types of satellites that can be used to measure or estimate UV radiation, which are polar orbiting satellites and geostationary satellites. The details of these satellites are as follows.

1) Polar orbiting satellite

Polar orbiting satellite is kind of polar orbits. It orbits the earth from the north to the south and the satellite is at low altitudes between 600–800 km (Figure 9). Generally, this type of satellite has velocity at about 7.8 km/s. From its orbit and velocity around the earth, it can provide data at a location on the earth's surface about 1-2 datasets per day.

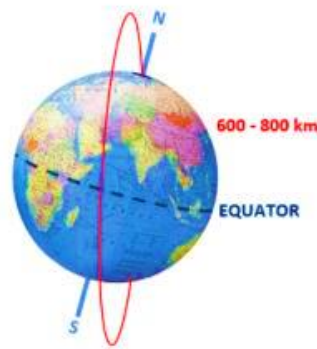


Figure 9 The polar orbiting satellite (adapted from Panwar, 2021).

There are some UV data available from this satellite. The useful and well known satellite UV data covering the global region such as TROPOMI/Sentinel-5, OMI/AURA, and TOMS/Earth Probe (Lindfors et al., 2018; Meerkötter et al., 2006; Tanskanen et al., 2006). In case of OMI/AURA, it provides surface UVB irradiance and erythemal dose rate with a resolution of 1.0 degree \times 1.0 degree as shown in Figure 10.

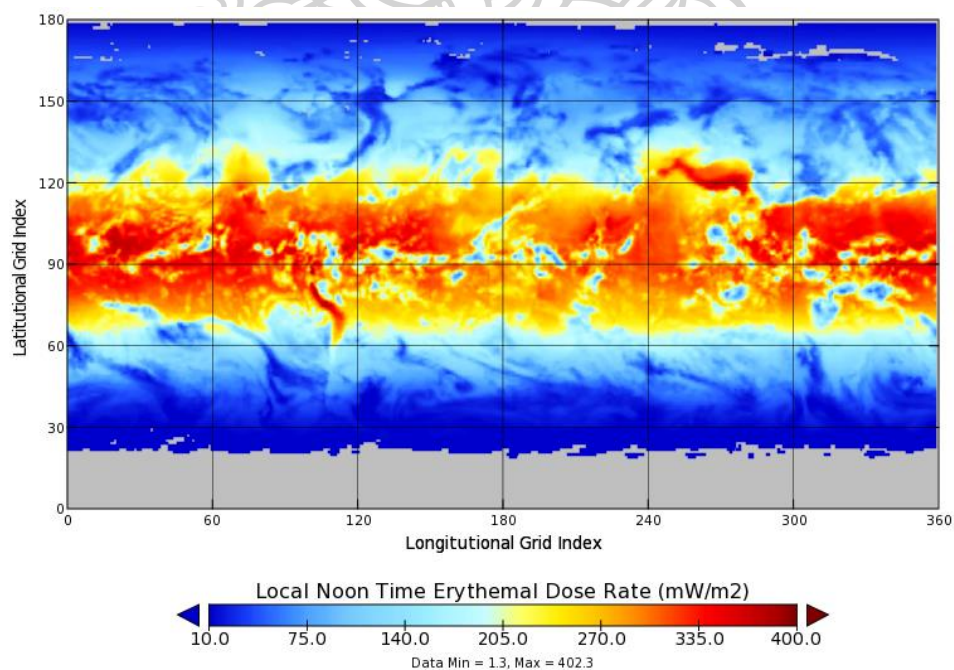


Figure 10 An example of erythemal dose rate from AURA satellite (adapted from Earthdata, 2006).

2) Geostationary satellite

The orbit of this satellite is about 35,786 km (Figure 11) above the equator, and velocity of the satellite is equal to the velocity of the earth's rotation. Images from this satellite can vision half of the world. This satellite is usually used in meteorology and communication.

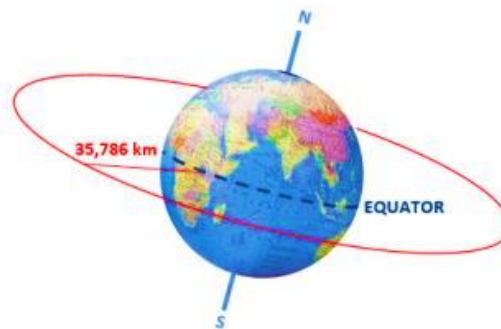


Figure 11 The geostationary satellite (adapted from Panwar, 2021).

There are several geostationary satellites providing atmospheric data, which are located over some regions of the earth as shown in Figure 12.

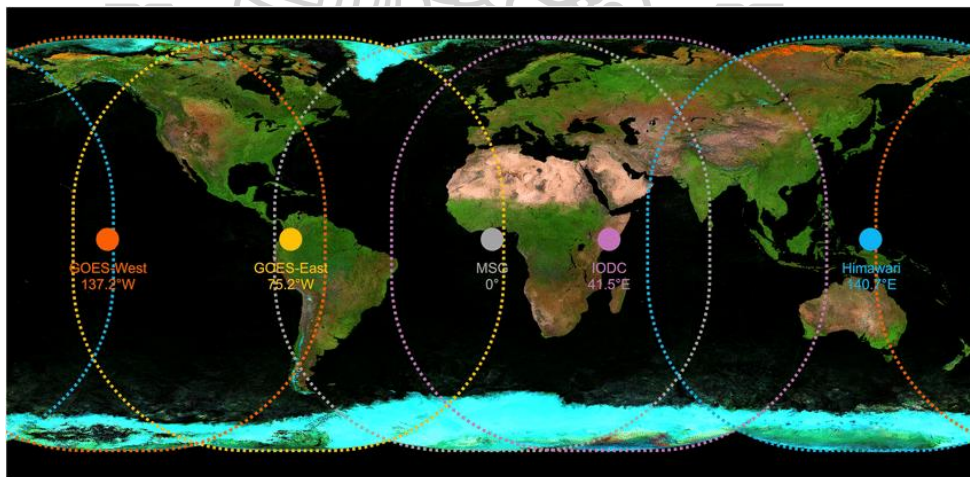


Figure 12 Coverage areas for geostationary satellites (adapted from Ceamanos et al., 2021).

An example of UV data obtained from this type of satellite is cloud free UV dose for vitamin D production in the skin from Meteosat satellite as shown in Figure 13.

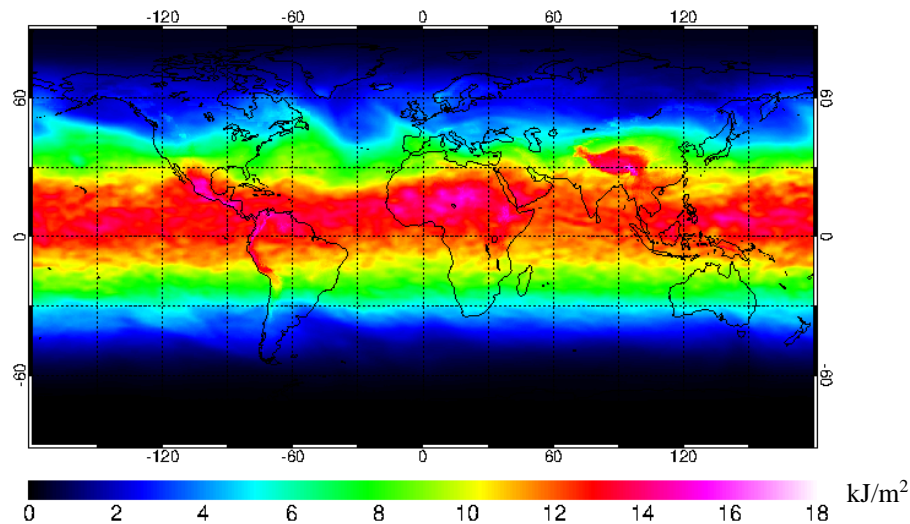


Figure 13 An example cloud free vitamin D UV dose from Meteosat satellite (adapted from TEMIS, 2023).

2.4 Effects of solar ultraviolet radiation on human health

Solar ultraviolet radiation affects human health both harmful and beneficial. Harmful effects are erythema, skin cancer, and cataract. Beneficial effects are production of previtamin D₃, and therapy of psoriasis. These harmful and beneficial effects are related to the exposure time, the dose of solar ultraviolet radiation, and the physical characteristics of the body human. Examples of a harmful effect and two beneficial effects are described as follows.

- Erythema

When skin body overexposure solar ultraviolet radiation, UVA can stimulate skin body to create melanin to protect skin (Maddodi et al., 2012) that can cause tanning and wrinkles, whereas UVB is more efficient to erythema (Brenner & Hearing, 2008). UVB is lower penetrated through skin layers than UVA due to UVB is more absorbed by cellular biochromes at the epidermis. Therefore, UVB affects mainly on constrain to the epidermis and UVA affects cellular and extracellular structures in the dermis (Solano, 2020).



Figure 14 The ultraviolet radiation can cause erythema (adapted from Barber, 2011).

Shorter wavelength (i.e. UVB) can cause erythema of human skin as it has higher response than longer wavelength (i.e. UVA). Response of human skin for erythema can compute as Eq. (2.11) and is shown in Figure 15.

$$R_{\text{Ery}} = \begin{cases} 1.0 & ; 250 < \lambda \leq 298 \text{ nm} \\ 10^{[0.094(298-\lambda)]} & ; 298 < \lambda \leq 328 \text{ nm} \\ 10^{[0.015(140-\lambda)]} & ; 328 < \lambda \leq 400 \text{ nm} \end{cases} \quad (2.11)$$

where R_{Ery} = the erythemal response (-)

λ = the wavelength (nm).

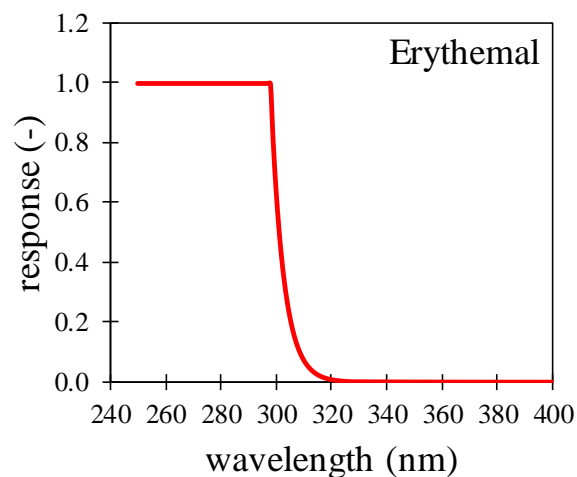


Figure 15 Action spectrum for erythema in human skin (adapted from McKinlay & Diffey, 1987).

- Production of vitamin D

When sufficient UV radiation penetrates into human skin layer, 7-dehydrocholesterol in the epidermis layer is converted to vitamin D and it is converted to a calcidiol (25(OH)D) in liver, which is then converted to a calcitriol hormone (1,25(OH)₂D) in the kidneys (Figure 16). Vitamin D is essential for absorption of calcium and phosphorus for healthy bones (Mostafa & Hegazy, 2015).

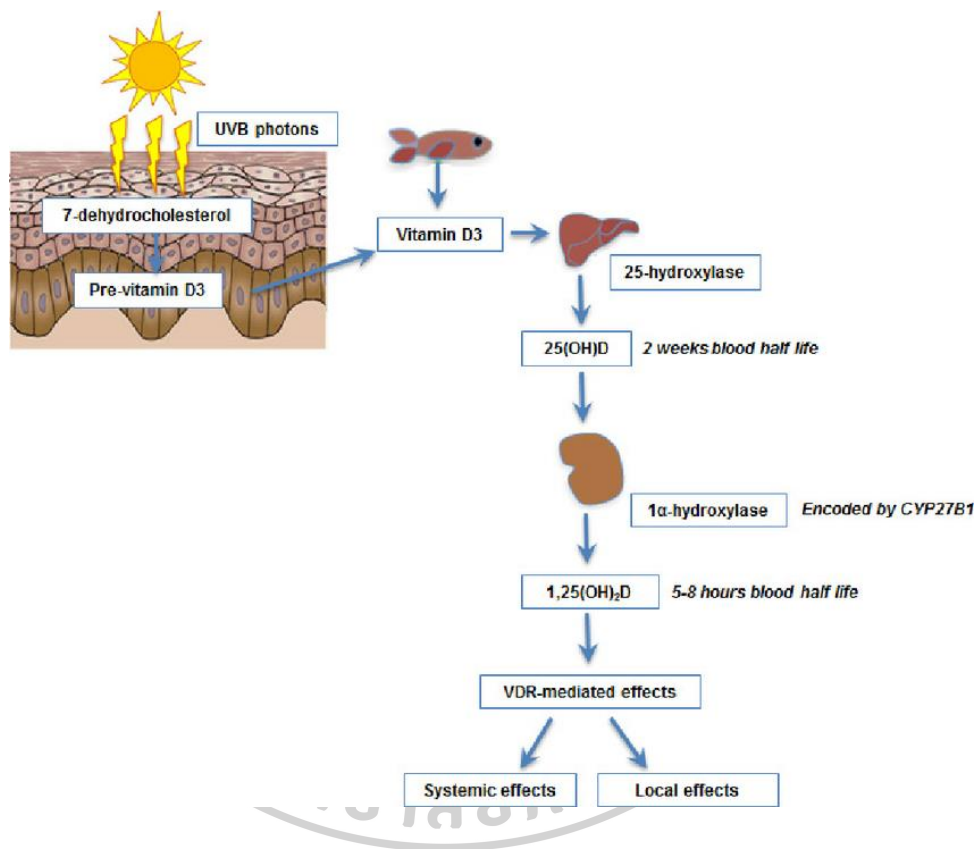


Figure 16 The vitamin D synthesis from sun exposure (adapted from Lucas et al., 2014).

Human skin can respond to each wavelength differently. UVB can help vitamin D production of skin. Figure 17 shows an action spectrum for the production of previtamin D₃ in human skin ($R_{\text{vit D}}$).

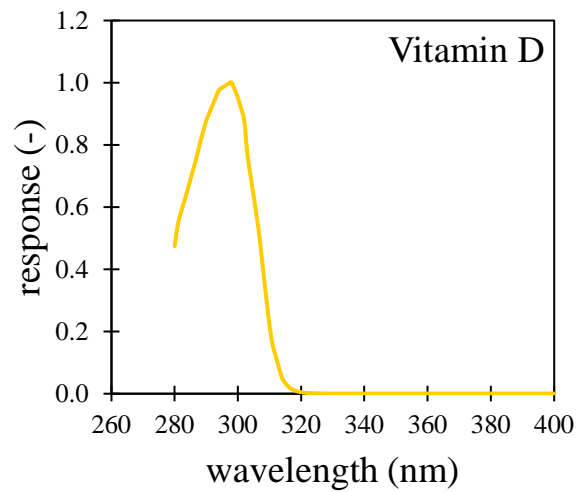


Figure 17 Action spectrum for the production of previtamin D₃ in human skin (adapted from Terenetskaya et al., 2006).

- Psoriasis

UV, especially UVB, works best for psoriasis treatment. An example of psoriasis on human body is shown in Figure 18. The spectral response for phototherapy of psoriasis can calculate following Eq. (2.12) and is shown in Figure 19. The maximum of its response is at 300 nm approximately.



Figure 18 The phototherapy of psoriasis.

$$R_{\text{Pso}} = \begin{cases} 0.6504 \times 10^{-0.6304(296-\lambda)} & \lambda < 296 \text{ nm} \\ 1.0000 \times 10^{-0.0467(300-\lambda)} & 296 \leq \lambda < 300 \text{ nm} \\ 1.0000 \times 10^{-0.1067(\lambda-300)} & 300 \leq \lambda < 304 \text{ nm} \\ 0.3743 \times 10^{-0.1571(\lambda-304)} & 304 \leq \lambda < 313 \text{ nm} \\ 0.0144 \times 10^{0.08233(313-\lambda)} & 313 \leq \lambda < 330 \text{ nm} \\ 0.0057 \times 10^{0.00937(330-\lambda)} & 330 \leq \lambda < 400 \text{ nm} \end{cases} \quad (2.12)$$

where R_{Pso} = the phototherapy of psoriasis response (-)

λ = the wavelength (nm).

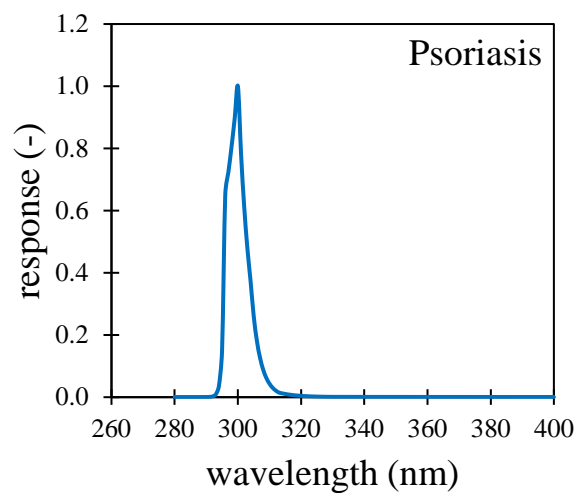


Figure 19 Action spectrum for phototherapy of psoriasis (adapted from Krzyściński et al., 2012).

2.5 Literature reviews on the UV from the measurement and UV mapping from satellite data

There are many research works that focus on surface UV radiation. Examples of the works are described as follows.

Eck et al. (1995) presented a method for estimated spectral UVB irradiance in Canada from satellite data i.e. reflectivity (R). In their research, the solar flux at the ground for clear sky condition can be written as:

$$F_{\text{ch}} = F_{\text{d}}(1 + r)/(1 - RS_{\text{b}}) \quad (2.13)$$

where F_{ch} = the solar flux at the ground for clear sky condition (W/m^2)
 F_d = the direct solar flux reaching the surface (W/m^2)
 r = the ratio of diffuse to direct radiation (-)
 R = the surface reflectivity (-)
 S_b = the fraction of reflected radiation backscattered to the surface by the atmosphere (-).

The solar flux at the ground for all sky condition in this work is as follows:

$$F_d = F_o \cos\theta \exp(-\sec\theta(\alpha\Omega + \beta p)) / d^2 \quad (2.14)$$

where F_d = the solar flux at the ground for all sky condition (W/m^2)
 F_o = the extraterrestrial solar flux at 1 AU (W/m^2)
 d = the sun-earth distance (AU)
 α = the ozone absorption coefficient per unit ozone amount (1/DU)
 β = the Rayleigh scattering coefficient per unit pressure (1/atm)
 p = the surface pressure (atm)
 θ = the solar zenith angle (degree)
 Ω = the total column ozone (DU).

Verdebut (2000) presented a method for estimating surface UV radiation maps over Europe using satellite data and ancillary geophysical data. Parameters of solar zenith angle, total column ozone amount, cloud liquid water thickness, near-surface horizontal visibility, surface elevation, and UV albedo were used to generate a look-up table to obtain the UV irradiance. In his work, cloud properties were processed from satellite data.

Li et al. (2000) developed a simple method for retrieving surface UV radiation dose rate from satellite data in Canada. Surface UV radiation determined by the transmittance of the ozone layer, which can be derived from total ozone measurements of TOMS and the reflectance of the atmospheric layer

Foyo-Moreno et al. (2007) presented adaptation of an empirical model for erythemal ultraviolet (UVER) irradiance in Spain from a relation between UVER in clear sky condition ($UVER_0$) and optical air mass (m_r) as Eq. (2.15) for clear sky conditions model.

$$UVER_0 = 12 + 1490e^{-\frac{m_r}{0.5}} + 124e^{-\frac{m_r}{0.8}} \quad (2.15)$$

For all sky conditions model, UVER can be calculated from the following equation:

$$UVER = 1.5(k_t UVER_0)^{0.96} \quad (2.16)$$

where UVER = erythemal ultraviolet irradiance (W/m^2)

k_t = global broadband hemispherical transmittance (-).

Gadhavi et al. (2008) developed an algorithm to estimate UV flux at the surface over north America using data of cloud amount, surface albedo, and aerosol from geostationary satellite, and also data of ozone from polar orbiting satellite. Researchers presented lookup tables for atmospheric transmission from data of solar zenith angle, aerosol, cloud optical depth, ozone, water vapour, and surface elevation using a radiative transfer model (SBDART). Afterward, UV flux were estimated from input data of satellite data.

Antón et al. (2009) presented an empirical model to estimate ultraviolet erythemal transmissivity in Spain. UVER transmissivity (T_{UV}) depends on ozone column (Z) and clearness index (k_t) as the following Equation:

$$T_{UV} = a \cdot Z^b \cdot k_t^c \quad (2.17)$$

where a, b and c are the coefficients of the model.

Janjai et al. (2010) developed technique for mapping erythemally-weighted solar ultraviolet (EUV) radiation from satellite data in Thailand that physical model is given by:

$$EUV_{SUR} = \frac{(1-\rho_{EUV}-(1-\tau_0)-\tau_0\alpha_{AER})EUV_{TOA}}{[(1-\rho_{G,EUV})+\rho_{G,EUV}\alpha_{AER}+\rho_{G,EUV}(1-\alpha_{AER})(1-\tau_0)]} \quad (2.18)$$

where EUV_{SUR} = the EUV at the surface (kJ/m^2)

EUV_{TOA} = the EUV at the top of the atmosphere (kJ/m^2)

τ_0 = the ozone transmission (-)

α_{AER} = the aerosol absorption coefficient (-)

ρ_{EUV} = the earth-atmospheric albedo in EUV wavelength band (-)

$\rho_{G,EUV}$ = the broadband surface albedo (-).

Mateos Villán et al. (2010) analyzed the influence of clouds on UV radiation. In their analysis, data were divided into three intervals separated by solar elevation; $h_1 \geq 60^\circ$, $40^\circ < h_2 < 60^\circ$ and $h_3 \leq 40^\circ$. The results showed that UV radiation decreases as cloud cover increases for the three intervals. For dependence of cloud modification (CMF) on cloudiness for all elevation, the result showed that CMF values decrease with cloudiness.

Zhang et al. (2013) investigated effects of aerosols on solar radiation. They presented that, in Beijing, higher aerosol values were found in summer, and lower aerosols were found in winter. Their results also showed that aerosol can attenuates UV radiation greater than global radiation. In addition, they proposed a semiempirical model for estimating daily ultraviolet radiation from global radiation in Beijing by using a relationship between cloud modification factor which is a ratio between the radiation under all sky conditions and the radiation under clear sky conditions in UV wavelength (CMF_{UV}), and global radiation (CMF_G). The relationship of cloud modification factors is shown in the following equation.

$$CMF_{UV} = 0.12e^{1.72CMF_G} \quad (2.19)$$

Miyauchi and Nakajima (2016) studied a relationship between solar erythemal ultraviolet radiation (UV_{Ery}) and solar ultraviolet radiation for vitamin D synthesis (UV_{VitD}) in Japan. From their results, UV_{VitD} can be estimated from UV_{Ery} as denoted in the following equations.

$$UV_{VitD} = 2.11UV_{Ery} - 0.027 \quad (UV_{Ery} \geq 0.04 \text{ W/m}^2) \quad (2.20)$$

$$UV_{VitD} = 16.74(UV_{Ery})^2 + 0.81UV_{Ery} \quad (UV_{Ery} < 0.04 \text{ W/m}^2)$$

Choosri et al. (2017) proposed maps of monthly average hourly diffuse erythemal ultraviolet radiation (EUV_D) in Thailand from an empirical model by using ground-based and satellite-based data. An empirical model is a function of air mass (m_a), aerosol optical depth (AOD), and cloud index (n) shown as the following equation.

$$EUV_D = C_0 m_a^{C_1} + C_2 AOD + C_3 n \quad (2.21)$$

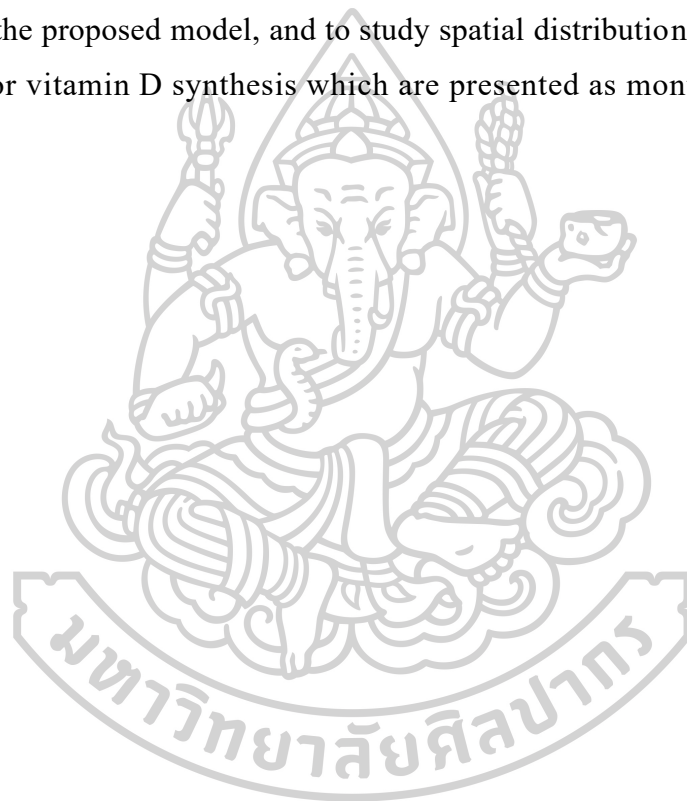
where C_0 , C_1 , C_2 and C_3 are coefficients ($C_0=173.2241$, $C_1=-1.5762$, $C_2=-31.0808$ and $C_3=-41.2056$).

For Liu et al. (2017), UV radiation under various sky conditions was developed based on UV radiation measurements during 2005–2014 from the Chinese Ecosystem Research Network (CERN). The empirical UV estimation model depends on the clearness index and the solar elevation angle under various sky conditions at each typical station. This model provides accurate UV radiation data, with an average root mean square error of 14.31%.

Brogniez et al. (2021) studied erythemal and vitamin D effective dose rates at two mainland sites that are Villeneuve d'Ascq (VDA) and Observatoire de Haute-Provence (OHP) and one island site that is R'eunion Island site (SDR). The results at the mainland sites (VDO and OHP) show that solar exposure close to solar noon induces erythema in phototypes 1 to 3 during most of the year and in the tropics (SDR), phototypes 4 and 5 are also at risk of erythema. At all sites, solar exposure

close to solar noon permits synthesis of desired amount of vitamin D by all phototypes during most of the year.

Thailand is located in the tropics which receives high level of solar radiation, but there have been relatively few studies about solar ultraviolet radiation for vitamin D synthesis and instrument used to measure solar ultraviolet radiation for vitamin D synthesis is more expensive causing the data from ground-based measurement is not covering all areas. Therefore, the objectives of this research are to develop an empirical model for estimating solar ultraviolet radiation for vitamin D photosynthesis, to validate the proposed model, and to study spatial distributions of solar ultraviolet radiation for vitamin D synthesis which are presented as monthly average hourly maps.



Chapter 3

Methodology, Result and Discussion

To achieve the objectives of the thesis, several tasks need to be carried out. These are measurement, modeling, validation, and mapping. The details of each task are described as follows.

3.1 Measurement

The solar ultraviolet radiation for vitamin D synthesis (DUV) is beneficial UV radiation. Its variation depends on compositions of the earth's atmosphere. To produce the DUV maps, the measurements of DUV and several compositions of the earth's atmosphere were studied. Therefore, several measurement data were collected and process. The details are as follows.

1) Solar ultraviolet radiation for vitamin D synthesis

In this thesis, solar ultraviolet radiation for vitamin D synthesis can be estimated using a relationship between solar erythemal ultraviolet radiation and solar ultraviolet radiation for vitamin D synthesis. The details of ground-based measurements of solar erythemal ultraviolet radiation and solar ultraviolet for vitamin D synthesis, and the relationship are described as follows.

- Solar ultraviolet radiation spectrum

The solar ultraviolet radiation spectrum was measured by a spectroradiometer model DMc150 of Bentham Instruments company. The sensor of this instrument was installed at roof top of a Science building at Silpakorn University in Nakhon Pathom (13.82°N, 100.04°E) that there have not obstacles of the celestial sphere. The solar radiation incidents the sensor, and the signals pass the optic fiber that connects between the sensor (Figure 20(a)), and the control box located in a control room (Figure 20(b)). The monochromator in the control box will separate the radiation into each wavelength and the computer with BenWin+ program is set to record the signal of spectral UV radiation ranging between 260 and 420 nm at intervals of 1 nm every

10 minute. An example of BenWin+ display on the computer is presented in Figure 21 which shows spectral UV radiation measuring from the spectroradiometer.

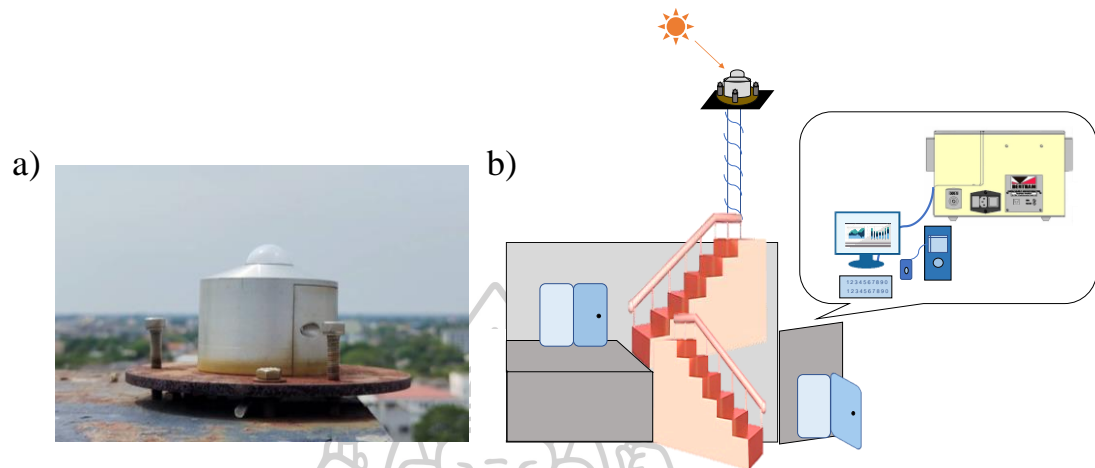


Figure 20 The spectroradiometer model DMc150 of Bentham Instruments company at the roof top of Science building at Silpakorn University in Nakhon Pathom (a) sensor and (b) control box.

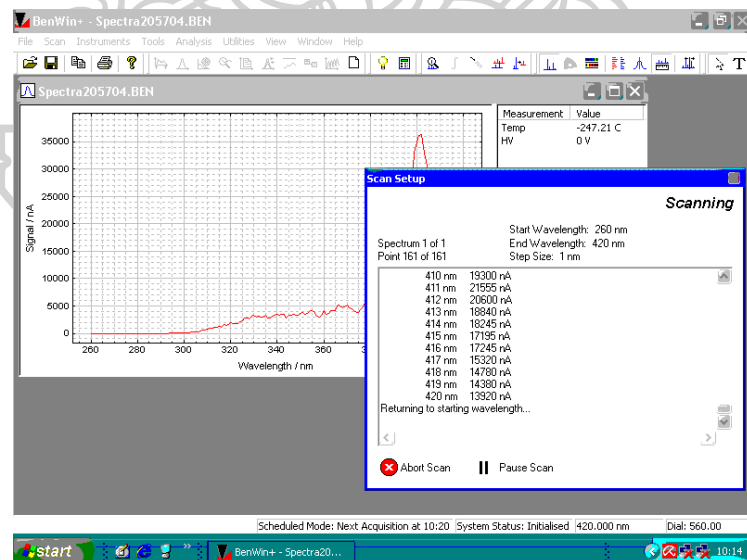


Figure 21 The computer display of BenWin+.

The spectral UV irradiance can be processed by the following equation:

$$I_{\lambda} = \frac{V_{\lambda}}{S_{\lambda}} \quad (3.1)$$

where I_λ = the spectral UV irradiance (mW/m²-nm)
 V_λ = the electrical signal at each wavelength (nA)
 S_λ = the sensitivity at each wavelength of instrument (nA/mW/m²-nm).

The solar ultraviolet radiation for vitamin D production was calculated from the spectral UV irradiance multiply with the spectral response of vitamin D production mentioned in Chapter 2 as Eq. (3.2).

$$DUV = \int I_\lambda \cdot R_{Vit D} d\lambda \quad (3.2)$$

where DUV = the solar ultraviolet radiation for vitamin D production (mW/m²)
 I_λ = the spectral UV irradiance (mW/m²-nm)
 $R_{Vit D}$ = the spectral response of vitamin D production (-).

In this work, the solar ultraviolet radiation for vitamin D production were processed and averaged to obtain monthly average hourly DUV from 8 a.m. to 4 p.m. from 1 January, 2014 to 31 December, 2018.

- Solar erythemal ultraviolet radiation

The solar erythemal ultraviolet radiation (EUV) was measured by UV biometer model 501A of Solar Light company. The biometer was installed at four stations in main regions of Thailand (Figure 22). These stations are at Silpakorn University in Nakhon Pathom (13.82°N, 100.04°E) and three meteorological stations in Chiang Mai (18.78°N, 98.98°E), Ubon Ratchathani (15.25°N, 104.87°E) and Songkhla (7.20°N, 100.60°E) (Figure 23-26). The electrical signals from each biometer consist of signals for UV light and signals for instrument's temperature. These signals at each station were recorded by a datalogger model DX2000 of YOKOGAWA every 1 second (Figure 27). EUV can be calculated from the signals using an equation represented by Webb et al. (2006).

$$E_{CIE} = (U - U_{offset}) \cdot C \cdot f_n(\theta_z, O_3) \cdot \varepsilon(T) \cdot Coscor \quad (3.3)$$

where E_{CIE}	= the CIE erythemal UV irradiance (W/m^2)
U	= the measured electrical signal from the radiometer (V)
U_{offset}	= the electrical offset for dark conditions (V)
$f_n(\theta_z, O_3)$	= the spectral conversion function depending on solar zenith angle (θ_z) and total column ozone (O_3) (-)
C	= the calibration coefficient, a constant value determined for a specific condition (For example, $\theta_z = 40^\circ$ and $O_3 = 300$ DU) ($W/m^2/V$)
$\varepsilon(T)$	= the temperature correction function (-)
$Coscor$	= the cosine correction function (-).

To find C , each biometer was calibrated with the standard EUV value from the Bentham spectroradiometer at Nakhon Pathom under the same conditions. This standard EUV value can be calculated from Eq. (3.4).

$$EUV = \int I_\lambda \cdot R_{Ery} d\lambda \quad (3.4)$$

where EUV	= the solar erythemal ultraviolet radiation from Bentham spectroradiometer (W/m^2)
I_λ	= the spectral UV irradiance ($mW/m^2\text{-nm}$)
R_{Ery}	= the spectral response of erythema (-).

Therefore, C of each biometer can be calculated from Eq. (3.5).

$$C = \frac{EUV}{(U - U_{offset}) \cdot f_n(\theta_z, O_3) \cdot \varepsilon(T) \cdot Coscor} \quad (3.5)$$

where C	= the calibration coefficient, a constant value determined for specific conditions ($W/m^2/V$)
EUV	= the solar erythemal ultraviolet radiation from Bentham spectroradiometer (W/m^2)
U	= the measured electrical signal from the radiometer (V)

- U_{offset} = the electrical offset for dark conditions (V)
 $f_n(\theta_z, O_3)$ = the spectral conversion function depending on solar zenith angle (θ_z) and total column ozone (O_3) (-)
 $\varepsilon(T)$ = the temperature correction function (-)
 Coscor = the cosine correction function (-).

To find $f_n(\theta_z, O_3)$ which is a function correcting for spectral response of detector to erythema spectral response, it is calculated as

$$f_n(\theta_z, O_3) = \frac{f(\theta_z, O_3)}{f_c(\theta_z, O_3)} \quad (3.6)$$

- where $f_n(\theta_z, O_3)$ = the spectral conversion function depending on solar zenith angle (θ_z) and total column ozone (O_3) (-)
 $f(\theta_z, O_3)$ = the spectral response function at different θ_z and O_3 (-)
 $f_c(\theta_z, O_3)$ = the spectral response function at a specific condition (For example, $\theta_z = 40^\circ$ and $O_3 = 300$ DU) (-).

$$f(\theta_z, O_3) = \frac{\int \text{CIE}(\lambda) E_{\text{rad}}(\lambda, \theta_z, O_3) d\lambda}{\int \text{SRF}(\lambda) E_{\text{rad}}(\lambda, \theta_z, O_3) d\lambda} \quad (3.7)$$

- where $f(\theta_z, O_3)$ = the spectral response function at different θ_z and O_3 (-)
 $E_{\text{rad}}(\lambda, \theta_z, O_3)$ = the global solar spectral irradiance calculated from a radiative transfer model (-)
 CIE = the CIE spectral response of erythema (-)
 SRF = the spectral response of sensor (-)
 λ = the wavelength (-).

To find Coscor , it can use Eq. (3.8) for calculating.

$$\text{Coscor} = \frac{1}{f_{\text{glo}}} \quad (3.8)$$

where Coscor = the cosine correction function (-)

f_{glo} = the global cosine error (-).

$$f_{\text{glo}} = f_{\text{dir}} \frac{E_{\text{dir}}}{E_{\text{glo}}} + f_{\text{dif}} \frac{E_{\text{dif}}}{E_{\text{glo}}} \quad (3.9)$$

where f_{glo} = the global cosine error (-)

f_{dir} = the direct cosine error equal to the angular response function from the manufacturer (-)

f_{dif} = the diffuse cosine error (-)

E_{dir} = the direct radiation calculated from a radiative transfer model (W/m^2)

E_{dif} = the diffuse radiation calculated from a radiative transfer model (W/m^2)

E_{glo} = the global radiation calculated from a radiative transfer model (W/m^2).

$$f_{\text{dir}} = \frac{\text{ARF}(\theta)}{\cos(\theta)} \quad (3.10)$$

where f_{dir} = the diffuse cosine error (-)

ARF = the angular response function from the manufacturer (-)

θ = the angular incident of radiation (-).

$$f_{\text{dif}} = 2 \int_0^{\frac{\pi}{2}} \text{ARF}(\theta) \sin(\theta) d\theta \quad (3.11)$$

where f_{dif} = the diffuse cosine error (-)

ARF = the angular response function from the manufacturer (-)

θ = the angular incident of radiation (degree).

To find $\varepsilon(T)$, it can be calculated from instrument's temperature. Due to the calibration process is under a constant temperature of 25°C and thus obtains the output

voltage at this temperature of +1V and the sensitivity of 20 mV/°C, the detector temperature in the actual environment can be calculated as follows.

$$T_{\text{det}} = (50 \times U_{\text{temp}}) - 25 \quad (3.12)$$

where T_{det} = the actual detector temperature (°C)

U_{temp} = the temperature output from the biometer (V).

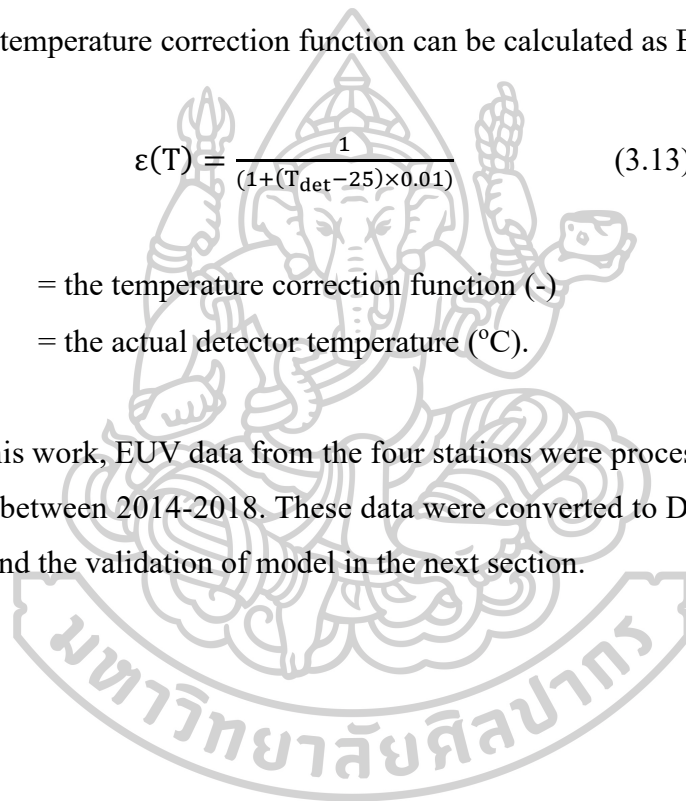
The temperature correction function can be calculated as Eq. (3.13).

$$\varepsilon(T) = \frac{1}{(1 + (T_{\text{det}} - 25) \times 0.01)} \quad (3.13)$$

where $\varepsilon(T)$ = the temperature correction function (-)

T_{det} = the actual detector temperature (°C).

In this work, EUV data from the four stations were processed to obtain hourly EUV value between 2014-2018. These data were converted to DUV and used for the modelling and the validation of model in the next section.



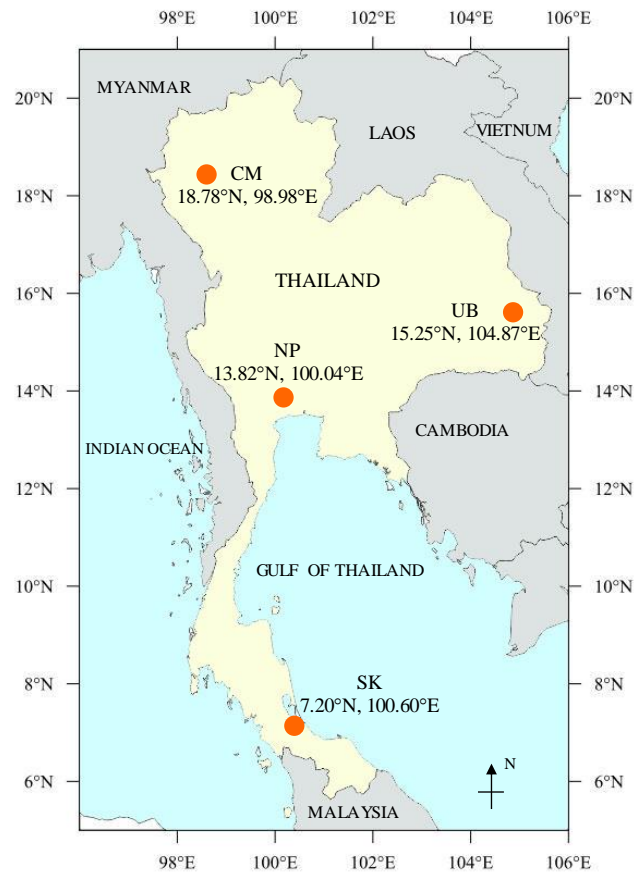


Figure 22 The location of four stations



Figure 23 Broadband UV radiometer model 501A of Solar Light company at Chiang Mai station.



Figure 24 Broadband UV radiometer model 501A of Solar Light company at Nakhon Pathom station.



Figure 25 Broadband UV radiometer model 501A of Solar Light company at Ubon Ratchathani station.



Figure 26 Broadband UV radiometer model 501A of Solar Light company at Songkhla station.

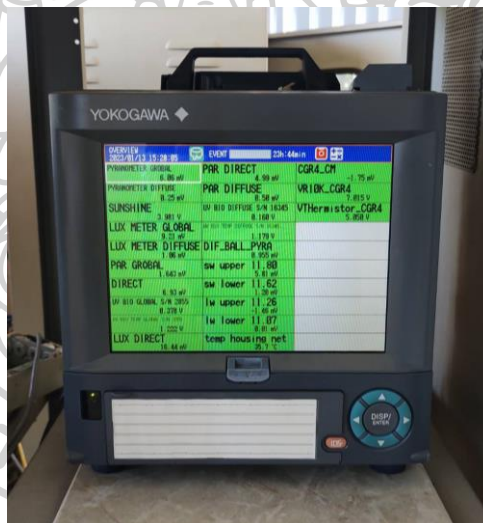


Figure 27 The datalogger model DX2000 of YOKOGAWA company.

- Estimation of DUV from EUV

In order to obtain DUV, spectral UV data was required. However, there is only one spectroradiometer installed at Nakhon Pathom. Therefore, in this thesis, a relationship between hourly DUV from the Bentham spectroradiometer and hourly EUV from the biometer at Nakhon Pathom was generated using the data in 2014 and 2016 for the modelling and 2017 to 2018 for the validation.

In this thesis, the relation in terms of a ratio between DUV and EUV depends on cosine of solar zenith angle in a polynomial form showing as

$$\frac{\text{DUV}}{\text{EUV}} = -1.864(\cos\theta_z)^2 + 3.3635\cos\theta_z + 0.3644 \quad (3.14)$$

where DUV = the solar ultraviolet radiation for vitamin D synthesis (mW/m^2)

EUV = the solar erythemal ultraviolet radiation (mW/m^2)

θ_z = the solar zenith angle (degree).

Before using this relation, it was validated. This relation was used to calculate DUV from EUV. The DUV calculated from the relation was compared with those measured by the Bentham spectroradiometer. The validation results show that the DUV from the ground-based measurement agree well with the DUV calculated from the polynomial equation. The difference of these data in terms of the root mean square difference (RMSD) as Eq. (3.15) and the mean bias difference (MBD) as Eq. (3.16) were found to be 9.8% and 3.2%, respectively (Figure 28).

$$\% \text{RMSD} = \sqrt{\frac{\sum_{i=1}^N (\text{DUV}_{\text{model},i} - \text{DUV}_{\text{meas},i})^2}{\frac{\sum_{i=1}^N \text{DUV}_{\text{meas},i}}{N}}} \times 100 \quad (3.15)$$

$$\% \text{MBD} = \frac{\sum_{i=1}^N (\text{DUV}_{\text{model},i} - \text{DUV}_{\text{meas},i})}{\frac{\sum_{i=1}^N \text{DUV}_{\text{meas},i}}{N}} \times 100 \quad (3.16)$$

where $\text{DUV}_{\text{model},i}$ = the solar ultraviolet radiation for vitamin D synthesis from the model (mW/m^2)

$\text{DUV}_{\text{meas},i}$ = the solar ultraviolet radiation for vitamin D synthesis from the measurement (mW/m^2)

N = numbers of data (-).

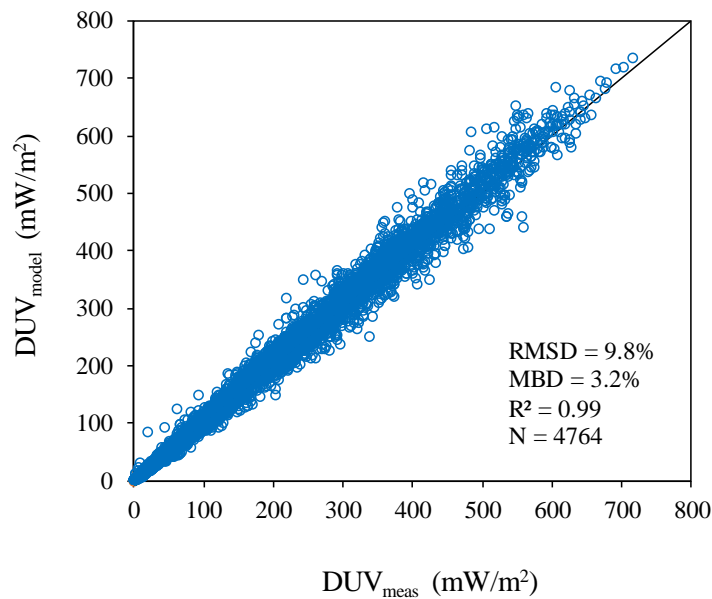


Figure 28 The comparison between the solar ultraviolet radiation for vitamin D synthesis from the model (DUV_{model}) and that from the measurement (DUV_{meas}).

In addition, the relationships between DUV and EUV were performed using a radiative transfer model (Libradtran) for the four UV monitoring sites. The results are shown in Figure 29. It can be noticed that the relationship between DUV and EUV are similar for all sites. Therefore, the relation in Eq. (3.14) was performed to calculate hourly DUV using hourly EUV from biometers at the four stations namely Nakhon Pathom station, Chiang Mai station, Ubon Ratchathani station, and Songkhla station. Afterward, the hourly DUV data were averaged to obtain monthly average hourly DUV during 2014-2018 from 8 a.m. to 4 p.m.

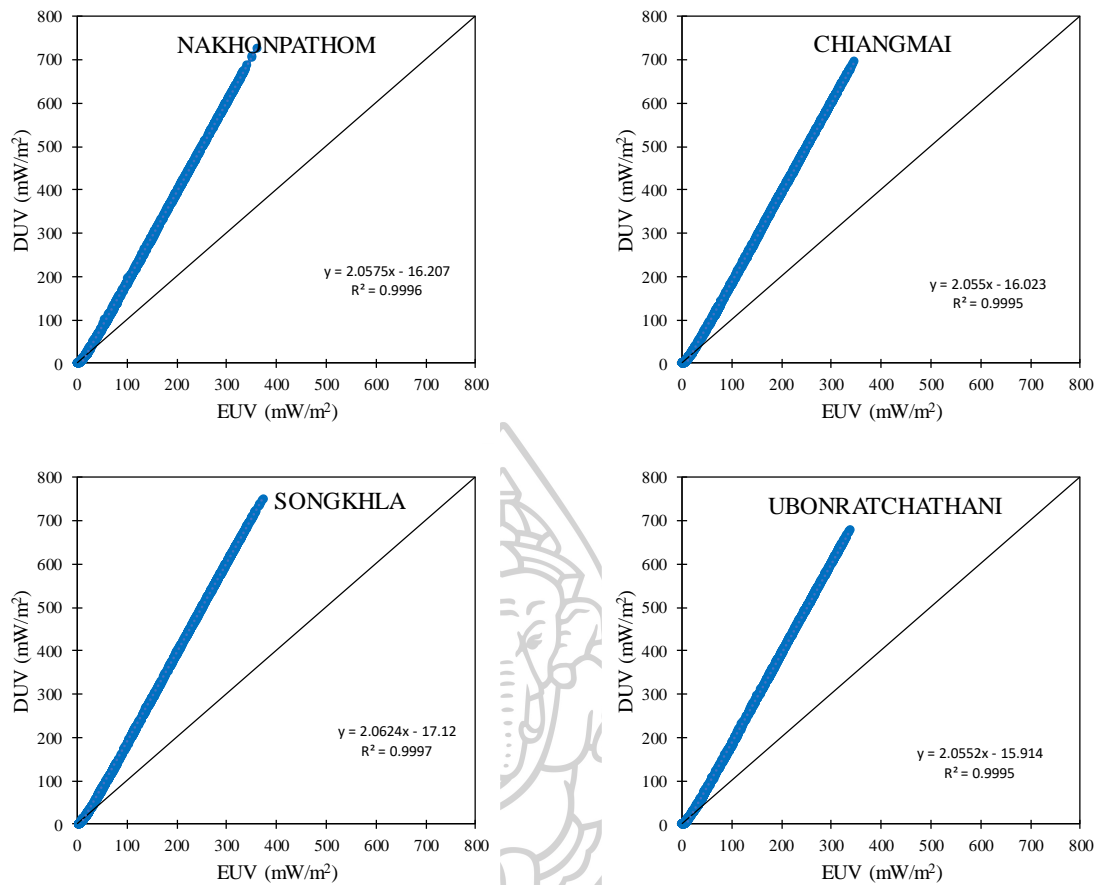


Figure 29 The relationship between DUV and EUV using the radiative transfer model.

2) Aerosol optical depth at 340 nm

Due to Thailand has few stations to provide aerosol optical depth (AOD), aerosol optical depth data used in this work can be calculated from Eq. (3.17) which represented by Iqbal (1983).

$$\text{AOD} = \beta \lambda^{-\alpha} \quad (3.17)$$

where AOD = the aerosol optical depth (-)

λ = the wavelength (μm)

α = Angstrom's wavelength exponent (-)

β = Angstrom's turbidity coefficient (-).

α and β are dependent of wavelength. In this work, the wavelength is $0.34 \mu\text{m}$ which is in the UV range, and the Angstrom's wavelength exponent was set to be 1.3

which is an average for natural atmosphere in this region (Iqbal, 1983). For Angstrom's turbidity coefficient, it can be calculated from the relationship with visibility as shown in Eq. (3.18) reported by (Janjai et al., 2003).

$$\beta = 0.589 - 0.068\text{VIS} + 0.019\text{VIS}^2 ; \text{VIS} < 14 \text{ km} \quad (3.18)$$

where VIS = the visibility (km).

Visibility data representing ability to vision object was observed by the meteorologist every 3 hour. They observe the greatest distance toward the horizon at prominent objects. This can be specified with visually eye. In this work, visibility data were obtained from the meteorological 125 stations in Thailand (Figure 30).

In this work, visibility in 3-hour basis higher than 14 km were removed following the condition of Eq. (3.18). These data were replaced by interpolated data from the nearby data. Then, these 3-hour data were interpolated to obtain hourly data, and these data were converted to be aerosol optical depth at 340 nm. Afterward, the aerosol optical depth data was averaged to obtain monthly average hourly data from 8 a.m. to 4 p.m. in 2012-2021. The aerosol optical depth at 340 nm from Chiang Mai, Ubon Ratchathani and Songkhla meteorological stations and a meteorological station nearby Nakhon Pathom station were gathered during 2014-2018 for modelling and validation processes.

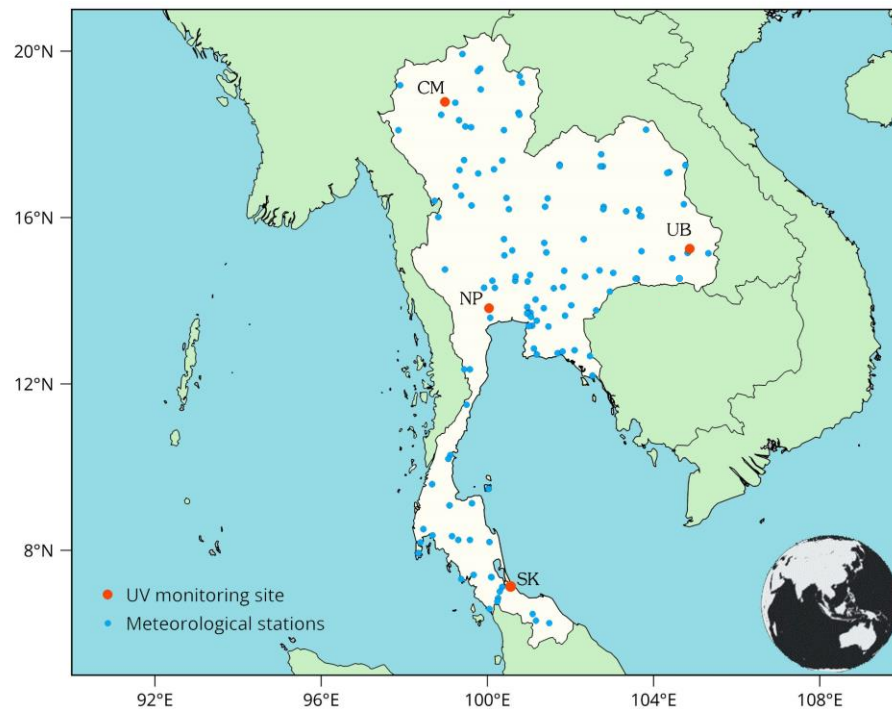


Figure 30 Locations of 125 meteorological stations and the four UV monitoring stations.

3) Cloud index

In this thesis, cloud index from the satellite data was used to indicate effects of cloud on solar ultraviolet radiation. Cloud images from two satellites that are MTSAT-2 (Himawari-7) satellite and Himawari-8 satellite of the Japan Meteorological Agency (JMA), Japan. They were processed to obtain cloud index for 10-year period covering 2012-2021.

The MTSAT-2 (Multi-Function Transport Satellite) (Figure 31) is a geostationary satellite that operates during 2010 to 2015. The position of its orbit is 35,800 km above the equator at around 140 degree east longitude. MTSAT-2 takes image every 30 minute. It has five channels consisting of Visible (0.55-0.90 micron), Infrared 1 (10.3-11.3 micron), Infrared 2 (11.5-12.5 micron), Infrared 3 (6.5-7.0 micron), and Infrared 4 (3.5-4.0 micron). In this work, cloud images in the visible channel were used.

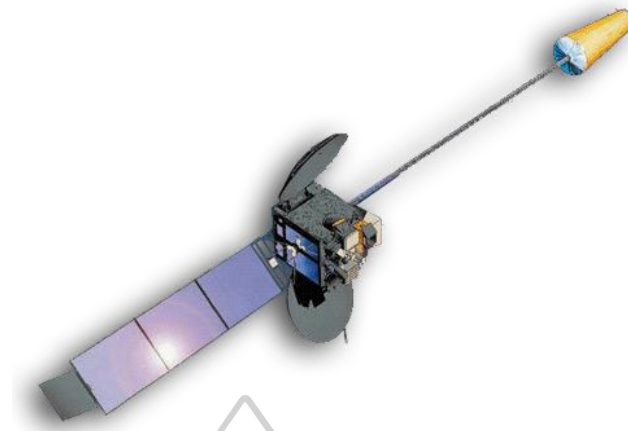


Figure 31 The MTSAT-2 (Multi-Function Transport Satellite).

Himawari-8 (Figure 32) is a geostationary satellite that was operated after MTSAT from 2015-2022. The position of its orbit is 35,800 km above the equator at around 140.7 degree east longitude. It has 16 observation bands including 3 bands of visible, 3 bands of near infrared and 10 bands of infrared as shown in Table 1.

Table 1 Advanced Himawari-8 imager.

Band	Wavelength (μm)	Spatial Resolution
1	0.43-0.48	1 km
2	0.50-0.52	1 km
3	0.63-0.66	0.5 km
4	0.85-0.87	1 km
5	1.60-1.62	2 km
6	2.25-2.27	2 km
7	3.74-3.96	2 km
8	6.06-6.43	2 km
9	6.89-7.01	2 km
10	7.26-7.43	2 km
11	8.44-8.76	2 km
12	9.54-9.72	2 km
13	10.3-10.6	2 km
14	11.1-11.3	2 km
15	12.2-12.5	2 km
16	13.2-13.4	2 km

The spatial resolution of visible band is 0.5-1 km and the resolutions of near infrared and infrared bands are 1-2 km. This satellite takes the image every 10 minute. In this work, visible channel at 0.51 micron were used.



Figure 32 The Himawari-8 satellite.

The boundary of the two satellites data used in this work is from 0.29-28.71°N and 90.20-109.80°E covering Thailand region. This provides 1,112×1,612 pixel. The processing of the satellite data is described in details in Section 3.4.

Due to satellite image has gray level values that vary as reflectivity, so gray level data of satellite image were converted to incur the pseudo reflectivity (ρ_{SAT}) by using a calibration table of JMA for MTSAT-2 (Figure 33) and Himawari-8 (Figure 34). The image data is 8 bit digital data which between 0-255 for MTSAT-2 and 10 bit digital which between 0-1023 for Himawari-8 where 0 means the lowest reflectivity and 255 or 1023 means the highest reflectivity from the earth's surface and the atmosphere.

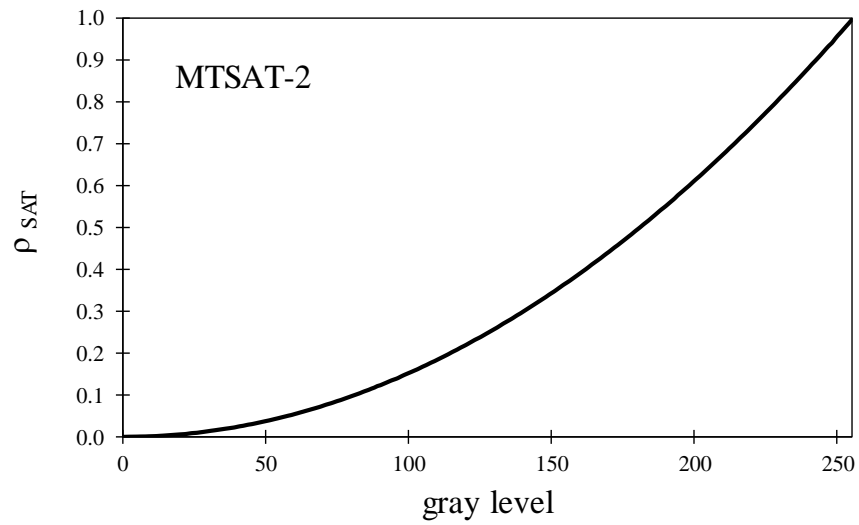


Figure 33 The calibration table of MTSAT-2 satellite showing a relation between the pseudo reflectivity (ρ_{SAT}) and gray level.

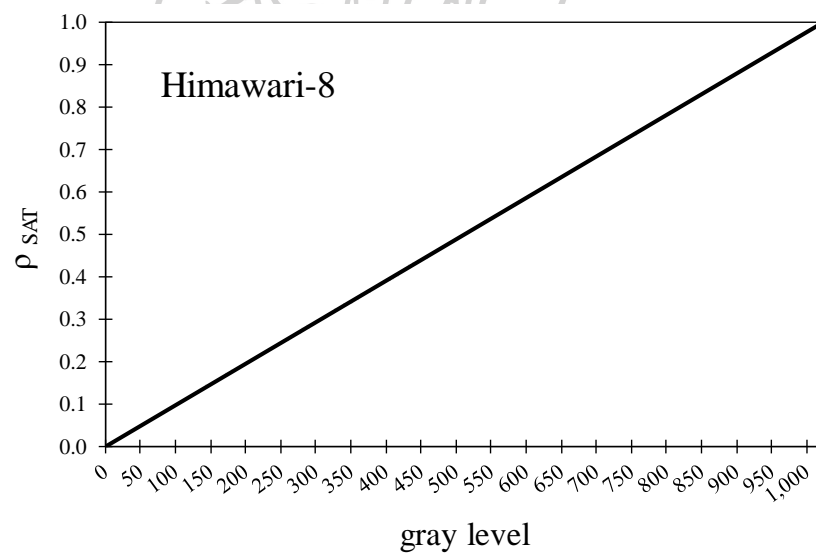


Figure 34 The calibration table of Himawari-8 satellite showing a relation between the pseudo reflectivity (ρ_{SAT}) and gray level.

Due to the pseudo reflectivity is value of the earth-atmospheric reflectivity in case that solar radiation incident in normal direction and cannot be used in reality as the solar radiation incident the earth's surface with different incident angles. Therefore,

the pseudo reflectivity needs to be corrected with the cosine of solar zenith angle to obtain the earth-atmospheric reflectivity (ρ_{EA}) as denoted in Eq. (3.19).

$$\rho_{EA} = \frac{\rho_{SAT}}{\cos\theta_Z} \quad (3.19)$$

where ρ_{EA} = the earth-atmospheric reflectivity (-)
 ρ_{SAT} = the pseudo reflectivity (-)
 θ_Z = the solar zenith angle (degree).

Afterward, the ρ_{EA} from MTSAT and Himawari-8 were converted to cloud index that can be calculated from Eq. (3.20) (Cano et al., 1986).

$$n = \frac{(\rho_{EA} - \rho_{min})}{(\rho_{max} - \rho_{min})} \quad (3.20)$$

where n = the cloud index (-)
 ρ_{EA} = the earth-atmospheric reflectivity (-)
 ρ_{min} = the surface reflectivity (-)
 ρ_{max} = the cloud reflectivity (-).

For ρ_{min} of each pixel, it can be considered from the minimum value of ρ_{EA} of each hour for each month. The ρ_{max} is the maximum value of ρ_{EA} for all pixels of all data.

Cloud index has the value from 0 to 1 which indicates reflection of radiation by cloud from no reflection to the highest reflection (Figure 35).

In this work, monthly average hourly cloud index at each pixel was processed from 8 a.m. to 4 p.m. during 2012-2021 using the data from MTSAT satellite between 2012-2015 and that from Himawari-8 satellite between 2016-2021. For modelling and validation, averaged values of cloud index at 3×3 pixels over each UV ground-based stations were used. An example of variation of cloud index is shown in Figure 36. It can be observed that cloud index is very low in the dry season and higher in the wet season.

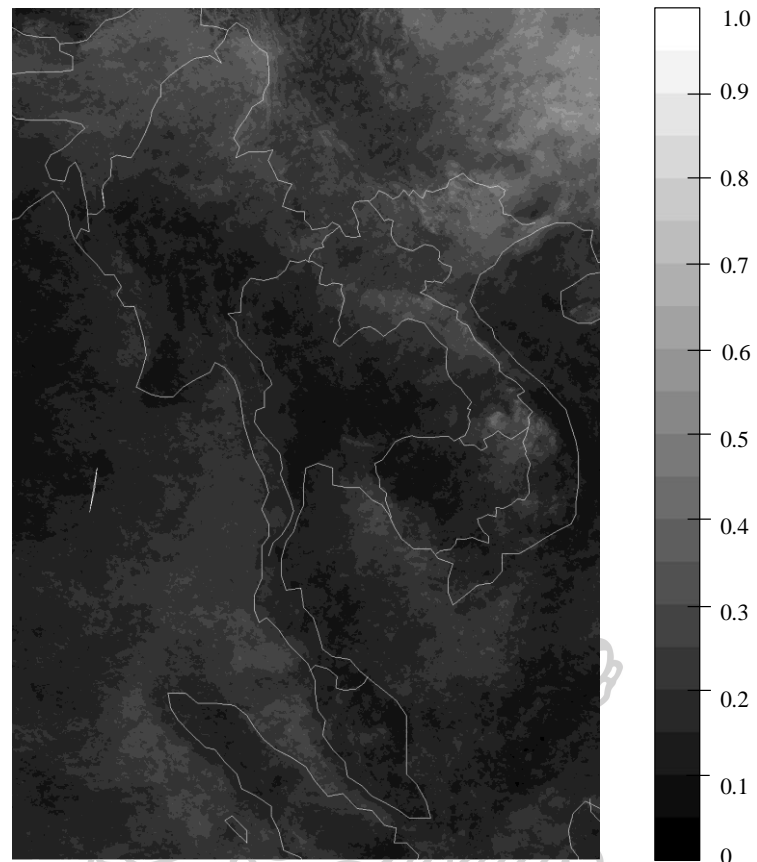


Figure 35 Image of the cloud index.

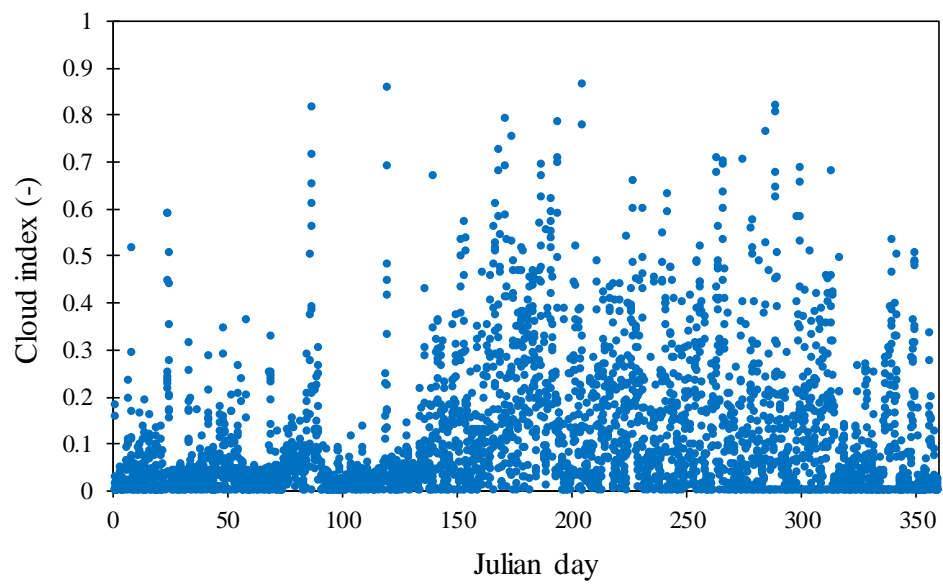


Figure 36 Example of the variation of cloud index at Nakhon Pathom station in 2016.

4) Total ozone column

Total ozone column used in this work was measured by Ozone Monitoring Instrument (OMI) onboard AURA satellite (Figure 37). Due to AURA satellite is a polar orbiting satellite, it passes over the same area only 1-2 times per day so that the total ozone column data was only measured 1-2 times per day. The daily ozone data can be downloaded at <https://acd-ext.gsfc.nasa.gov/anonftp/toms/omi/data/Level3e/ozone/>. The data covers the global area with a resolution of 0.25×0.25 degree.

In this thesis, the total column ozone data during 2012-2021 were downloaded and sectorized for the region of Thailand, similar to the cloud index data. Due to the total ozone column providing from OMI/AURA is in daily basis, in this thesis, total ozone column was assumed to be constant during a day. Then, these data were averaged to be monthly data. An example of daily total ozone is shown in Figure 38.

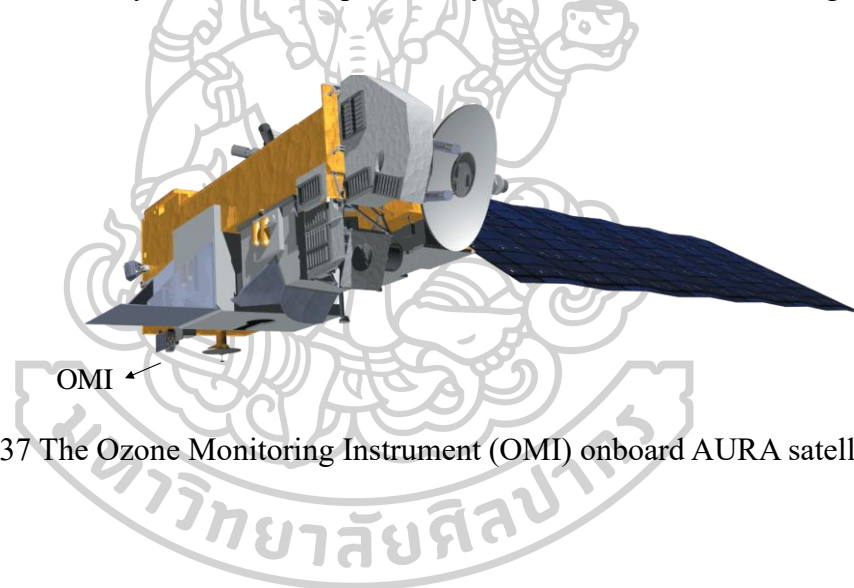


Figure 37 The Ozone Monitoring Instrument (OMI) onboard AURA satellite.

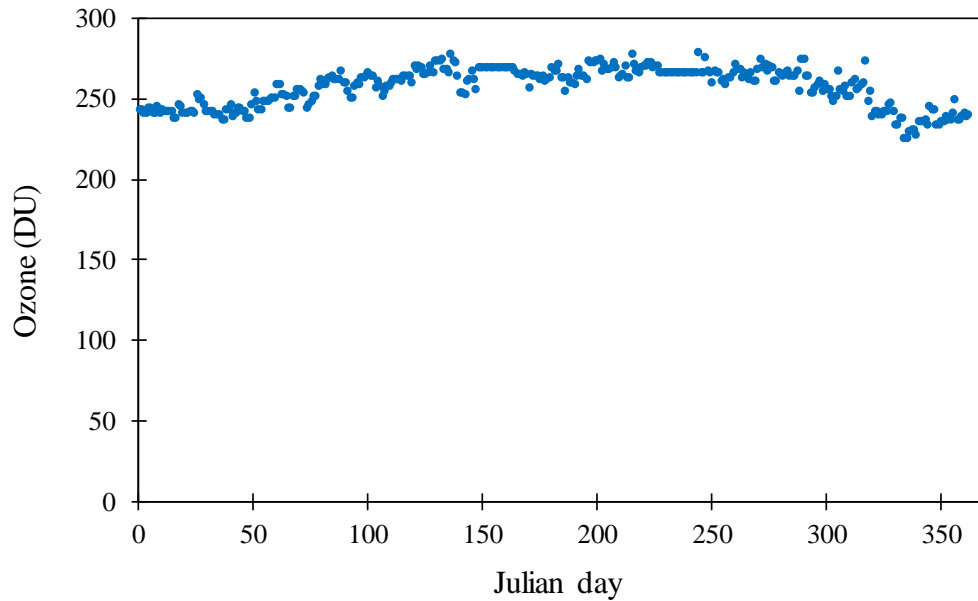


Figure 38 Example of the seasonal variation of ozone at Nakhon Pathom station in 2016.

5) Extraterrestrial vitamin D weighted solar ultraviolet irradiance

Vitamin D weighted UV irradiance at the top of the atmosphere can be calculated (Iqbal, 1983) from Eq. (3.21).

$$DUV_0 = DUV_{SC} E_0 \cos \theta_z \quad (3.21)$$

where DUV_0 = the extraterrestrial vitamin D weighted solar UV irradiance (mW/m^2)

DUV_{SC} = the vitamin D weighted UV solar constant ($11.34 mW/m^2$)

E_0 = the eccentricity correction factor (-)

θ_z = the solar zenith angle (degree).

The eccentricity correction factor depends on the day of year as shown in Figure 39 and this factor can be calculated from an empirical equation represented by (Spencer, 1971).

$$E_0 = 1.000110 + 0.034221\cos\Gamma + 0.001280\sin\Gamma + 0.000719\cos2\Gamma + 0.000077\sin2\Gamma \quad (3.22)$$

where Γ = the day angle (radian).

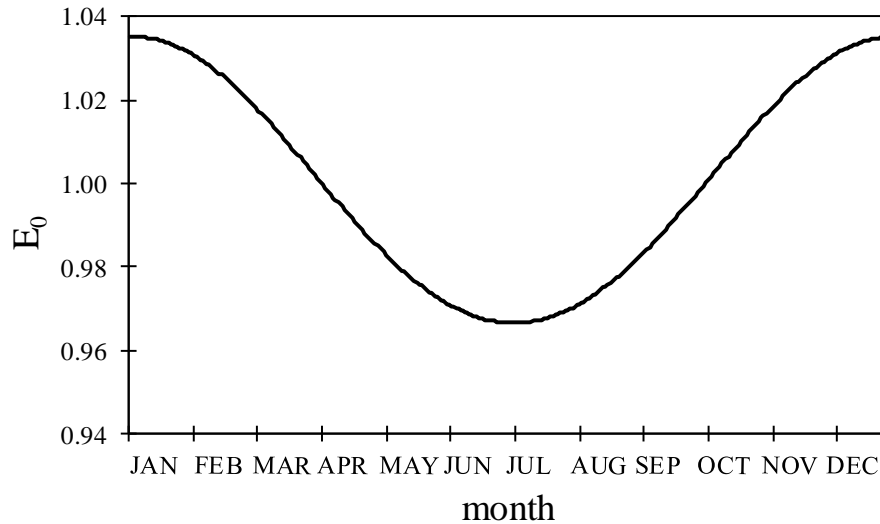


Figure 39 The variation of the eccentricity correction factor (E_0) in a year.

3.2 Empirical model for estimating solar ultraviolet radiation for vitamin D synthesis

Development of models for accurately estimating of solar ultraviolet radiation for vitamin D synthesis is important because it can help to estimate the DUV in regions that instrument is not available. For Thailand, there are few studies about DUV. Therefore, this research will develop an empirical model for estimating solar ultraviolet radiation for vitamin D photosynthesis. The details are described as follows.

Monthly average hourly data of the solar ultraviolet radiation for vitamin D synthesis (DUV) and atmospheric parameters that effect the DUV consisting of aerosol optical depth at 340 nm (AOD_{340}), cloud index (n), total ozone column (O_3), air mass (m_a), zenith angle (θ_z), and extraterrestrial vitamin D weighted solar ultraviolet irradiance (DUV_0) at the four stations (Chiang Mai, Nakhon Pathom, Ubon Ratchathani and Songkhla) during 8 a.m. to 4 p.m. in years 2014 to 2016 were gathered. All datasets were normalized by their highest values. Afterward, the relation of DUV with each parameter was considered leading to a form showing a relation

between the DUV and these parameters. This form was used in Statistica program to obtain coefficients giving the best result. The empirical model in this work was presented as

$$\text{DUV} = [\text{DUV}_0' (a_0 \cos\theta_z^{a_1} + a_2 e^{m_a'} + a_3 O_3' + a_4 \text{AOD}_{340}' + a_5 n)(1 - n)] \times 800 \quad (3.23)$$

where DUV = the solar ultraviolet radiation for vitamin D synthesis (mW/m²)
 DUV_0' = the normalized extraterrestrial vitamin D weighted solar ultraviolet irradiance (-)
 $\cos\theta_z$ = the cosine of solar zenith angle (-)
 m_a' = the normalized air mass (-)
 O_3' = the normalized total ozone column (-)
 AOD_{340}' = the normalized aerosol optical depth at the wavelength 340 nm (-)
 n = the cloud index (-)
 a_0, a_1, a_2, a_3, a_4 and a_5 = the coefficients of the equation. Their values and statistic values are presented in Table 2.

Table 2 The coefficient values and statistic values.

coefficient	value	t-value	p-value
a_0	1.095	21.862	0.00
a_1	1.394	12.255	0.00
a_2	0.864	9.944	0.00
a_3	-1.292	-14.072	0.00
a_4	-0.672	-15.226	0.00
a_5	0.944	35.028	0.00

3.3 Validation of the empirical model for estimating solar ultraviolet radiation for vitamin D synthesis

For the validation of the model, the monthly average hourly data of AOD_{340} , n , O_3 , m_a , θ_z and DUV_0 in years 2017-2018 from 8 a.m. to 4 p.m. were used for calculating the DUV. The DUV estimated from the model was compared with the DUV from the measurement at each station (Chiang Mai, Nakhon Pathom, Ubon Ratchathani and Songkhla) and all stations. In addition, the RMSD and the MBD were used to represent the differences between the two datasets. The validation results are shown in Figure 40-44.

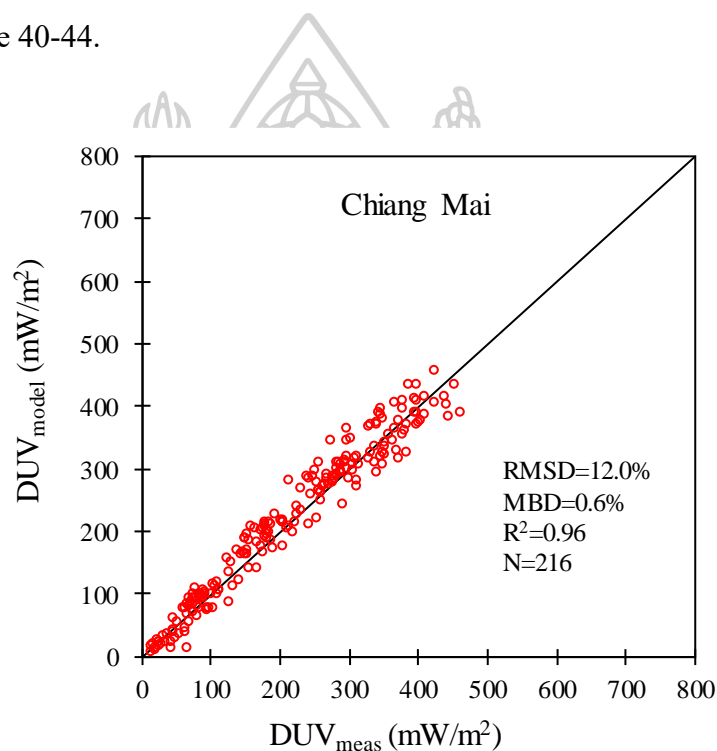


Figure 40 Comparison of the DUV from the measurement (DUV_{meas}) and the DUV from the model (DUV_{model}) at Chiang Mai station.

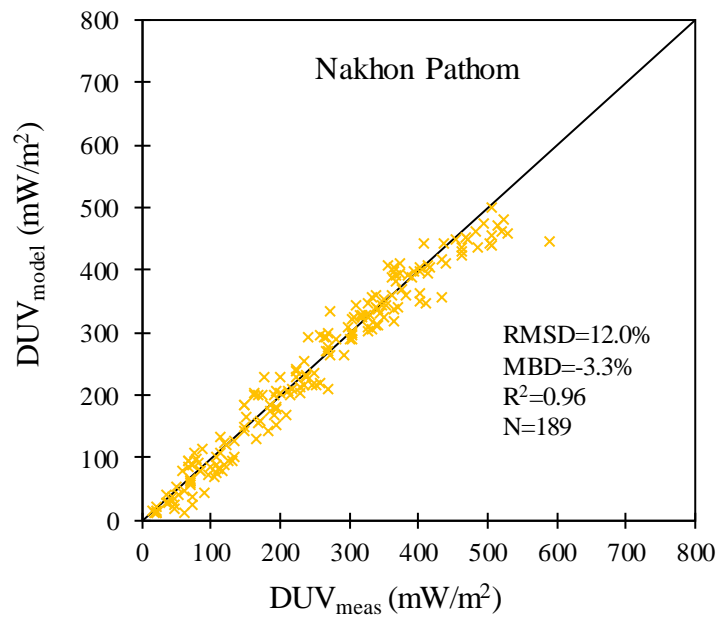


Figure 41 Comparison of the DUV from the measurement (DUV_{meas}) and the DUV from the model (DUV_{model}) at Nakhon Pathom station.

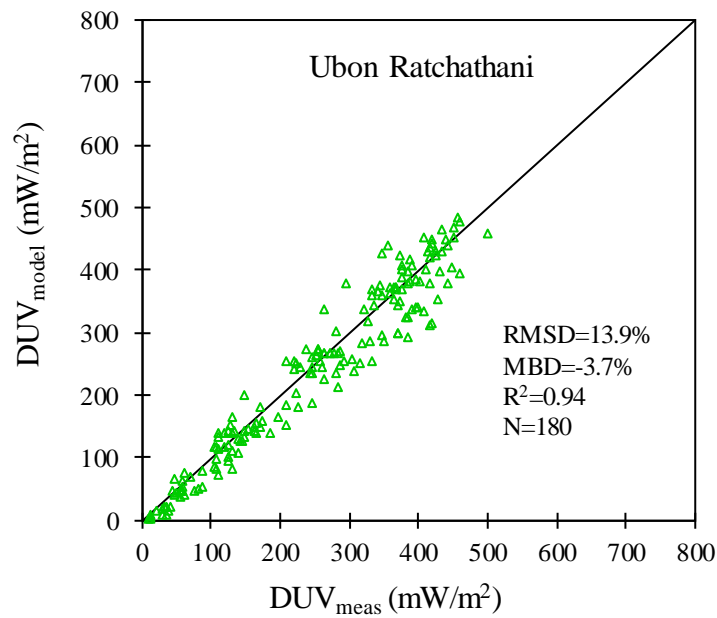


Figure 42 Comparison of the DUV from the measurement (DUV_{meas}) and the DUV from the model (DUV_{model}) at Ubon Ratchathani station.

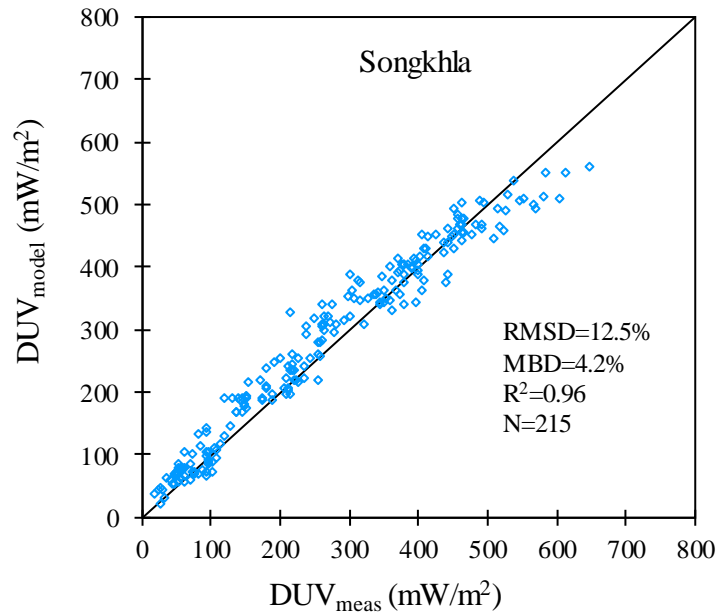


Figure 43 Comparison of the DUV from the measurement (DUV_{meas}) and the DUV from the model (DUV_{model}) at Songkhla station.

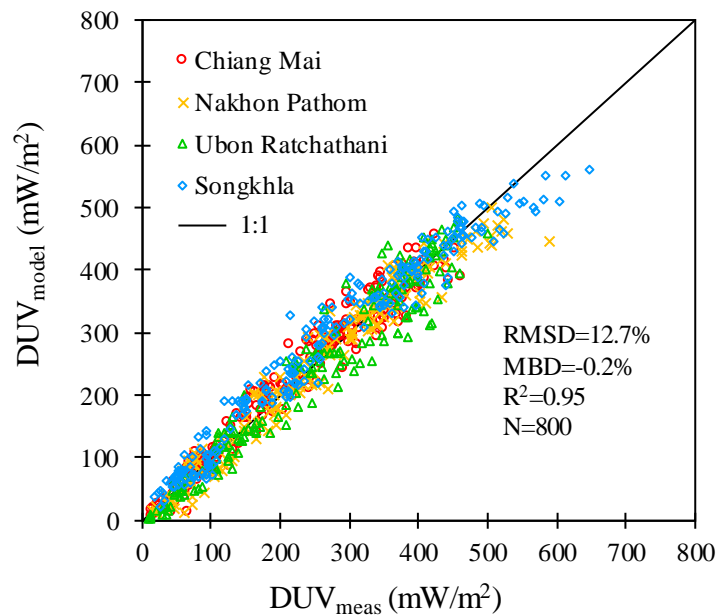


Figure 44 Comparison of the DUV from the measurement (DUV_{meas}) and the DUV from the model (DUV_{model}) at the four stations.

The validation results show that the DUV from the measurement and the model was consistent for all stations. Songkhla station has the highest radiation. The RMSD of Chiang Mai station, Nakhon Pathom station, Ubon Ratchathani station, and Songkhla station were found to be 12.0%, 12.0%, 13.9% and 12.5%, respectively. The MBD were 0.6%, -3.3%, -3.7% and 4.2% for Chiang Mai station, Nakhon Pathom station, Ubon Ratchathani station and Songkhla station, respectively. For the RMSD and the MBD of the combined data from all stations were 12.7% and -0.2%, respectively. The results show that this empirical model can accurately estimate the DUV for all regions of the country.

3.4 Processing of satellite data from MTSAT and Himawari-8 satellites

To produce the DUV maps, it is necessary to process the satellite data. For the first period (2012-2015), data are from MTSAT and the second period (2016-2021), data are from Himawari-8. In this thesis, these data were sectorized to cover Thailand region. The original data are in satellite projection (Figure 45) which can see the arc of the world. Then, these data were transformed to cylindrical projection (Figure 46) to obtain distance of image matching with latitude and longitude. Afterward, each pixel of satellite image was coordinated (Figure 47) using a geographical cylindrical projection map superimposed and coast lines as references.

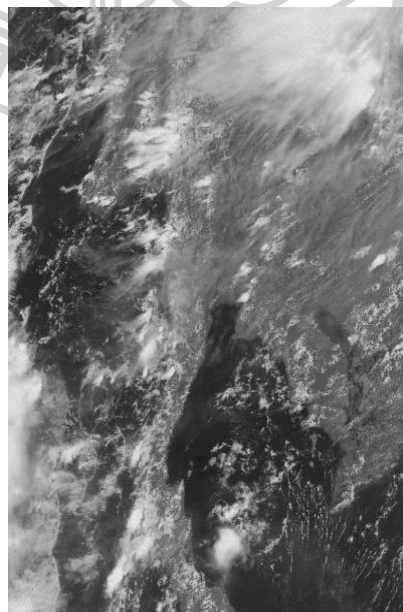


Figure 45 Satellite image in satellite projection.



Figure 46 Satellite image in cylindrical projection.

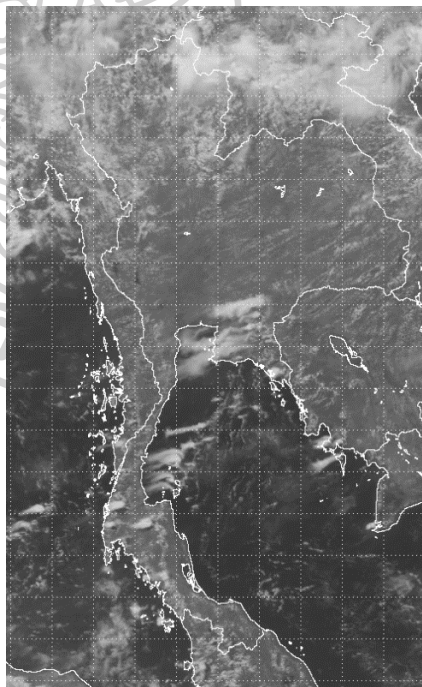


Figure 47 Coordinated satellite image.

3.5 Maps of monthly average hourly solar ultraviolet radiation for vitamin D synthesis

In this work, there are several procedures required to map solar ultraviolet radiation for vitamin D synthesis. The details are described as follows.

Image of cloud index was selected for the region of Thailand. Size of the image is $1,112 \times 1,612$ pixels covering latitude of 0.29°N – 28.71°N and longitude of 90.20°E – 109.80°E . For AOD data retrieved from visibility at 125 meteorological stations, they were interpolated to have monthly average hourly data with a resolution corresponding to cloud index data. In case of O_3 , due to the O_3 data obtained from OMI/AURA providing only daily data with a resolution of $0.25^\circ \times 0.25^\circ$, in this thesis, daily data were averaged to monthly data and these data were interpolated to have $1,112 \times 1,612$ pixels, similar to cloud index data. In addition, $\cos\theta_z$, DUV_0 and m_a were calculated to be maps and each data is equal for every year. All parameters will have grid sizes same as cloud index data.

All parameters were used as input of the empirical model for estimating the DUV for each pixel. Afterward, the DUV maps were resized to 500×800 pixels covering latitude of 5°N – 21°N and longitude of 96°E – 106°E . The maps of long-term monthly average hourly DUV were presented in Figure 48-49.



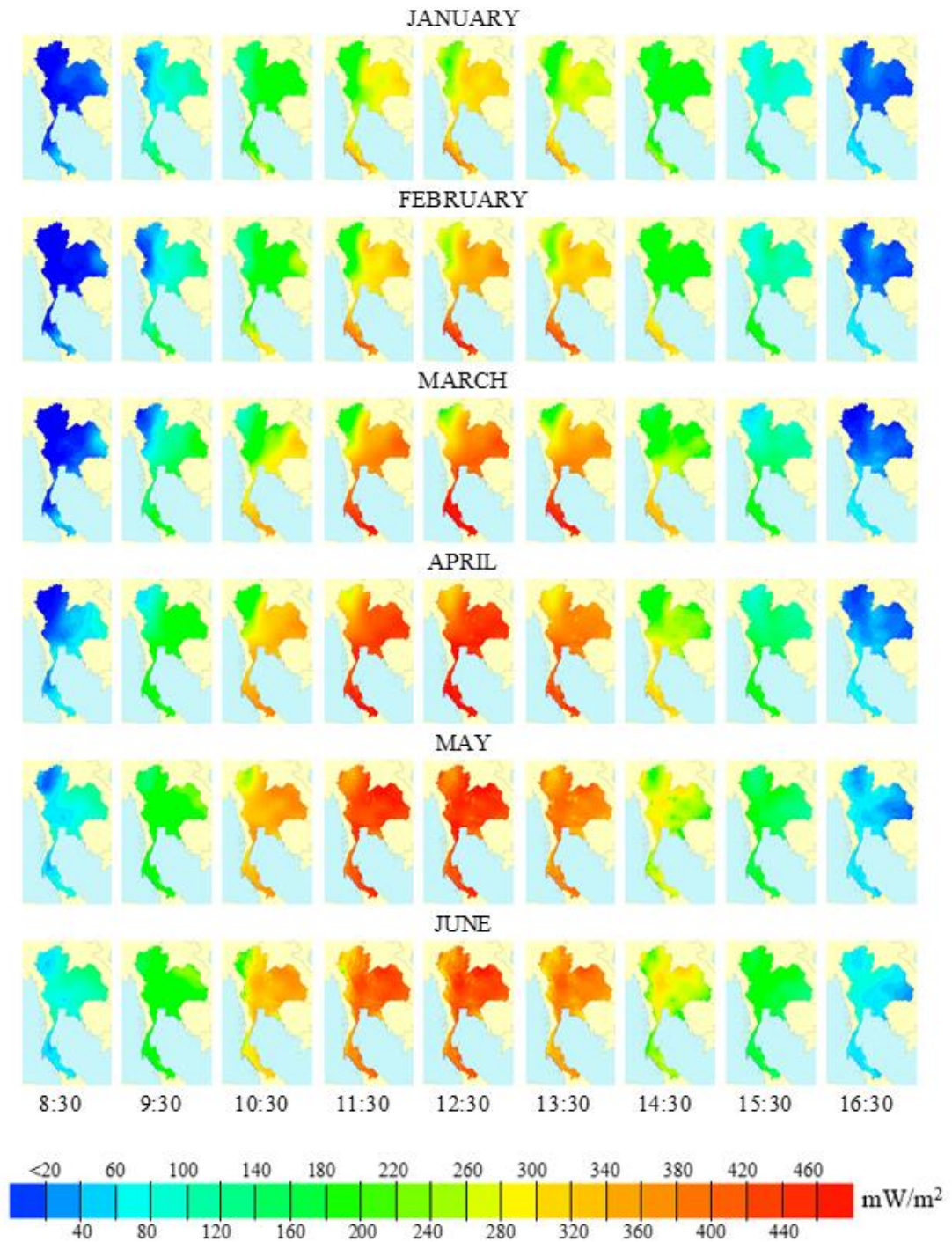


Figure 48 Spatial distribution maps of long-term monthly average hourly vitamin D weighted UV irradiance from 8:30-16:30 local time during January to June.

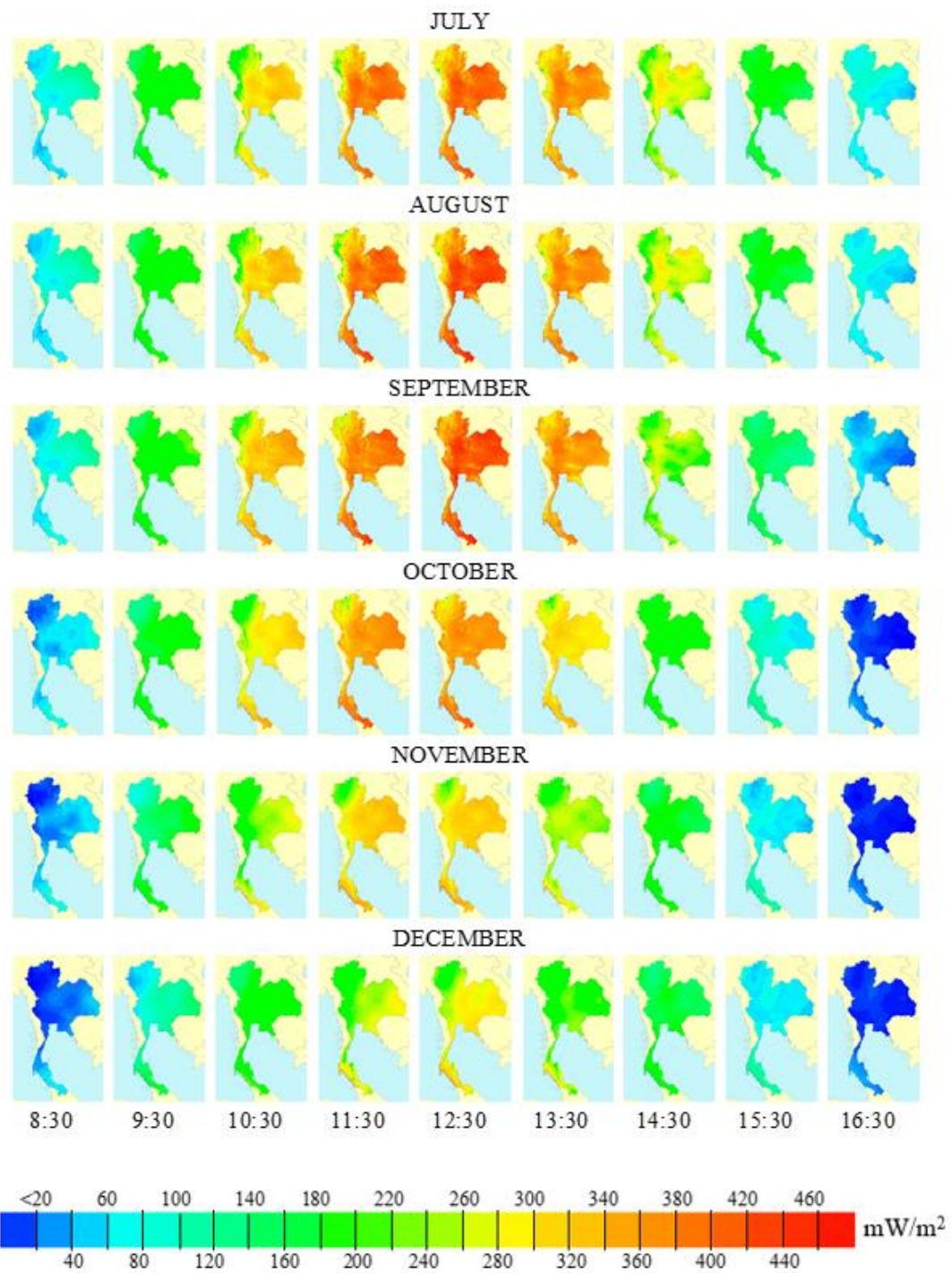


Figure 49 Spatial distribution maps of long-term monthly average hourly vitamin D weighted UV irradiance from 8:30-16:30 local time during July to December.

- Daily variation

The maps show that the DUV increases in morning (8:30-10:30 local time) and the highest value at noon (11:30-13:30 local time) and then the DUV decreases to evening (14:30-16.30 local time). In addition, it is noticed that the DUV in the morning is higher than the DUV in the evening for all months because solar zenith angle in the morning is lower than solar zenith angle in the evening. This can cause optical path length in the morning is lower than in the evening. Thus, the DUV will pass atmospheric path length in the evening more than in the morning. Moreover, in the evening, there is higher aerosol load which can attenuate the solar ultraviolet radiation.

- Seasonal variation

In Thailand, there are three seasons that are summer (mid-February to mid-May), rainy (mid-May to mid-October) and winter (mid-October to mid-February). The maps of DUV present that the DUV is the highest in summer season in April and May. Afterward, the DUV decreases in rainy season due to cloud cover increases. The DUV continuously decreases until winter season. The DUV is the lowest in December because the north pole of the earth turns out from the sun. After that the DUV slightly increases again in January according to the earth's orbit around the sun. In addition, it is noticed that the northern region of Thailand receives the DUV lower than the southern region of Thailand. These is because the southern region located near the equator more than the northern region.

Chapter 4

Conclusion

This work has presented the empirical model for estimating monthly average hourly vitamin D weighted UV radiation in Thailand as a function of aerosol, ozone, cloud, solar zenith angle, air mass, and extraterrestrial vitamin D weighted UV irradiance. For the data of solar zenith angle, air mass, and extraterrestrial vitamin D weighted UV irradiance, they were calculated from well-known equations. Data from satellites consist of ozone from OMI/AURA and cloud index from MTSAT-2 and Himawari-8 satellites. For ground-based data, aerosol optical depth data were obtained from the visibility of 125 meteorological stations in Thailand. The relation between DUV and EUV was developed, and EUV in the main regions of Thailand was converted to DUV used for the modelling and the validation. The validation results show that the DUV from the measurement and the DUV from the model was consistent with root mean square difference and mean bias difference of 12.7% and -0.2%, respectively. The proposed model was used to estimate the monthly average hourly DUV shown as maps. The maps show that the DUV is the highest at noon. The DUV is highest in May while the DUV is lowest in December. In addition, the DUV expand progressively from the south to the north of the country.

Recommendation

Due to the limited number of UV stations, it is recommended that more UV stations especially measurement of UV spectrum should be established in Thailand so that more UV data could be used to improve the knowledge of UV in this country.

Appendix 1

A model for estimating solar ultraviolet radiation for vitamin D photosynthesis at Nakhon Pathom¹

The UV radiation for vitamin D photosynthesis (DUV) is the beneficial radiation but studying about UV radiation is very scarce and to the best of our knowledge there is no work published about UV for vitamin D photosynthesis at Nakhon Pathom. Therefore, this research aims to create an empirical model for estimating hourly DUV based on data at Nakhon Pathom station, Thailand. The details are described as follows.

1. Measurements and Data

A spectrophotometer (Bentham, model DMc150) is installed at the Science Building 1 of Silpakorn University, Nakhon Pathom, Thailand (13.82°N, 100.04°E) (Figure 1(a)).

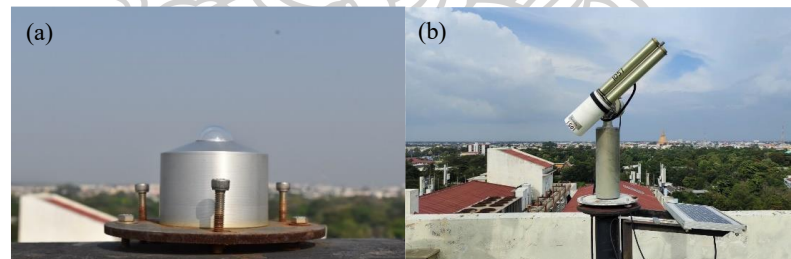


Figure 1. (a) An input optics of a spectrophotometer (Bentham, model DMc150) and (b) a sunphotometer (Cimel, model CE-318) installed at the rooftop of Science Building 1 at Silpakorn University, Nakhon Pathom, Thailand.

This instrument is employed to measure the spectral UV irradiance between 260 and 400 nm, with 1 nm spectral resolution, every 10 minute. An example of the spectral UV irradiance is depicted in figure 2(a). The spectral UV irradiance was multiplied by the spectral response of vitamin D [1] (Figure 2(a)) and then integrated for all

¹ The part of this appendix has been published in Journal of Physics Conference Series (2023) Vol.2431 No.1.

wavelengths to obtain the instantaneous DUV. The 10 minute DUV values were averaged to obtain hourly DUV data from 7 a.m. to 5 p.m. (Figure 2(b)). The hourly DUV data during 2016-2018 were collected for the modeling and validation.

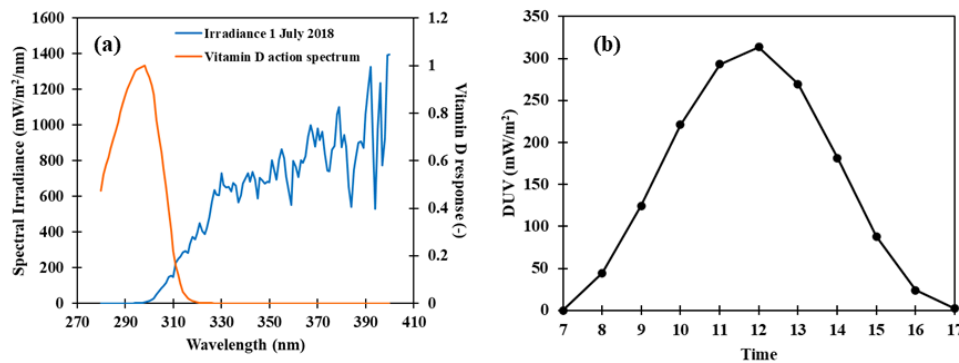


Figure 2. (a) The spectral UV irradiance on 1 July 2018 at noon and the vitamin D synthesis action spectrum and (b) an example of the hourly DUV data on 1 July 2018.

A sunphotometer (Cimel, model CE-318) (figure 1(b)) installed at Nakhon Pathom site was used to measure direct solar radiation at 340, 380, 440, 500, 670, 870, 940 and 1,020 nm which can provide aerosol optical depth (AOD) at these wavelengths [2,3]. In this work, AOD at 340 nm was selected as it is in the UV wavelength. The instantaneous data during 2016-2018 were downloaded from the Aerosol Robotic Network (AERONET) website and the data were averaged to obtain hourly data.

In this work, cloud is represented by cloud index (n) which can be processed from Himawari satellite data using the method of Beyer et al. [4]. The cloud index has values between 0 and 1, where 0 indicates that there is no reflected radiation from cloud and 1 indicates the highest reflected radiation from cloud.

The ozone monitoring instrument (OMI) onboard AURA satellite was also employed to obtain the amount of ozone (O_3).

Another parameter used as an input in the model is air mass which depends on the path length of the radiation penetrating the atmosphere. Air mass relates solar zenith angle and altitude of the location. The lower solar zenith angle, the lower air mass, and the lower altitude, the higher air mass. The air mass can be calculated from the equation given by Kasten [5].

$$m_a = (\cos \theta_z + 0.15(93.885 - \theta_z)^{-1.253})^{-1} e^{(-0.0001184z)} \quad (1)$$

where m_a is air mass (-)
 θ_z is solar zenith angle (degree)
 z is altitude (m).

2. Methodology

The methodology is divided into two sections: modeling and validation. The details are as follows.

2.1 Modelling

The data of DUV, the atmospheric parameters i.e. AOD, n , O_3 , and m_a in years 2016 and 2017 were used for the modelling, as these atmospheric parameters have influenced on the DUV. Firstly, the relation between the DUV and each parameter was tested, and then the relations of these parameters were used as a guideline for generating the model. Various equations showing the DUV as a function of AOD, n , O_3 and m_a in different forms were generated as empirical models. Finally, the empirical model giving the best validation result was chosen. The coefficients of the model were obtained using the “Statistica” software.

2.2 Validation

In this process, independent data were used. The data on AOD, n , O_3 and m_a in year 2018 were input to the model to retrieve hourly DUV. The DUV estimated from the model was compared with that from the measurements. The difference between these two datasets was presented in percentage of root mean square difference (RMSD) and mean bias difference (MBD) relative to mean measured values.

3. Results and discussion

The proposed empirical model for estimating hourly DUV is written as:

$$DUV = a_0 + a_1 n + a_2 m_a^{a_3} + a_4 AOD + a_5 AOD^2 + a_6 AOD m_a + a_7 AOD O_3 m_a \quad (2)$$

where DUV is UV irradiance for vitamin D photosynthesis (mW m^{-2})

n is cloud index (-)

m_a is air mass (-)

AOD is aerosol optical depth at a wavelength of 340 nm (-)

O_3 is total column ozone (DU)

$a_0, a_1, a_2, a_3, a_4, a_5, a_6$ and a_7 are the empirical coefficients of the model. The software gives the following values of the coefficients: $a_0 = -48.069 \text{ mW m}^{-2}$, $a_1 = -89.351 \text{ mW m}^{-2}$, $a_2 = 599.085 \text{ mW m}^{-2}$, $a_3 = -1.638$, $a_4 = -230.504 \text{ mW m}^{-2}$, $a_5 = 50.507 \text{ mW m}^{-2}$, $a_6 = 303.552 \text{ mW m}^{-2}$ and $a_7 = -1.051 \text{ mW m}^{-2} \text{ DU}^{-1}$.

From the equation (2), it shows that the DUV decreases when n , AOD, O_3 and m_a increases. The DUV is a linear function with cloud index but the influences of aerosol optical depth and ozone on DUV also depend on air mass. For the validation results, the DUV estimated from the model was plotted against the DUV from the measurement as presented in figure 3.

From figure 3, the model can estimate quite well for low value of DUV. For high value of DUV, the model underestimates DUV value. This may result from the complex effects of aerosol, ozone and air mass together. However, the overall result shows that the DUV predicted from the model reasonably agrees with the measurements with RMSD of 17.1% and MBD of -9.2%. This shows that the empirical model proposed in this work can be used to estimate hourly DUV at this site.

In order to estimate the DUV at a given hour and day, the data of AOD, n , O_3 and m_a at the given hour and day, and the coefficients are required as inputs. Then the DUV can be calculated from the model. However, to estimate the DUV at any different climate region, the coefficients may change and thus they need to be revised.

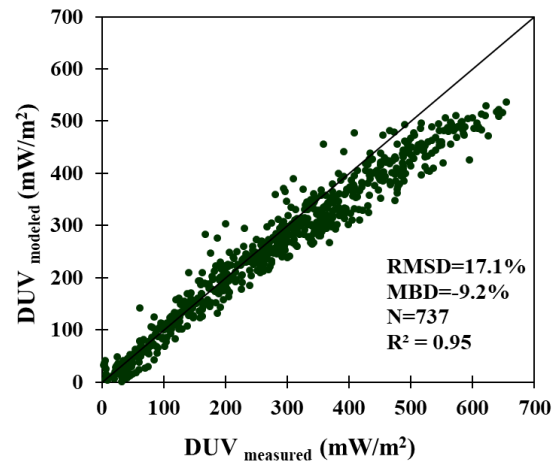


Figure 3. The comparison between the DUV from the model (DUV_{modeled}) and from the measurement (DUV_{measured}).

4. Conclusion

In this research, the empirical model was developed to estimate hourly DUV from cloud, aerosol, ozone and air mass. The proposed model can estimate DUV in consistent with the measurement with RMSD of 17.1% and MBD of -9.2%. In the future, the model is required to be adjusted to estimate DUV with a better accuracy.

Acknowledgments

This research is financially supported by Thailand Science Research and Innovation (TSRI) National Science, Research and Innovation Fund (NSRF) (Fiscal Year 2022).

References

- [1] Miyauchi M and Nakajima H 2016 Determining an effective UV radiation exposure time for vitamin D synthesis in the skin without risk to health: simplified estimations from UV observations *Photochem. Photobiol.* **92** 863–9
- [2] Holben B N *et al* 1998 AERONET-A Federated instrument network and data archive for aerosol characterization *Remote Sens. Environ.* **66(1)** 1–16
- [3] Xun L, Lu H, Qian C, Zhang Y, Lyu S and Li X 2021 Analysis of aerosol optical depth from sun photometer at shouxian, china *Atmosphere* **1226** 1–14

- [4] Beyer H G, Costanzo C and Heinemann D 1996 Modifications of the heliosat procedure for irradiance estimates from satellite images *J. Sol. Energy* **56** 207–12
- [5] Kasten F 1966 A new table and approximate formula for relative optical air mass *Arch. Meteorol. Geophys. Bioklimatol. Ser. B* **14** 206–23



Appendix 2

Solar ultraviolet radiation for psoriasis treatment at Nakhon Pathom province²

Psoriasis is one of the long-term chronic skin disease that causes suppression of immune system. Usually exposure of the skin to the artificial UVB radiation is one of the treatment. Alternative, lot of light exposure is also important. However, doctor who treats this disease should know level of the UV in the sun light. This paper focuses on the study of UV in natural sun light in Thailand. The study used the measurement of UV radiation and the analysis of its variation. The study consisted of several tasks. The details of each tasks are described as follows.

1. Materials and Method

A spectroradiometer (Bentham Instrument, model DMc150) installed at Silpakorn University, Nakhon Pathom province (13.82 °N, 100.04 °E, 39.4 msl), was used to measure solar spectral irradiance covering the wavelength of 260-420 nm with the spectral resolution of 1 nm. The pictorial view of the instrument is presented in Figure 1.



Figure 1 A pictorial view of the spectroradiometer installed at Nakhon Pathom a) input optics b) the monochromator and detector

² The part of this appendix has been published Journal of Research on Science and Technology(JARST) (2022) Vol.21 Issue 1.

The input optics is located on a rooftop of the science building of Silpakorn University. These input optics are connected to the double monochromator, the photomultiplier, and the detector. The electronic signals from the detector were transferred and displayed on a processing computer, and Benwin+ software was installed on the processing computer to control the system and for the data acquisition. This instrument was calibrated using a deuterium standard lamp once per month.

To obtain the UV data responding to psoriasis treatment, the current signals recorded in the processing computer every ten minutes were converted to spectral irradiance using its sensitivity retrieved from the calibration. This spectral irradiance was converted to effective doses for the anti-psoriatic effect of ultraviolet radiation using the following expression.

$$\text{Dose}_{\text{ANTIPSOR}}(t_2, t_1) = \int_{t_1}^{t_2} \left(\int_{280\text{nm}}^{400\text{nm}} I_{\lambda}(t, \lambda) R_{\lambda} d\lambda \right) dt \quad (1)$$

where $\text{Dose}_{\text{ANTIPSOR}}$ is an anti-psoriasis-weighted dose in the period t_1 to t_2 , $I_{\lambda}(t, \lambda)$ is spectral irradiance at time t and wavelength λ , and R_{λ} is anti-psoriasis action spectrum function.

The anti-psoriasis action spectra are defined as follows (1):

$$R_{\lambda} = \begin{cases} 0.6504 \times 10^{-0.6304(296-\lambda)} & \lambda < 296 \text{ nm} \\ 1.0000 \times 10^{-0.0467(300-\lambda)} & 296 \leq \lambda < 300 \text{ nm} \\ 1.0000 \times 10^{-0.1067(\lambda-300)} & 300 \leq \lambda < 304 \text{ nm} \\ 0.3743 \times 10^{-0.1571(\lambda-304)} & 304 \leq \lambda < 313 \text{ nm} \\ 0.0144 \times 10^{0.08233(313-\lambda)} & 313 \leq \lambda < 330 \text{ nm} \\ 0.0057 \times 10^{0.00937(330-\lambda)} & 330 \leq \lambda < 400 \text{ nm} \end{cases} \quad (2)$$

An example of the spectral irradiance and anti-psoriasis action function is presented in Figure 2, which can be seen that the most effective spectral irradiance for anti-psoriasis is in the UV-B wavelength.

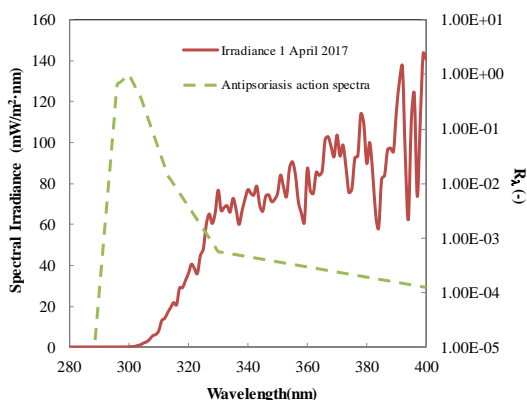


Figure 2 An example of spectral UV irradiance at a given time on 1 April 2017 at 8 a.m. and the anti-psoriasis action spectra (R_{λ})

2. Results and Discussion

In this study, the anti-psoriasis weighted doses retrieved from the spectroradiometer were used for three years, from 1 January 2016 to 31 December 2018. The dose within an hour was obtained from 7 a.m. to 6 p.m. At each month, the hourly anti-psoriasis UV doses at the same period were averaged to obtain monthly average hourly data and then plotted against the local time to investigate the diurnal variation. For the seasonal variation analysis, the monthly data were plotted against the month for each period.

- The diurnal variation

The diurnal variation of the anti-psoriasis UV doses averaged during 2016-2018 are presented in Figure 3. The results indicate that the UV doses increase from the early morning to reach the maximum value during noontime and decrease until evening. This is mainly influenced by the position of the sun. In the morning and evening, the sun is relatively low, and thus path length of solar radiation in the atmosphere is relatively large compared to the noontime. As a result, the maximum anti-psoriasis UV doses are 77.6, 76.9, and 52.4 mJ/cm^2 in the summer (February-May), rainy (June-October), and winter (November-January) seasons, respectively.

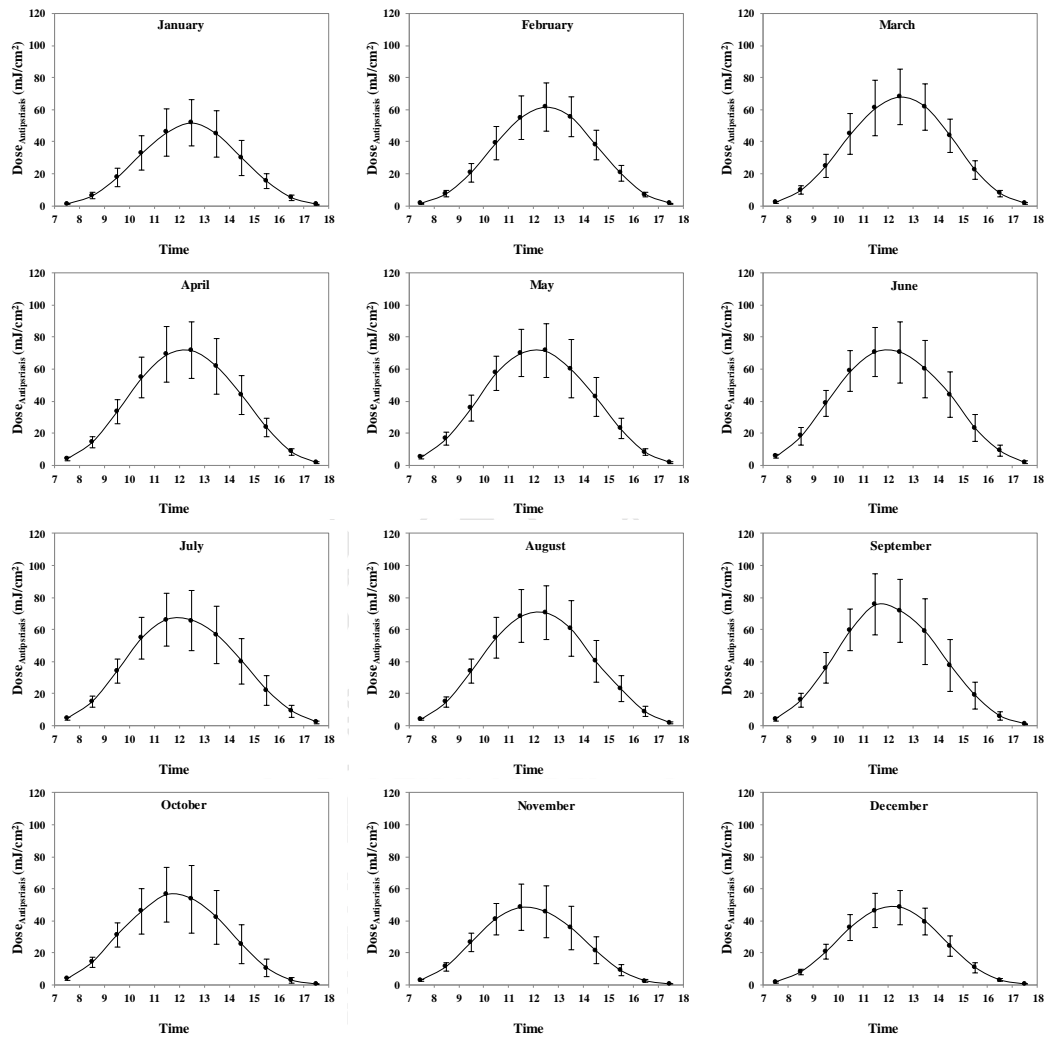


Figure 3 The diurnal variation of anti-psoriasis UV doses at Nakhon Pathom during 2016-2018

- Seasonal variation

The seasonal variation of the hourly anti-psoriasis UV dose averaged during 2016-2018 is shown in Figure 4 from 7 a.m. to 6 p.m. In addition, the threshold dose (i.e., 45 mJ/cm^2) used for the treatment of psoriasis proposed by (1) was also drawn in the figures to present the potential of the solar UV dose for the psoriasis treatment in Thailand.

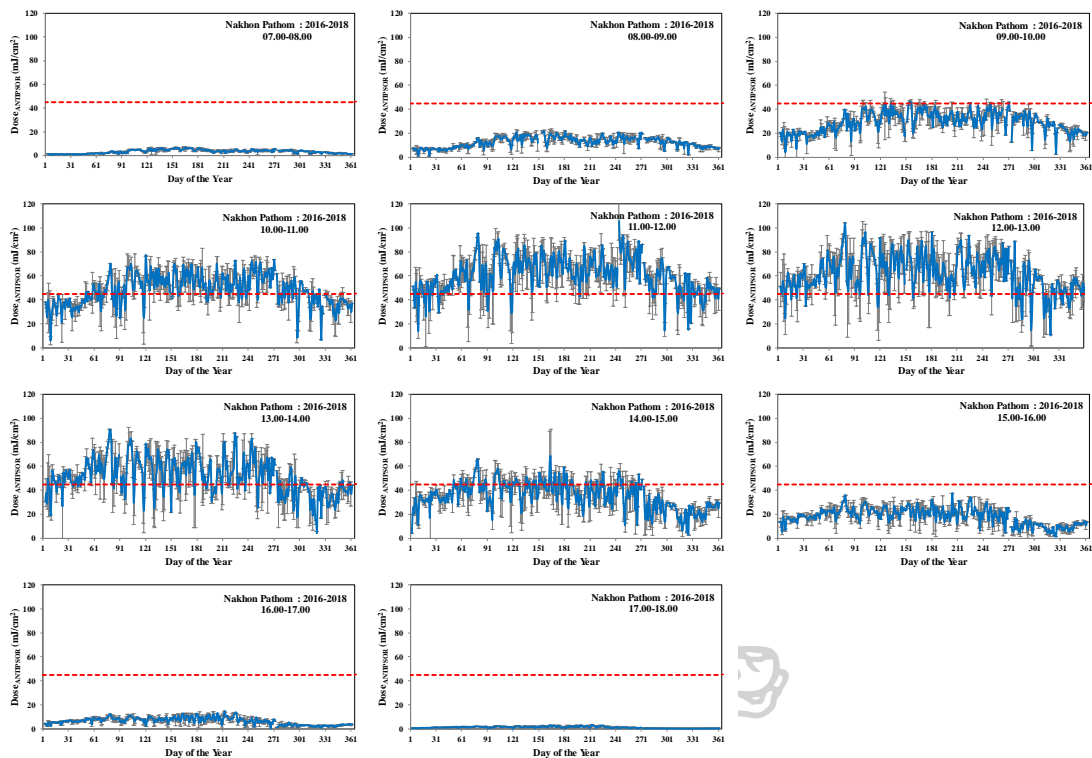


Figure 4 The seasonal variation of hourly anti-psoriasis UV doses from 7 a.m. to 6 p.m. at Nakhon Pathom (The red dash line indicates the threshold of UV dose for the treatment)

The results show seasonal variation in which the anti-psoriasis UV doses are relatively high from March to October and relatively low from November to February. This is mainly because of the position of the sun in the sky. The solar zenith angle is relatively high from March to October, resulting in small solar path length and solar extinction (2-4). In addition, the figure represents that the potential periods to treat psoriasis using sunlight within 1 hour are from 10 a.m. - 2 p.m. from March to October when the value of UV dose is above the threshold value. However, patients can exposure the sun at other times for a longer period depending on the direction of their dermatologists. It is noted that the threshold used in this work was defined in (1) for mid-latitude at San Diego (32.77°N , 117.20°W) and high-latitude at Belsk (51.83°N , 20.78°E), which may not perfectly suit for Thailand. This threshold then should be further justified for low-latitude as Thailand. Moreover, excessive exposure is harmful. Therefore, the optimal exposure time for psoriasis treatment should not exceed the time leading to hazardous health (5).

- *The empirical model*

According to the limitation of the ground-based spectroradiometer, they can be used to measure the UV doses to treat psoriasis. In contrast, UV index (UVI) has been measured broadly. Therefore, a simple model used to estimate the anti-psoriasis UV doses is needed. In this study, an empirical model was developed and validated. UVI was calculated following the method in (6) using the DMc150 spectroradiometer at the same site. Then hourly anti-psoriasis UV dose was plotted against the UV index using 2016 and 2017. The graph between the anti-psoriasis UV dose and the UV index is shown in Figure 5, and the linear least square expression can be written as follows:

$$\text{DOSE}_{\text{ANTIPSOR}} = 6.5713\text{UVI} \quad (3)$$

$\text{DOSE}_{\text{ANTIPSOR}}$ is the anti-psoriasis UV dose (mJ/cm^2), and UVI is the UV index (unitless).

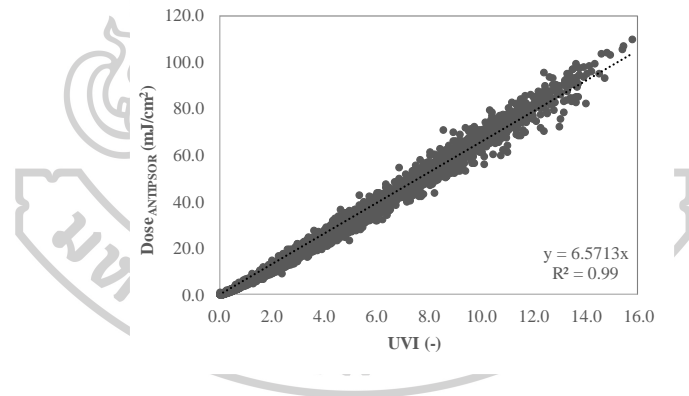


Figure 5 The relationship between anti-psoriasis UV dose (DosePsoriasis) and UV index (UVI) in 2016 and 2017

For the model validation, the anti-psoriasis UV doses calculated from the proposed model were compared with those measured from the spectroradiometer in 2018. The validation result presented in Figure 6 shows that the model can estimate the anti-psoriasis reasonably compared to a method in (7) that used the satellite data approach.

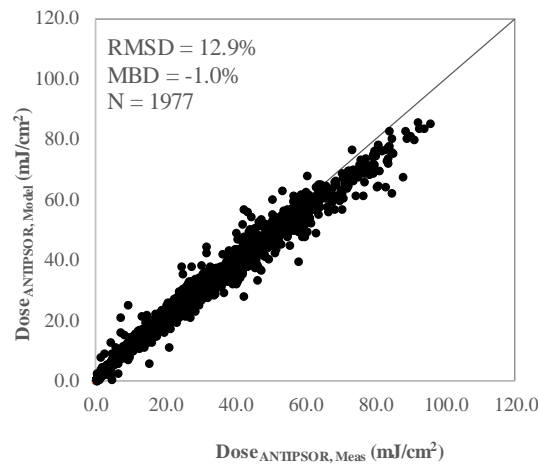


Figure 6 The comparison between the anti-psoriasis UV dose from the model ($Dose_{ANTIPSOR, Model}$) and the measurement ($Dose_{ANTIPSOR, Meas}$)

3. Conclusion

The anti-psoriasis effective UV dose at Nakhon Pathom was investigated. The results show that the UV dose was diurnal and seasonal variations and relatively high from 10 a.m. to 2 p.m., especially between March and October. Therefore, this period is likely to have the potential for treating psoriasis and several inflammatory skin conditions. However, the UV doses in other regions may differ depending on the location, geography, and atmospheric conditions. Therefore, the UV dose in other regions of Thailand should be further investigated for the extended development of a national heliotherapy protocol for psoriasis in Thailand. In Thailand, Heliotherapy using a sustainable abundance of solar energy would transform medical practice on light-based treatments, which is considered enormously beneficial but time-consuming and required commitment into perhaps one of the supervised primary aids at home.

Acknowledgements

The authors would like to thank the Faculty of Sciences, Silpakorn University, for the financial support (Grant number SRF-JGR-2561-03) (to SB) and the Royal College of Physicians of Thailand (to EB). We gratefully acknowledge undergraduate senior project students of the Department of Physics, Silpakorn University, for their help processing data, and staff of the Photodermatology Unit, Division of

Dermatology, Department of Medicine, Chulalongkorn University for assistance on medical service perspectives of psoriasis treatment.

References

1. Krzyscin JW, Jarosławski J, Rajewska-Wiech B, Sobolewski PS, Narbutt J, Lesiak A, et al. Effectiveness of heliotherapy for psoriasis clearance in low and mid-latitude regions: a theoretical approach. *J Photochem Photobiol B, Biol.* 2012;115:35–41.
2. Janjai S, Buntoung S, Masiri I, Wattan R. Mapping solar ultraviolet radiation from satellite data in a tropical environment. *Remote Sens Environ.* 2010;114(3):682-91.
3. Janjai S, Kirdsiri K, Masiri I, Nunez M. An investigation of solar erythemal ultraviolet radiation in the tropics: a case study at four stations in Thailand. *Int J Climatol.* 2010;30:1893-903.
4. Iqbal M. An introduction to solar radiation. New York: Academic Press; 1983.
5. Miyauchi M, Nakajima H. Determining an Effective UV Radiation Exposure Time for Vitamin D Synthesis in the Skin Without Risk to Health: Simplified Estimations from UV Observations. *Photochem Photobiol.* 2016;92(6):863-869.
6. World Health Organization (WHO), World Meteorological Organization (WMO), United Nations Environment Programme (UNEP), International Commission on Non-Ionizing Radiation Protection (ICNIRP), Global Solar UV Index: A Practical Guide, Watch No 95, WMO/TD No. 625, Geneva, Switzerland. 2002.
7. Krzyscin JW, Guzikowski J, Czerwinska A, Lesiak A, Narbutt J, Jarosławski J, et al. 24 hour forecast of the surface UV for the antipsoriatic heliotherapy in Poland. *J Photochem Photobiol B, Biol.* 2015;148:136-44.

Appendix 3

Development of empirical models for calculating global and diffuse erythema weighted solar ultraviolet radiation under clear sky conditions in Thailand ³

Global and diffuse UV erythema weighted solar radiation under clear sky is an importance such as forecasting the UV radiation and indication effect of atmosphere's components on radiation from maximum radiation of days. Therefore, the objective of this study is to develop models for calculating global and diffuse EUV solar radiation under clear sky condition. The details are described as follows.

1. Measurements and Data

Various data sets were used in this study. The details of these data sets are explained as follows.

1) Global and diffuse EUV solar radiation

Our research group established solar monitoring stations in four main regions of Thailand to obtain solar radiation and atmospheric data for our atmospheric and solar energy research. These regions include Chiang Mai (CM; 18.78°N, 98.98°E) in the Northern region, Ubon Ratchathani station (UB; 15.25°N, 104.87°E) in the North-eastern region, Nakhon Pathom station (NP; 13.82°N, 100.04°E) in the Central region, and Songkhla station (SK; 7.2°N, 100.60°E) in the Southern region. Global and diffuse EUV solar radiation, as well as other band and spectral solar radiation, are measured at these stations. At each station, a broadband UV instrument (Solar Light, model 501A) was installed on a pole at a height of 1.8 m on the rooftop of the station building to measure the global EUV solar radiation at the station. Voltage signals from the instrument were captured every second using a datalogger (Yokogawa, model DX2000). A broadband UV instrument with the same model was installed on a sun tracker (Kipp&Zonen, model 2AP) with a shade ball to block the direct UV component to measure diffuse EUV radiation, and the voltage signals from the UV broadband instrument were captured every second by the same datalogger used to record the

³ The part of this appendix has been submitted in Journal of Science, Engineering and Health Studies

global EUV radiation. These voltage signals were converted to hourly average EUV radiation using the procedure proposed by Webb et al. (2006). The EUV data encompassing the period of January 2011 and December 2020 was used in this study.

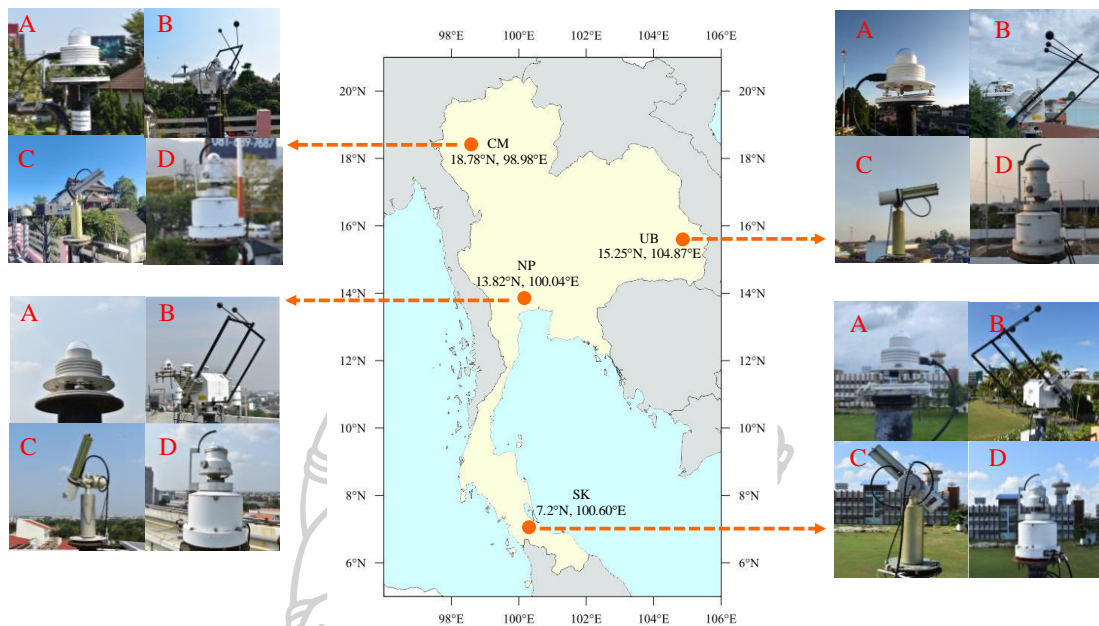


Figure 1 Instruments and locations of the four monitoring sites: (A) UV instruments for measuring global EUV (B) UV instruments for measuring diffuse EUV (C) Sunphotometers, and (D) Skyviews

2) Ozone dataset

Ozone is important for the calculation of EUV radiation at the surface of the earth. In this study, daily total ozone column (O_3) data were acquired from OMI/AURA satellite and downloaded from <ftp://tom.gsfc.nasa.gov/pub/omi/data/ozone/> during the study period. The data at the four stations were extracted and used for modeling and validation.

3) Aerosol dataset

Aerosols significantly affect EUV radiation, especially in highly polluted regions like in most parts of Thailand (Janjai et al., 2012). A sunphotometer (Cimel, model CE-318) was installed at each solar monitoring station to obtain aerosol optical

properties (Figure 1). The data from the sunphotometer was processed by the Aerosol Robotic Network (AERONET). In this study, an aerosol optical depth (AOD) at a wavelength of 340 nm that effects ultraviolet radiation was downloaded from <https://aeronet.gsfc.nasa.gov/>. All point data were averaged to obtain hourly AOD data for use in this study.

4) Sky image dataset

In this study, a Skyview (Prede, model PSV-100) installed at each of our stations (Figure 1) was set to take an image of half of the celestial spheres every five minutes. By using this image, cloud cover, or fraction of clouds in the sky in the octa unit can be obtained. The cloud cover was used to identify the sky conditions, which can be broadly classified into five classes: clear sky (<1 octas), few clouds (1–2 octas), scattered clouds (3–4 octas), broken clouds (5–7 octas), and overcast sky (8 octas) (Grant and Gao, 2003). Therefore, in this study, the data corresponding to the cloud cover equal to 0 were acquired and used as the data under clear sky conditions.

5) Air mass dataset

The atmospheric path that the solar radiation can pass to reach the surface of the earth can be explained using air mass. The air mass is calculated using the following equation (Gueymard, 1993):

$$m_a = m_r \left(\frac{P}{101.325} \right) \quad (1)$$

where m_a denotes the air mass at mean sea level (-), m_r denotes the relative air mass (-) and can be calculated from Eq. (2) presented by Kasten (1965):

$$m_r = [\cos\theta_z + 0.15(93.885 - \theta_z)^{-1.253}]^{-1} \quad (2)$$

where θ_z denotes the solar zenith angle (degree).

From Eq. (1), P denotes the atmospheric pressure (kPa) that can be obtained from Eq. (3) presented by Lunde (1980):

$$\frac{P}{P_0} = \exp(-0.0001184Z) \quad (3)$$

where P_0 denotes the standard pressure (101.325 kPa), and Z denotes the height from mean sea level (m).

2. Method

The hourly global and diffuse EUV solar radiation, aerosol optical depth, air mass, and daily total ozone column under clear sky conditions were acquired for this study. The retrieved data were from the period between 2011 and 2020, and these data were divided into two groups. In the first group, the data acquired between 2011 and 2018 was used for modeling, while in the second group, the data acquired during 2019 to 2020 was used for model validation. For modeling, each data was normalized with a constant value, which is its maximum value. The relationship between the normalized EUV radiation and the other atmospheric parameters was generated using Statistica program to obtain coefficients of empirical models. For model validation, the global, and diffuse EUV solar radiation from calculations were compared with the EUV solar radiation from measurements. Then, the differences between both datasets were presented in terms of root mean square difference (RMSD) and mean bias difference (MBD), as shown in Eq. (4) and Eq. (5), respectively.

$$\text{RMSD} = \sqrt{\frac{\sum_{i=1}^N (\text{EUV}_{\text{model},i} - \text{EUV}_{\text{meas},i})^2}{N}}{\frac{\sum_{i=1}^N \text{EUV}_{\text{meas},i}}{N}}} \times 100\% \quad (4)$$

$$\text{MBD} = \frac{\sum_{i=1}^N (\text{EUV}_{\text{model},i} - \text{EUV}_{\text{meas},i})}{\frac{\sum_{i=1}^N \text{EUV}_{\text{meas},i}}{N}} \times 100\% \quad (5)$$

where $EUV_{\text{model},i}$ denotes the solar erythemal ultraviolet radiation under clear sky conditions from the model, $EUV_{\text{meas},i}$ denotes the solar erythemal ultraviolet radiation under clear sky conditions from the measurement, and N denotes the number of data.

3. Results and Discussion

- Empirical models

In this study, two empirical models were proposed. One is for estimating global EUV radiation and the other is for estimating diffuse EUV radiation under clear sky conditions. The details of each model are as follows.

By using the Statistica program to obtain the best relationship between hourly global EUV and the related atmospheric parameters, the model for estimating the hourly global EUV obtained in this study is presented in Eq. (6).

$$\frac{EUV_g}{EUV_{g \max}} = a_0 + a_1 e^{\left(a_2 \frac{O_3}{O_{3 \max}} + a_3 \frac{AOD_{340}}{AOD_{340 \max}} \right) \frac{m_a}{m_{a \max}}} \quad (6)$$

where EUV_g denotes the global solar erythemal ultraviolet radiation under clear sky conditions (mW/m^2), $EUV_{g \max}$ denotes the maximum global solar erythemal ultraviolet radiation under clear sky conditions ($400 \text{ mW}/\text{m}^2$), O_3 denotes the total ozone column (cm), $O_{3 \max}$ denotes the maximum total ozone column (0.320 cm), AOD_{340} denotes the aerosol optical depth at 340 nm wavelength (-), $AOD_{340 \max}$ denotes the maximum aerosol optical depth at 340 nm wavelength which is equal to 5, m_a denotes air mass (-), and $m_{a \max}$ denotes the maximum air mass which is equal to 20. a_0 , a_1 , a_2 , and a_3 denote the coefficients of the model ; $a_0 = 0.0380$, $a_1 = 5.7345$, $a_2 = -50.1048$, and $a_3 = -36.3765$. These coefficients are 95% confidence level.

Similarly, the best relationship between hourly diffuse EUV radiation under clear sky conditions and the related parameters was obtained in this study. The model for estimating the hourly diffuse EUV radiation is presented in Eq. (7).

$$\frac{EUV_d}{EUV_{d \max}} = a_0 + a_1 \frac{O_3}{O_{3 \max}} + a_2 \frac{AOD_{340}}{AOD_{340 \max}} + a_3 \left(\frac{m_a}{m_{a \max}} \right)^{a_4} \quad (7)$$

where EUV_d denotes the diffuse solar erythemal ultraviolet radiation under clear sky conditions (mW/m^2), $EUV_{d_{max}}$ denotes the maximum diffuse solar erythemal ultraviolet radiation under clear sky conditions ($300 mW/m^2$). a_0 , a_1 , a_2 , a_3 , and a_4 denote the coefficients of the model; $a_0 = 0.3051$, $a_1 = -0.3488$, $a_2 = -0.2784$, $a_3 = 0.0018$, and $a_4 = -1.9211$. These coefficients are also 95% confidence level.

- *Validation results*

The performances of the models were examined by comparing the UV irradiance estimated from the models with those obtained from the ground-based measurements using independent datasets.

The comparison results between hourly global EUV irradiances from the proposed model and the ground-based measurement at the four monitoring sites are shown in Figure 2. The differences between the two datasets in terms of RMSD and MBD are 15.8% and -5.5%, respectively. The validation results for the diffuse EUV radiation are shown in Figure 3. The RMSD and MBD are 14.9% and 1.1%, respectively.

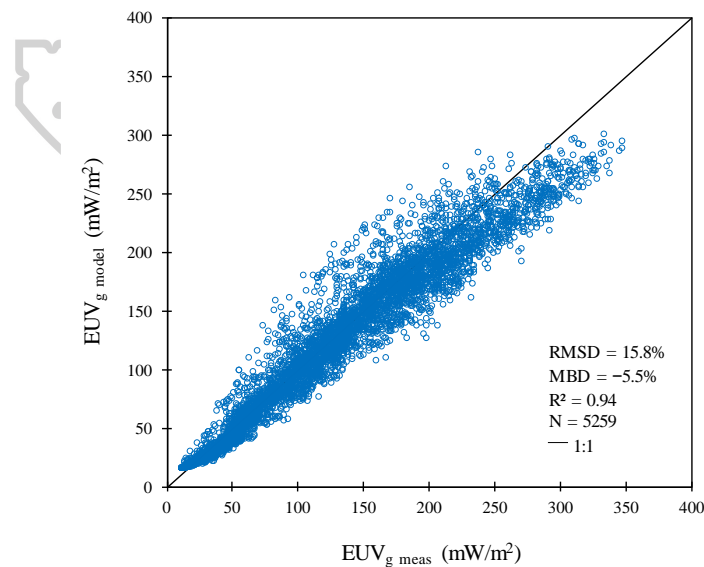


Figure 2 Comparison between global EUV from the model ($EUV_{g_{model}}$) and the measurements ($EUV_{g_{meas}}$)

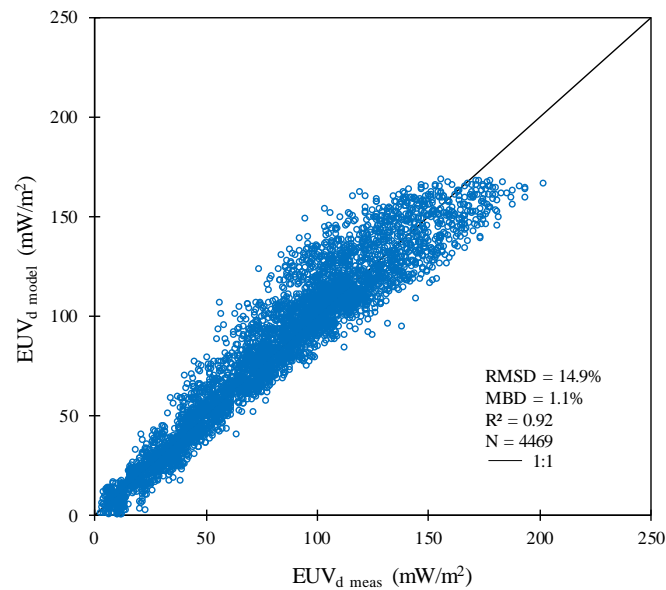


Figure 3 Comparison between diffuse EUV solar radiation from the model ($EUV_{d\ model}$) and the measurements ($EUV_{d\ meas}$)

Our results show that the models for estimating hourly global EUV and diffuse EUV radiation performed well compared with those from the ground-based measurements. In addition, the RMSD, and MBD are in acceptable ranges for the hourly data. The proposed model for calculating global EUV can be compared to the model reported by Bilbao et al. (2015) for estimating global EUV radiation under cloudless conditions in the Marsaxlokk (Malta) campaign having low aerosol loads. Only two input data were used: solar zenith angle and total column ozone. The coefficients of the model were adjusted using our dataset to test the performance of Bilbao's model in our region. The differences in terms of RMSD and MBD between the global EUV obtained from the Bilbao's model and those from the measurement were 23.4% and -7.2% , respectively: These values are higher than those from our models. Therefore, the models proposed in the present study are recommended for the Thai region that has high aerosol loads.

4. Conclusion

In this research, empirical models were developed to calculate the global and diffuse EUV solar radiation under clear sky conditions using total ozone column, AOD at 340 nm, and air mass. The results show that the global and diffuse EUV solar radiation from the models and the measurement are consistent with RMSD of 15.8% and 14.9%, respectively, and MBD of -5.5% and 1.1% , respectively. Our findings show that these models can be used to calculate global and diffuse EUV solar radiation in tropical regions as in Thailand.

Acknowledgements

The authors would like to thank the Meteorological Department of Thailand at Chiang Mai, Ubon Ratchathani, and Songkhla for the maintenance of our instruments at the sites. The authors are also grateful to the AERONET team for providing aerosol data.

References

- Bilbao, J., Roman, R., Yousif, C., Mateos, D., and de Miguel, A. (2015). UV and global irradiance measurements and analysis during the Marsaxlokk (Malta) campaign. *Advances in Science and Research*, 12(1), 147-155.
- Grant, R.H., and Gao, W. (2003). Diffuse fraction of UV radiation under partly cloudy skies as defined by the Automated Surface Observation System (ASOS). *Journal of Geophysical Research: Atmospheres*, 108, 4046.
- Gueymard, C. (1993). Critical analysis and performance assessment of clear sky solar irradiance models using theoretical and measured data. *Solar Energy*, 51(2), 121-138.
- Janjai, S., Nuñez, M., Masiri, I., Wattan, R., Buntoung, S., Jantarach, T., and Promsen, W. (2012). Aerosol Optical Properties at Four Sites in Thailand. *Atmospheric and Climate Sciences*, 2, 441-453.
- Kasten, F. (1965). A new table and approximate formula for relative optical air mass. *Archiv fur Meteorologie, Geophysik und Bioklimatologie, Serie B*, 14(2), 206-223.

Lunde, P.J. (1980). Solar Thermal Engineering: Space heating and hot water systems, Wiley, Hudson.

Webb, A., Gröbner, J., and Blumthaler, M. (2006). COST-726: A practical guide to operating broadband instruments measuring erythemally weighted irradiance, EU publications office. No. EUR22595.



Appendix 4

Accurate surface ultraviolet radiation forecasting for clinical application with deep neural network⁴

Study of surface UV radiation in Thailand showed that this region has sufficient UV radiation, indicating that heliotherapy is a promising treatment alternative for skin patients in the country. This work developed a deep learning model for surface UV radiation forecasting. The details are described as follows.

1. Measurement, Methods and Data

Surface UV and weather data acquisition

Surface UV radiation, total ozone column, cloud coverage, and aerosol optical depth at 500 nm (AOD500), were collected at the Faculty of Science, Silpakorn University, Nakhon Pathom, Thailand (13.82°N, 100.04°E) from January 2009 to May 2019. UV intensity was measured every 10 min from 5AM to 7PM at 1-nm wavelength interval from 280 to 400 nm in mW/m² unit using a DMc150 double monochromator (Bentham Instruments, Berkshire, UK). AOD500 and cloud coverage data were collected from 6 AM to 6 PM from January 2011 to December 2018. Hourly AOD500 data were measured by a ground based CE318 sunphotometer (Cimel Electronique, Paris, France) and calibrated by the Aerosol Robotic Network (NASA, Washington, DC, USA). Cloud coverage data were estimated on a 0–10 scale from recorded images of the sky every hour through a PSV-100 skyview instrument (Prede Company, Tokyo, Japan). Total ozone column data were measured daily in Dobson unit (DU) via an OMI/Aura satellite (NASA, Washington, DC, USA) from January 2011 to December 2019. The distributions of UV radiation, cloud, ozone and AOD500 in Nakhon Pathom throughout the year are shown in Fig. 1a–d, respectively.

Hourly downward surface UV radiation in J/m², total ozone column in kg/m², and mid cloud coverage were also downloaded from ERA5 (1) for London, England (51.5°N, 0°E) and Tokyo, Japan (35.75°N, 139.75°E) from 5AM to 7PM from January 2011 to December 2019. It should be noted that ERA5 datasets were generated from a

⁴ The part of this appendix has been published in Scientific Report (2021) Vol.11 No.1.

combination of actual observation (every 3-h) and computational reanalysis. ERA5 downward UV radiation data cover the 200–440 nm wavelength range.

Data cleaning and preprocessing.

Surface UV radiation exhibits an annual seasonal pattern. We used this pattern as a justification for using UV data of the same dates from adjacent years to impute each missing data point. This is crucial because missing UV data often arise from sensor malfunction which typically spans multiple days. Also, because the artificial neural network model cannot handle missing values, imputation increases the number of data points that can be used to train and test the model. Specifically, we impute each missing data point with the average UV radiation from adjacent 10-min time steps, the same time steps from adjacent days, and the same dates from adjacent years. The ranges of adjacent time steps, days, and years that were used for imputation are 2, 5, and 2, respectively. Imputed data were visually inspected to ensure that the overall UV intensity follows the expected bell-shape pattern with a peak at around noon. In Thailand, this bell-shape pattern is often observed from October to January where there are few rainy and cloudy days. The Nakhon Pathom UV data from 2014 were excluded from further considerations as there is a technical problem with the instrument.

Nakhon Pathom UV data were split into a training set (2009–2017), for optimizing the parameters of artificial neural network models, a validation set (2018), for determining when to stop the optimization process, and a test set (2019), for evaluating the performance of the final models. We found that using the whole training set, i.e., using UV data from all dates and times, to train the models yielded the best performance. For the validation and test sets, we further exclude data from days with anomalous UV intensity profiles to prevent them from influencing the evaluation of the models. Specifically, we removed data from days whose UV profiles are highly skewed (absolute skewness greater than 0.3), disproportional (ratio between maximal and minimal irradiances greater than 15), or out of expected range (maximal irradiance above 400 or below 150 mW/m²). The distributions of cloud coverage in the validation and test datasets are shown in Fig. 1e and f, respectively. Finally, the antipsoriatic

irradiance at each time point was calculated from 280 to 400 nm UV data based on published psoriasis clearance action spectrum formula (2, 3).

For evaluating the impact of incorporating ozone and AOD500 information as input into SurfUVNet, because these data were available only up to 2018, we re-split the dataset by setting data from 2009 to 2016 as the training set, data from 2017 as the validation set, and data from 2018 as the test set. The same quality filter for excluding data from days with poor UV profiles defined above was also applied to these validation and test sets. SurfUVNet model variants with and without ozone and AOD500 as input were then trained and evaluated together on this data split.

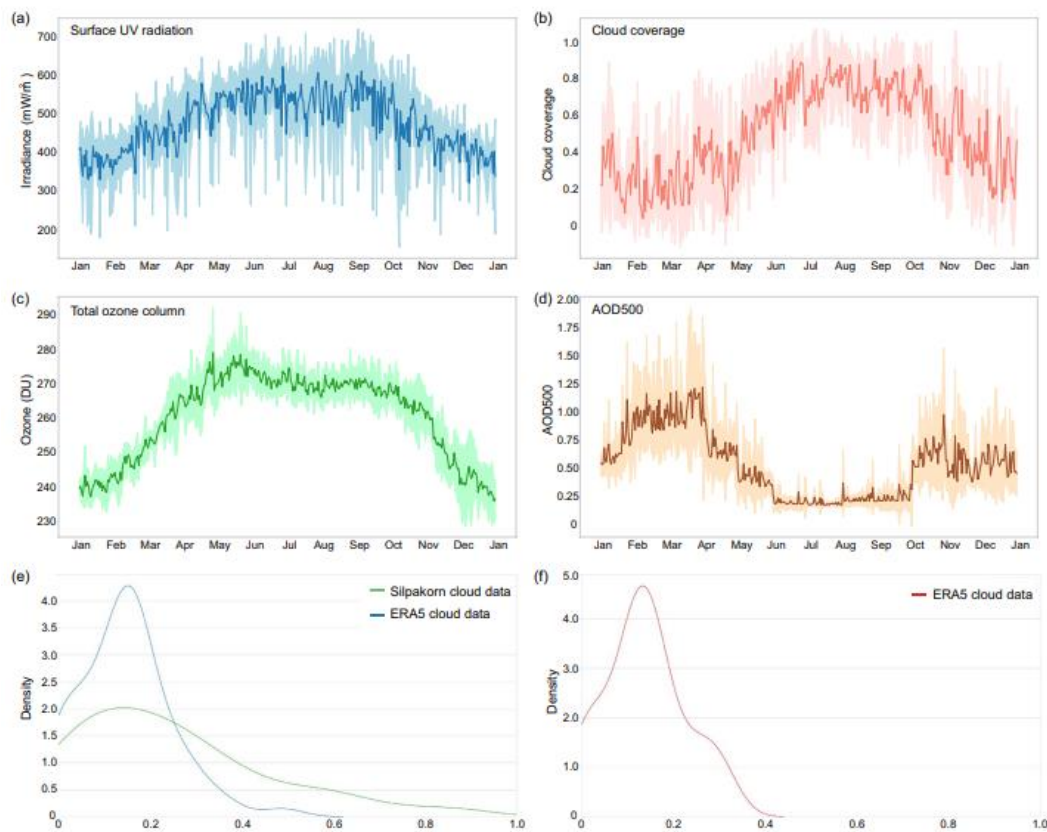


Figure 1. Characteristics of UV and weather conditions at Nakhon Pathom, Thailand. Daily maximums are shown for UV irradiance, total ozone column, and AOD500. Daily averages are shown for cloud coverage. Dark lines indicate the average across 2009–2017. Shaded areas indicate the ± 1 standard deviation range. (a) Annual surface UV irradiance. (b) Annual cloud coverage. (c) Annual total ozone column. (d) Annual AOD500. (e) The distribution of cloud coverage in the validation set (UV data from year 2018). Both Silpakorn University’s observations and ERA5 data were shown. (f) The distribution of cloud coverage in test set (UV data from year 2019). Information from Silpakorn University is unavailable.

SurfUVNet model architecture.

Encoder–decoder-based model is a kind of deep learning model that have been successfully applied to various applications such as image captioning (4) and machine translation. In the context of UV forecasting, an encoder–decoder model can be used to translate a sequence of past observed UV radiations into a sequence of future UV radiations. The model consists of two parts: encoder and decoder as shown in Fig. 2a. Both parts consist of multilayered LSTMs. As the names implied, the LSTMs in the encoder are used for encoding information from the input sequence while the LSTMs in the decoder decoded that information to generate the output sequence.

As the input to our model, for the main implementation which relies only on UV data, we use a sequence of 10-min interval antipsoriatic data from the previous days, denoted as $[A_1, A_2, \dots, A_i]$ and a sequence of antipsoriatic data from the previous year, denoted as $[B_1, B_2, \dots, B_i]$. For the model variant which also accepts AOD500 and ozone, the inputs A_i 's and B_i 's will include these data of the same time-of-day from previous days and previous year as well. To handle differences in data resolution for various features (10-min for UV irradiance, hourly for AOD500, and daily for ozone), the values of features with lower resolutions were duplicated to match the highest resolution.

Since the antipsoriatic values are seasonal in nature, we also include day-of-year information as the input by encoding the day-of-year on a circular index defined as:

$$\text{Circular Index Date} = \left[\sin 2\pi \left(\frac{\text{day}}{265} \right), \cos 2\pi \left(\frac{\text{day}}{365} \right) \right] \quad (1)$$

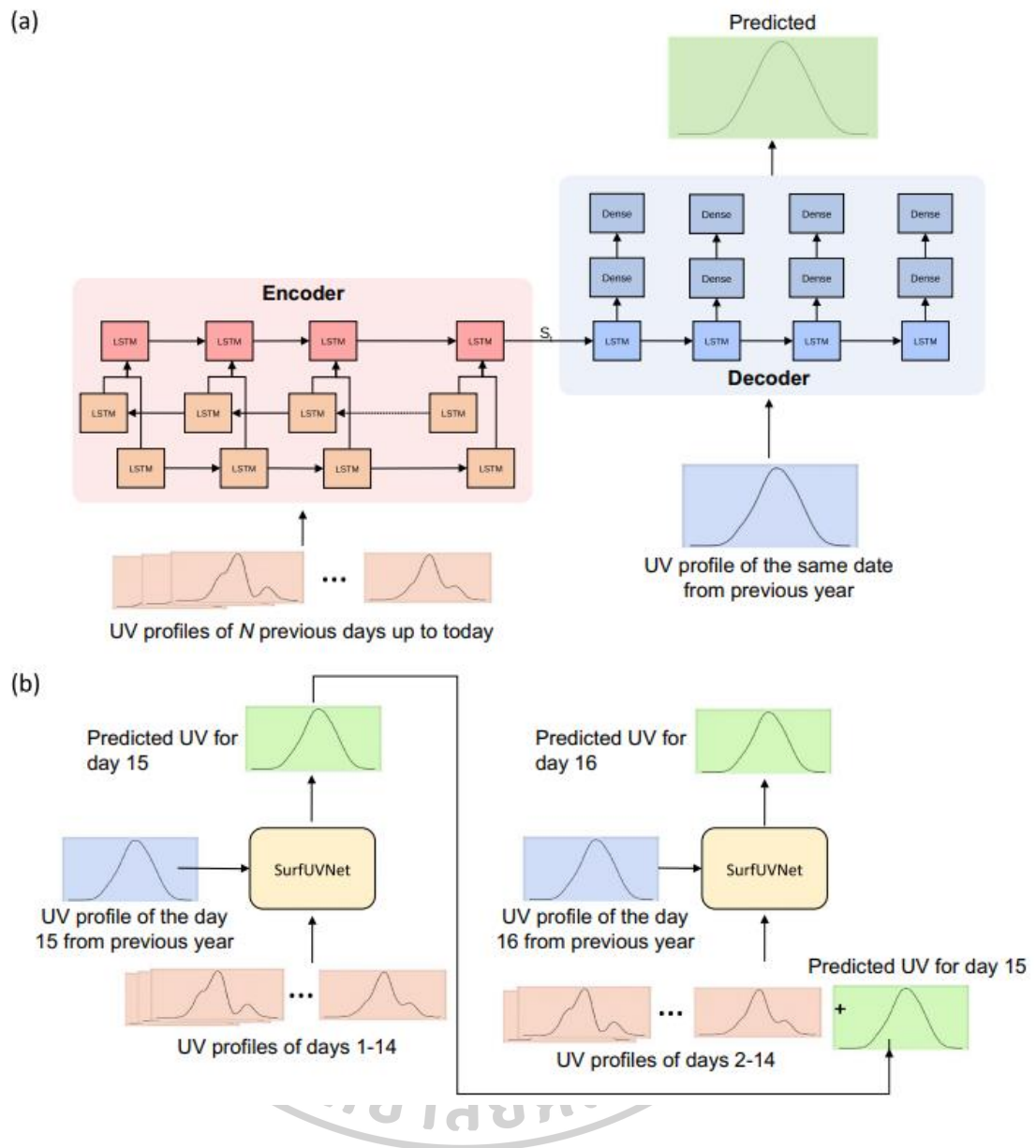


Figure 2. Schematic of SurfUVNet. (a) The underlying encoder–decoder neural network architecture showing the flow of data from the encoder to the decoder via the central connection denoted by S_t . LSTM and Dense indicates the Long Short-Term Memory and fully connected neural network layers, respectively. UV data from days prior to the forecast date are fed into the encoder part while UV data from the same date of previous year are fed into the decoder part. The model forecasts next-day UV radiation at 10-min resolution. (b) The autorecursive mode for long-term UV forecasting. To forecast UV radiation for the next N days, SurfUVNet first forecast next-day’s UV radiation profile and then uses the prediction as input to forecast UV radiation profile for the day after. This process is repeated until the forecasts for the next N days are generated.

The circular date feature helps the model to learn the seasonal pattern. The model predicts future antipsoriatic values, $[\check{y}_1, \check{y}_2, \dots, \check{y}_t]$

Next, we provide detailed information of our model.

Encoder. The decoder takes the previous day sequence $[A_1, A_2, \dots, A_t]$ and the circular date feature as input. We use a bi-directional (5) LSTM as the first layer to help the model learn the temporal effect in both directions. The latter layers are uni-directional LSTM that will capture the information and pass the information to the decoder via the final cell state, S_t .

Decoder. The decoder takes $[B_1, B_2, \dots, B_t]$ as input and uses it to future predict antipsoriatic values. The first layer of the decoder is a LSTM layer which uses S_t from the decoder as the initial value of the cell state. We also add two fully connected layers with sigmoid activation function with the dropout (6) rate of 0.2 after the LSTM layer for the final output.

Before feeding the input data to the model, we denoised the input antipsoriatic data with the Savitzky–Golay filter (7). Applying the filter, smooth out the input data, removing any possible noise spikes in the data. However, we do not apply this processing to the target output data. If we train the model to predict the denoised data, the model is learning to predict the unrealistic data and will not be able to handle noises in the UV intensities. Ten, we normalized the antipsoriatic data into a range of $[0, 1]$.

We trained the model using quantile loss (8) defined as:

$$LQUANTILE = \frac{1}{N} \sum_{i=1}^N \max(q(\check{y}_i - y_i), (q - 1)(\check{y}_i - y_i)) \quad (2)$$

where y_i is the actual value and \check{y}_i is the predicted value, q is a quantile value which balances the penalties of overestimates and underestimates. If q is more than 0.5, the quantile loss gives more penalty to overestimated predictions and vice versa. In our work, we set q to 0.33 to favor overestimation rather than underestimation because underestimated results can cause sunburn to patients due to a prescribed sunbathing time that is too long.

Model training.

We used Adaptive Moment Estimation (ADAM) (9) as the optimizer. The learning rate was initially set to 0.0005 and iteratively reduced linearly by $1e^{-7}$ per epoch. Models were trained for 2000 epochs with a batch size of 256.

2. Results

SurfUVNet model architecture.

The task of forecasting in general can be formulated as a problem of finding the best approximation for the relationship between past and future observations. For surface UV radiation, which exhibits an annual seasonal pattern, the profile of next-day UV radiation can be modeled using not only data from previous days but also data from previous years. Here, we adapted an encoder–decoder architecture, which can effectively capture relationship between sequence data, to develop an artificial neural network model for forecasting next-day surface UV radiation. Our model, named SurfUVNet, takes in UV radiation profiles of the past 7, 14, or 21 days through the encoder and passes the encoded information to the decoder. The decoder then takes in the UV radiation profile of the same date as the next day but from last year, combines it with information from the encoder, and then generates the next-day forecast (Fig. 2a). Intuitively, because UV radiation exhibits annual seasonal pattern, our approach models the next-day UV radiation profile as a transformed version of last year’s data and uses recently observed UV pattern to learn the appropriate transformation. Finally, to forecast UV radiation profile further into the future, our approach essentially performs next-day forecast repeatedly via an auto-regressive approach. For example, if we define today as the day N , to predict the UV radiation profile for next week, or day $N+7$, our model first uses data from days $N - 6$, $N - 5$, ..., N to forecast UV for the day $N+1$, and then uses the data from days $N - 5$, $N - 4$, ..., N , and the forecast for the day $N+1$ to forecast UV for the day $N+2$, and so on (Fig. 2b).

Benchmark procedure.

We evaluated the performance of SurfUVNet (also called Seq2Seq-14 here) against four alternative models: a simple model that uses the previous day UV

radiation pattern as the prediction, an empirical approach that combined physics knowledge to define the interactions between UV-related factors with regression technique to learn coefficient values, which is currently in used by the Tai Meteorological Department, a CNN-LSTM neural network model developed for solar power forecasting, and an implementation of bidirectional GRU neural network model which is often used in time series forecasting applications. As prior study has shown that the CNN-LSTM model benefits from additional smoothing of UV data from rainy days²⁷, we considered two CNN-LSTM model implementations: one without smoothing and one with Savitzky–Golay filter (2) (denoted by CNN-LSTM and CNN-LSTM-SG in Fig. 3a and Table 1). To fairly compare model performance, the validation and test datasets were subjected to quality filtering to remove days with highly skewed and out-of-range UV irradiance values (see “Methods” section) where all models are expected to perform poorly on. However, it should be noted that this does not mean that our validation and test sets consist of only clear-sky data. The distribution of cloud coverage shows that both datasets contain many days with cloud coverage above 0.2 and up to 0.4 or more (Fig. 1e and f).

Next-day antipsoriatic irradiance forecast for Nakhon Pathom dataset.

All artificial neural network models were trained using the same UV data from 2011 to 2017 and evaluated on the same UV data from 2018 and 2019 while the regression model based on Earth–Sun distance and total ozone column was fit to UV and ozone data of the same year. All models were trained to forecast next-day antipsoriatic irradiance at 10-min resolution. Furthermore, as past UV radiation profile is a critical input data for artificial neural network models, we tried inputting data from 7, 14, or 21 days prior to the forecast date to explore whether the models benefit from seeing data from more distant past

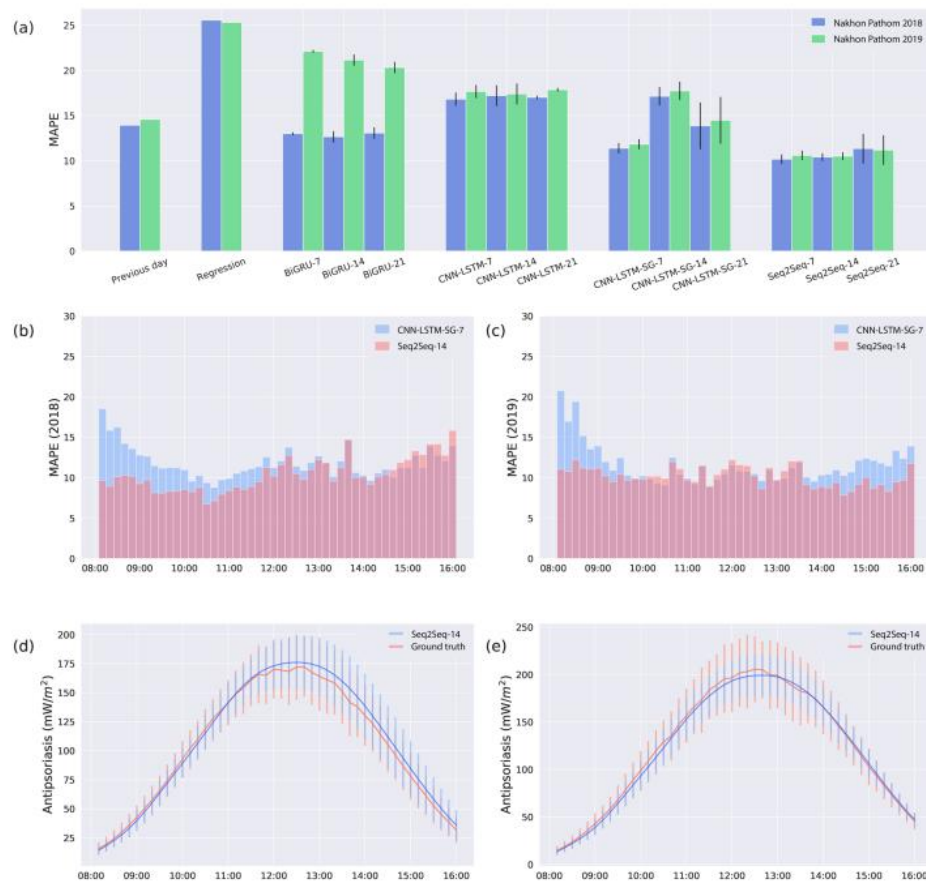


Figure 3. SurfUVNet accurately forecast antipsoriatic irradiance throughout the day. Results on Nakhon Pathom dataset were shown. (a) Comparison of the mean absolute percentage errors (MAPE) for the next-day antipsoriatic irradiance forecast between SurfUVNet (Seq2Seq-14) and four benchmark models (see “Methods” section). Previous day model simply predicts next-day’s UV radiation to be the same as today’s. Regression model refers to the regression model based on Earth–Sun distance and total ozone column currently in used by the Thai Meteorological Department. BiGRU is an artificial neural network architecture that is often utilized for time series forecasting. CNN-LSTM, and CNN-LSTM-SG are artificial neural network models that were recently applied to UV forecasting in the energy domain. The tags – 7, – 14, and – 21 designate the length of UV data, in days prior to the forecast date, that were input into each model. (b) Distribution of MAPE for the validation set (UV data from 2018) throughout the times of the day. Results for the best performing models, namely CNN-LSTM-SG-7 and SurfUVNet (Seq2Seq-14), are shown. (c) A similar plot showing distribution of MAPE for the test set (UV data from 2019). (d) Comparison of ground truth UV data and forecasts made by SurfUVNet for the validation set (UV data from 2018). Error bars indicate one-standard deviation ranges. (e) A similar plot for the test set (UV data from 2019).

Overall, SurfUVNet achieves the best next-day forecasting performance with mean absolute percentage errors (MAPE) of 10.41 and 10.51 on the validation and test sets, respectively (Seq2Seq models in Fig. 3a and Table 1). It should be noted that while the CNN-LSTM-SG model can also reach similar levels of performance (MAPE of 11.39 and 11.84), it is highly sensitive to the length of input UV data. Changing the length of input UV data from 7 days to 14 or 21 days significantly raises the MAPE of CNN-LSTM-SG models to 13.87–17.74. In contrast, the performance of SurfUVNet is stable with respect to the length of the input. Furthermore, SurfUVNet achieves consistent forecasting accuracy throughout the day while the CNN-LSTM-SG model produce significantly higher forecast error during the morning and afternoon hours (8AM–9AM and 2PM–4PM) compared to the middle of the day (Fig. 3b and c). Lastly, comparison of ground truth antipsoriatic irradiance and SurfUVNet’s forecast confirmed that SurfUVNet’s prediction closely mimics the expected bell-shaped pattern of daily UV radiation in both validation and test sets (Fig. 3d and e)

Table 1. Mean absolute percentage errors (MAPE) of the next-day antipsoriatic irradiance forecasting produced by SurfUVNet and benchmark models on Nakhon Pathom dataset.

Model	Number of parameters	Validation set MAPE (2018, 8AM–4PM)	Test set MAPE (2019, 8AM–4PM)
Previous day model	–	13.93	14.58
Regression model based on Earth–Sun distance and total ozone column ²³	6	25.57	25.32
BiGRU-7	39,165,013	13.00 ± 0.16 ^b	22.12 ± 0.33
BiGRU-14	78,158,933	12.66 ± 0.62	21.15 ± 1.20
BiGRU-21	117,152,853	13.07 ± 0.63	20.33 ± 0.47
CNN-LSTM-7 ²⁷	178,077	16.82 ± 0.73	17.67 ± 0.91
CNN-LSTM-14 ²⁷		17.21 ± 1.15	17.40 ± 0.44
CNN-LSTM-21 ²⁷		17.02 ± 0.20	17.87 ± 0.24
CNN-LSTM-SG-7		11.39 ± 0.57	11.84 ± 0.63
CNN-LSTM-SG-14		17.14 ± 1.01	17.74 ± 0.70
CNN-LSTM-SG-21		13.87 ± 2.59	14.48 ± 1.96
Seq2Seq-7	1,627,393	10.18 ± 0.53	10.60 ± 0.34
Seq2Seq-14 (SurfUVNet)		10.41 ± 0.43	10.51 ± 0.41
Seq2Seq-21		11.35 ± 1.64	11.19 ± 0.33

Table 2. Mean absolute percentage errors (MAPE) of the next-day antipsoriatic irradiance forecasting produced by SurfUVNet and other models on the ERA5 Tokyo and London datasets.

Model	Tokyo		London	
	Validation set MAPE (2018, 8AM–4PM)	Test set MAPE (2019, 8AM–4PM)	Validation set MAPE (2018, 8AM–4PM)	Test set MAPE (2019, 8AM–4PM)
Previous day model	21.78	35.50	18.14	43.57
Regression model based on Earth–Sun distance and total ozone column ²²	16.68	16.52	18.68	19.17
CNN-LSTM-SG-7	14.75 ± 0.41	15.77 ± 0.33	13.14 ± 0.35	16.27 ± 0.54
CNN-LSTM-SG-14	13.18 ± 0.28	14.99 ± 0.51	12.19 ± 0.19	17.78 ± 0.19
Seq2Seq-14 (SurfUVNet)	11.83 ± 0.44	12.72 ± 0.67	11.54 ± 0.50	17.74 ± 0.19

Next-day downward solar UV irradiance forecast for Tokyo and London datasets.

All models were further evaluated on hourly downward solar UV irradiance data obtained from ERA5 for Tokyo, Japan and London, England, which represent different weather regimes from Thailand's. In contrast to the seasonal cloud coverage pattern at Nakhon Pathom (Fig. 1b), cloud coverage for Tokyo and London fluctuates around 0.2–0.4 year-round. Furthermore, day-to-day variation in UV radiation profiles are much higher in Tokyo and London compared to Nakhon Pathom, as indicated by much higher MAPE between today's and the next day's UV profiles (Tables 1 and 2, 21.78–35.50 for Tokyo, 18.14–43.57 for London, and 13.93–14.58 for Nakhon Pathom). Overall, SurfUVNet performs competitively, achieving MAPE of 12.72 and 17.74 for the next-day forecast for Tokyo and London datasets, respectively (Table 2). The regression model based on Earth–Sun distance and total ozone column performs much better on these datasets than on Nakhon Pathom's (Tables 1 and 2, MAPE of 16.52–19.17 on ERA5 compared to 25.52–25.57 on Nakhon Pathom) and only slightly worse than the artificial neural network approaches. Again, it should be noted that the validation and test sets contain many days with considerable cloud coverage.

Adding weather information does not improve forecasting.

As atmospheric conditions can reflect and scatter UV radiation before it reaches the Earth's surface, we tried incorporating total ozone column, atmospheric aerosol (AOD500), and cloud coverage data into SurfUVNet. However, cloud coverage data contain many missing values that could not be imputed due to the irregularity of the

data and had to be excluded from model development. Instead, we used cloud coverage data to evaluate whether SurfUVNet overestimates the amount of UV radiation when the weather is cloudy. This reveals that SurfUVNet's forecasting errors weakly correlate with cloud condition (Fig. 4, Spearman rank correlation=0.16776, -0.04546, and 0.20229 for Nakhon Pathom,

Tokyo, and London 2019 datasets). For Nakhon Pathom dataset, SurfUVNet's forecast error stays roughly the same before shifting upward when cloud coverage goes above 0.7 (Fig. 4a). For Tokyo dataset, SurfUVNet's error is not correlated with cloud coverage at all (Fig. 4b). SurfUVNet's error shows the clearest correlation with cloud coverage in London dataset (Fig. 4c). Addition of ozone and AOD500 data into SurfUVNet does not improve the performance of the base model that utilizes only UV data (Supplementary Figure 3). The model with ozone and AOD500 data achieves MAPE of 15.33 on the validation set (data from 2017) and MAPE of 13.91 on the test set (data from 2018), while the base model achieves MAPE of 14.32 and 13.60, respectively. This may be because ozone and AOD500 data were collected at lower frequency (hourly vs every 10 min) and at a shorter time period during the day (6AM–6PM vs 5AM–7PM) than UV data. Although data from the early morning and late evening hours where the amount of UV radiation is almost nonexistent should not contribute much to the forecasting of UV radiation during daylight hours, we found that withholding UV data from 6AM to 8AM and 4PM to 6PM from the model slightly raises error from 10.51 to 11.78 MAPE (Wilcoxon signed rank test result is not significant with p value=0.5567). Lastly, to evaluate the impact of uncertainty of next-day ozone and AOD500 on the forecast performance, a variant of SurfUVNet was trained with the actual values of next-day ozone and AOD500. This does not reduce the forecast error (MAPE of 15.70 and 15.50 on the validation and test sets, respectively), indicating that the limitation lies elsewhere.

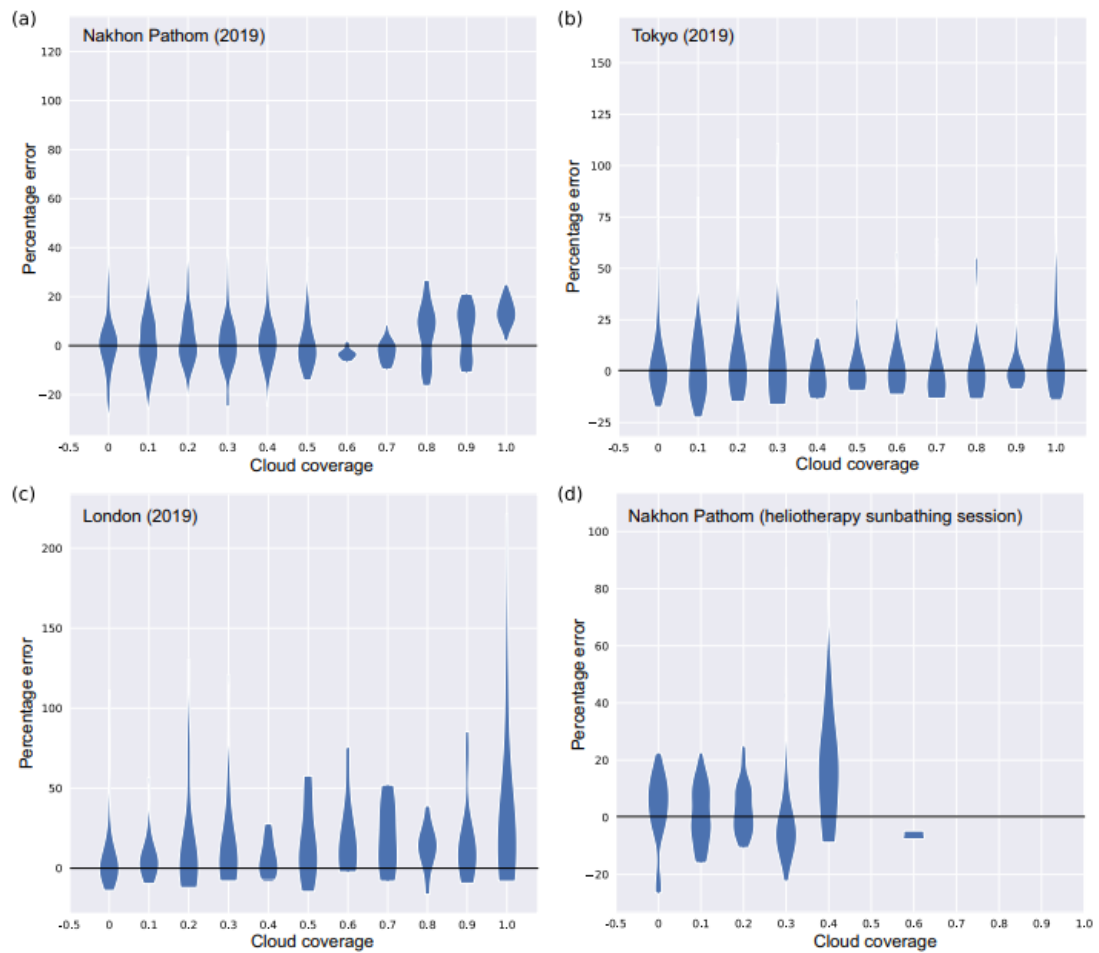


Figure 4. SurfUVNet's forecast error weakly correlates with cloud coverage. Violin plots showing the distribution of SurfUVNet's forecast error in 1-h interval with various cloud coverage. Errors on the test sets (UV data from year 2019) are shown. (a) Nakhon Pathom dataset. (b) Tokyo dataset. (c) London dataset. (d) Heliotherapy sunbathing sessions planned by photodermatologist at King Chulalongkorn Memorial Hospital. Each data point that constitutes the violin plots correspond to the error between predicted and actual antipsoriatic irradiances that a patient would be exposed to if he or she were to sunbath according to dermatologist's planning.

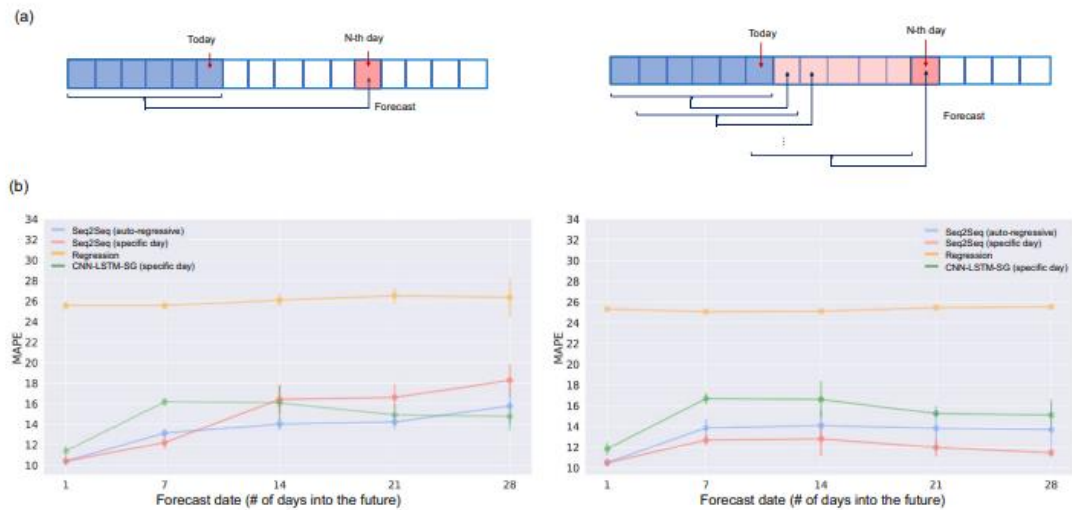


Figure 5. Long-term antipsoriatic irradiance forecasting. Results on Nakhon Pathom dataset were shown. (a) Diagram of two approaches for making long-term forecast: developing specific artificial neural network model for making forecast for a specific day that is a certain number of days into the future (left) and autoregressively using the next-day forecast as input for making forecast for the day after that (right). (b) Long-term antipsoriatic irradiance forecasting performance for up to 28 days into the future on the validation set (UV data from 2018) and the test set (UV data from 2019). Performance for SurfUVNet, the regression model based on Earth–Sun distance and total ozone column, and the best CNN-LSTM models were shown.

Long-term antipsoriatic irradiance forecasting.

Long-term UV forecasting is essential for heliotherapy applications as it allows clinicians and patients to plan sunbathing schedule in advance and make necessary adjustments to the schedule to achieve the desire UV radiation dosage. We explored two approaches for forecasting antipsoriatic irradiance for up to a month into the future (Fig. 5a). The first approach is to train a collection of artificial neural network models, each making the forecast for a specific date that is a certain number of days into the future. In other words, we trained one model for making the next-day forecast, one model for making the forecast for the day after that, and so on. The second approach is to train a single model for making the next day forecast and then autoregressively use the next-day forecast as in input to make the forecast for the day after that. Evaluation on Nakhon Pathom 2018–2019 UV datasets showed that the performance of the autoregressive approach is quite stable with average MAPE of

13.70–15.79 for forecasting up to 28 days into the future (Table 3 and Fig. 5b). On the other hand, developing specific models for specific days performs well on the 2019 dataset but poorly on the 2018 dataset (MAPE of 11.46 vs 18.38 for forecasting up to 28 days into the future). We also additionally explored the possibility of training a model that can forecast UV profiles of multiple days at once, but the performances were much worse than the two methods described above (MAPE of 29.49 and 49.69 for forecasting the next 7 days at once on the 2018 and 2019 datasets, respectively). Hence, we decided to choose the autoregressive approach for SurfUVNet. It should be noted that the regression approach based on Earth–Sun distance and ozone information performed poorly on Nakhon Pathom’s UV data even for next-day forecast (Table 1, MAPE of 25.32–25.57).

3. Discussion

We have developed SurfUVNet, an artificial neural network model for predicting surface UV radiation that achieves around 10% error for next-day forecast and 13–16% error for 7-day up to 4-week forecast. This affirms that quantitative UV forecast is appropriate for heliotherapy applications, which tolerate up to 10–25% error level. SurfUVNet’s performance is competitive on UV data from multiple regions, Thailand, Japan, and England, and on both antipsoriatic and downward irradiance. Hence, SurfUVNet can be adapted for forecasting other useful UV action spectra such as vitamin D production and erythematous UV index as well. In fact, our model can even be trained to forecast antipsoriatic irradiance from input erythemally-weighted UV data from a UV Biometer instrument with a small performance reduction (data now shown). This capability is necessary for establishing a national heliotherapy network in Thailand because there is only one full-spectrum UV sensor located in the central region of the country while the rest of the country is covered by a network of UV Biometers.

A key limitation of artificial neural network is that it tends to overfit to the training dataset and does not generalize well to other datasets that come from different distributions. In the context of UV forecasting, this dictates that the model must be retrained with data from particular weather station in order to be usable for that geographic region. Indeed, the accuracy of each model varies by 5–6% across the

three geographical regions, Thailand, Japan, and England and even across 2018 and 2019 in the case of London dataset (Tables 1 and 2). For the case of London dataset, comparison of UV profiles between consecutive days in 2019 showed an extremely high average variation of 43.57%. The discrepancy in performance of the regression model based on Earth–Sun distance and total ozone column developed by the Thai Meteorological Department²² between Nakhon Pathom and ERA5 datasets (25% error on Nakhon Pathom and 16–19% error on ERA541 (1) datasets) could be attributed to the fact that ERA5 data, which contain more detailed ozone measurements (hourly compared to daily) and were computationally interpolated, are likely to be more easily fitted by regression.

Table 3. Mean absolute percentage errors (MAPE) for long-term antipsoriatic irradiance forecasting for up to 28 days into the future on Nakhon Pathom dataset.

Model	Target day	Validation set MAPE (2018, 8AM–4PM)	Test set MAPE (2019, 8AM–4PM)
Regression model based on Earth–Sun distance and total ozone column ²²	7	25.57	25.07
	14	26.10	25.11
	21	26.53	25.45
	28	26.37	25.53
CNN-LSTM-SG-7 Forecast specific date	7	16.18 ± 0.42	16.68 ± 0.59
	14	16.09 ± 1.70	16.60 ± 1.77
	21	14.91 ± 1.08	15.24 ± 0.29
	28	14.76 ± 1.39	15.09 ± 1.56
CNN-LSTM-SG-7 Auto-regressive	7	18.56 ± 2.65	17.41 ± 2.70
	14	20.60 ± 2.31	19.49 ± 2.92
	21	22.51 ± 1.97	21.37 ± 1.83
	28	24.45 ± 1.60	22.62 ± 0.98
CNN-LSTM-SG-14 Forecast specific date	7	16.69 ± 0.92	16.73 ± 1.16
	14	14.82 ± 0.63	15.49 ± 1.43
	21	15.96 ± 0.99	16.18 ± 0.46
	28	15.46 ± 0.71	15.55 ± 1.14
CNN-LSTM-SG-14 Auto-regressive	7	17.31 ± 0.45	17.77 ± 0.55
	14	17.20 ± 0.47	19.16 ± 0.65
	21	17.13 ± 0.50	20.71 ± 0.57
	28	17.00 ± 0.50	20.83 ± 0.97
Seq2Seq-14 (SurfUVNet) Forecast specific date	7	12.21 ± 0.65	12.68 ± 0.53
	14	16.42 ± 1.40	12.80 ± 1.64
	21	16.61 ± 1.29	11.97 ± 0.88
	28	18.28 ± 1.57	11.46 ± 0.38
Seq2Seq-14 (SurfUVNet) Auto-regressive	7	13.13 ± 0.41	13.86 ± 0.91
	14	14.03 ± 0.62	14.09 ± 1.49
	21	14.22 ± 0.74	13.83 ± 2.20
	28	15.79 ± 1.90	13.70 ± 2.65

The fact that SurfUVNet's forecast error only weakly correlates with cloud coverage (Fig. 4) is unexpected but may be explained by the fact that cloud coverage in Nakhon Pathom exhibits clear seasonal pattern (Fig. 1b) and that the UV radiation profiles are stable over consecutive days (Table 1, MAPE of 13.94–14.58 for previous day model). On a geographical region with highly variable weather condition, such as London in 2019, artificial neural network models' performance drop significantly (Table 2) and the error of SurfUVNet exhibits higher correlation with cloud coverage (Fig. 4c). Hence, artificial neural network models seem to be able to exploit seasonal weather pattern and day-to-day variation to achieve good performance without relying on explicit cloud coverage information. This capability of the model to extract seasonal patterns may also explain why addition of ozone and AOD500 information did not improve the performance of SurfUVNet (Supplementary Figure 3), particularly as AOD500 level at Nakhon Pathom closely follows the same seasonal pattern as cloud coverage (Fig. 1d).

We explored two approaches for forecasting long-term UV radiation. Initially, we expected that developing a specific model for making the forecast for a specific date a certain number of days into the future would yield better performance than an autoregressive approach which use the next-day forecast as input for making the forecast for the day after because forecasting errors would accumulate through autoregressive steps. However, the models for specific date seem to overfit the training data, performing well on the 2019 dataset but poorly on the 2018 dataset (Table 3, 11.46% vs 18.28% error for forecasting up to 28 days into the future). In contrast, the autoregressive approach performs more consistently (13.70% and 15.79% error). An explanation for the over-fitting of the model trained for specific date may be because the relationship between today's and next week's UV radiation profiles is so weak that the models learn mostly patterns that are specific to the training dataset. The poor performance of models for multi-day forecast (29.49–49.69% error for 7-day forecast) is likely due to the sheer number of outputs that the models must optimize. To make a 7-day forecast at 10-min resolution, the model has to output 595 values. From these results, we recommend the autoregressive approach for making long-term UV forecast with SurfUVNet.

To prospectively examine whether SurfUVNet’s performance is sufficient for heliotherapy applications, we asked photodermatologist at King Chulalongkorn Memorial Hospital to plan a 3-month sunbathing course based on SurfUVNet’s output and then compared their schedule with the ground truth antipsoriatic irradiances of the same time interval. This reveals that the error in antipsoriatic dose that the patient would receive by following the clinician’s sunbathing protocol remains well within the acceptable 10–25% up to 0.3 cloud coverage (Fig. 4d, MAPE of 11.23). A possible solution for accounting for weather effects on UV radiation that we are exploring is to have each patient carry a portable UV sensor or a smartphone equipped with light sensor and use that data to adjust SurfUVNet’s forecast in real-time.

References

1. Hersbach, H., Bell, B., Berrisford, P. et al. ERA5 Hourly Data on Single Levels from 1979 to Present. Copernicus Climate Change Service (C3S) Climate Data Store (CDS) (Accessed on 30/12/2020) (2018).
2. Parrish, J. A. & Jaenicke, K. F. Action spectrum for phototherapy of psoriasis. *J. Investig. Dermatol.* 76(5), 359–362 (1981).
3. Fischer, T., Alsins, J. & Berne, B. Ultraviolet-action spectrum and evaluation of ultraviolet lamps for psoriasis healing. *Int. J. Dermatol.* 23(10), 633–637 (1984).
4. Vinyals, O., Toshev, A., Bengio, S. & Erhan, D. Show and tell: a neural image caption generator. In *Inproceedings* 3156–3164 (2015).
5. Schuster, M. & Paliwal, K. K. Bidirectional recurrent neural networks. *IEEE Trans. Signal Process.* 45(11), 2673–2681 (1997).
6. Srivastava, N., Hinton, G., Krizhevsky, A., Sutskever, I. & Salakhutdinov, R. Dropout: a simple way to prevent neural networks from overfitting. *J. Mach. Learn. Res.* 15(56), 1929–1958 (2014).
7. Savitzky, A. & Golay, M. J. E. Smoothing and differentiation of data by simplified least squares procedures. *Anal. Chem.* 36(8), 1627–1639 (1964).
8. Koenker, R. & Hallock, K. F. Quantile regression. *J. Econ. Perspect.* 15(4), 143–156 (2001).
9. Kingma, D. & Ba, J. Adam: a method for stochastic optimization. In *International Conference on Learning Representations* (2014).

REFERENCES

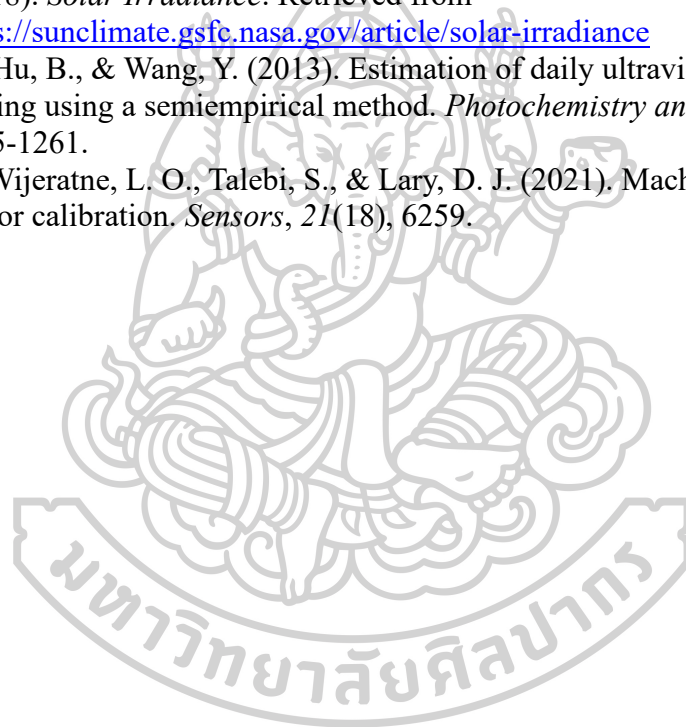
- Antón, M., Serrano, A., Cancillo, M., & García, J. (2009). An empirical model to estimate ultraviolet erythematous transmissivity. *Annales Geophysicae*,
- Barber, K. (2011). *Are the erythema and roughness on a young girl's cheeks treatable?*
- Barbero, F., Lopez, G., & Batlles, F. (2006). Determination of daily solar ultraviolet radiation using statistical models and artificial neural networks. *Annales Geophysicae*,
- Brenner, M., & Hearing, V. J. (2008). The protective role of melanin against UV damage in human skin. *Photochemistry and photobiology*, *84*(3), 539-549.
- Brogniez, C., Doré, J.-F., Auriol, F., Cesarini, P., Minvielle, F., Deroo, C., Catalfamo, M., Metzger, J.-M., & Da Conceicao, P. (2021). Erythematous and vitamin D weighted solar UV dose-rates and doses estimated from measurements in mainland France and on Réunion Island. *Journal of Photochemistry and Photobiology B: Biology*, *225*, 112330.
- Buntoung, S., Janjai, S., Nunez, M., Choosri, P., Pratummasoot, N., & Chiwpreecha, K. (2014). Sensitivity of erythematous UV/global irradiance ratios to atmospheric parameters: application for estimating erythematous radiation at four sites in Thailand. *Atmospheric research*, *149*, 24-34.
- Buntoung, S., Pattarapanitchai, S., Laiwarin, P., Boontaveeyuwat, E., & Janjai, S. (2022). Solar Ultraviolet Radiation for Psoriasis Treatment at Nakhon Pathom Province. *Journal of Applied Research on Science and Technology (JARST)*, *21*(1), 34-43.
- CarbonBrief. (2020). *Liquid and ice*. Retrieved from <https://www.carbonbrief.org/guest-post-how-declining-ice-in-clouds-makes-high-climate-sensitivity-plausible/#:~:text=The%20fraction%20of%20liquid%20droplets,to%20space%20than%20ice%20clouds.>
- Ceamanos, X., Six, B., & Riedi, J. (2021). Quasi-Global Maps of Daily Aerosol Optical Depth From a Ring of Five Geostationary Meteorological Satellites Using AERUS-GEO. *Journal of Geophysical Research: Atmospheres*, *126*(20), e2021JD034906.
- Chapman, S. (1930). XXXV. On ozone and atomic oxygen in the upper atmosphere. *The London, Edinburgh, and Dublin Philosophical Magazine and Journal of Science*, *10*(64), 369-383.
- Choosri, P., Janjai, S., Nunez, M., Buntoung, S., & Chanalert, W. (2017). Development of a method for mapping monthly average hourly diffuse erythematous ultraviolet radiation. *Journal of Atmospheric and Solar-Terrestrial Physics*, *161*, 19-27.
- Costa, A., Meyer, J., Afchine, A., Luebke, A., Günther, G., Dorsey, J. R., Gallagher, M. W., Ehrlich, A., Wendisch, M., & Baumgardner, D. (2017). Classification of Arctic, midlatitude and tropical clouds in the mixed-phase temperature regime. *Atmospheric Chemistry and Physics*, *17*(19), 12219-12238.
- Dissanayake, A., Allnutt, J., & Haidara, F. (2001). Cloud attenuation modelling for SHF and EHF applications. *International journal of satellite communications*, *19*(3), 335-345.
- Earthdata. (2006). Retrieved from https://disc.gsfc.nasa.gov/datasets/OMUVBd_003/summary

- Eck, T., Bhartia, P., & Kerr, J. (1995). Satellite estimation of spectral UVB irradiance using TOMS derived total ozone and UV reflectivity. *Geophysical Research Letters*, 22(5), 611-614.
- eia. (2022). *Is ozone a greenhouse gas?* U.S. Energy Information Administration. Retrieved from <https://www.eia.gov/tools/faqs/faq.php?id=84&t=11#:~:text=Ozone%20is%20technically%20a%20greenhouse,found%20in%20the%20earth's%20atmosphere.>
- EPA. (2021). *Basic Ozone Layer Science*. U.S. Environmental Protection Agency. Retrieved from <https://www.epa.gov/ozone-layer-protection/basic-ozone-layer-science#:~:text=The%20ozone%20layer%20in%20the,that%20has%20several%20harmful%20effects.>
- Ewald, F., Zinner, T., Kölling, T., & Mayer, B. (2019). Remote sensing of cloud droplet radius profiles using solar reflectance from cloud sides—Part 1: Retrieval development and characterization. *Atmospheric Measurement Techniques*, 12(2), 1183-1206.
- FDA. (2020). *Ultraviolet (UV) Radiation*. Retrieved from <https://www.fda.gov/radiation-emitting-products/tanning/ultraviolet-uv-radiation>
- Feister, U., Cabrol, N., & Häder, D. (2015). UV irradiance enhancements by scattering of solar radiation from clouds. *Atmosphere*, 6(8), 1211-1228.
- Foyo-Moreno, I., Alados, I., & Alados-Arboledas, L. (2007). Adaptation of an empirical model for erythemal ultraviolet irradiance. *Annales Geophysicae*,
- Gadhavi, H., Pinker, R., & Laszlo, I. (2008). Estimates of surface ultraviolet radiation over north America using Geostationary Operational Environmental Satellites observations. *Journal of Geophysical Research: Atmospheres*, 113(D21).
- Garcia, P., Benarroch, A., & Riera, J. M. (2008). Spatial distribution of cloud cover. *International Journal of Satellite Communications and Networking*, 26(2), 141-155.
- Gistda. *Data from Satellite and Land-based Sensor*. Retrieved from https://www.gistda.or.th/ewtadmin/ewt/gistda_web/news_view.php?n_id=1544&lang=EN
- GrassrootsHealth. (2021). *Overview of Solar Radiation*. Retrieved from <https://www.grassrootshealth.net/blog/forms-energy-sunshine-may-affect-health/>
- Hönigsmann, H. (2001). Phototherapy for psoriasis. *Clinical and experimental dermatology*, 26(4), 343-350.
- Iqbal, M. (1983). *An Introduction to Solar Radiation*. Elsevier.
- Janjai, S., Buntung, S., Wattan, R., & Masiri, I. (2010). Mapping solar ultraviolet radiation from satellite data in a tropical environment. *Remote Sensing of Environment*, 114(3), 682-691.
- Janjai, S., Kumharn, W., & Laksanaboonsong, J. (2003). Determination of Angstrom's turbidity coefficient over Thailand. *Renewable Energy*, 28(11), 1685-1700.
- Kaskaoutis, D., & Kambezidis, H. (2006). Investigation into the wavelength dependence of the aerosol optical depth in the Athens area. *Quarterly Journal of the Royal Meteorological Society: A journal of the atmospheric sciences, applied meteorology and physical oceanography*, 132(620), 2217-2234.
- Kasten, F. (1965). A new table and approximation formula for the relative optical air mass. *Archiv für Meteorologie, Geophysik und Bioklimatologie, Serie B*, 14, 206-223.

- Kolhe, A. R., Aher, G. R., Soyam, P. S., Ralegankar, S. D., Kedia, S., Chaudhari, L. M., Antad, V. V., Ghude, S. D., Safai, P. D., & Chakane, S. D. (2022). Aerosol Opto-physical Properties: Temporal Variation, Aerosol Type Discrimination and Source Identification. *Aerosol and Air Quality Research*, 22, 220104.
- Krzyściński, J., Jarosławski, J., Rajewska-Więch, B., Sobolewski, P., Narbutt, J., Lesiak, A., Pawlaczyk, M., & Janouch, M. (2012). Space-based estimation of the solar UV-B doses for psoriasis heliotherapy in Poland using OMI data for the period 2005–2011. *Journal of Photochemistry and Photobiology B: Biology*, 117, 240-246.
- Kumar, N., Chu, A., & Foster, A. (2007). An empirical relationship between PM_{2.5} and aerosol optical depth in Delhi Metropolitan. *Atmospheric Environment*, 41(21), 4492-4503.
- Lalic, B., Eitzinger, J., Dalla Marta, A., Orlandini, S., Sremac, A. F., & Pacher, B. (2018). *Agricultural meteorology and climatology* (Vol. 8). Firenze University Press.
- Li, J., Carlson, B. E., Yung, Y. L., Lv, D., Hansen, J., Penner, J. E., Liao, H., Ramaswamy, V., Kahn, R. A., & Zhang, P. (2022). Scattering and absorbing aerosols in the climate system. *Nature Reviews Earth & Environment*, 3(6), 363-379.
- Li, Z., Wang, P., & Cihlar, J. (2000). A simple and efficient method for retrieving surface UV radiation dose rate from satellite. *Journal of Geophysical Research: Atmospheres*, 105(D4), 5027-5036.
- Lightle, K. (2008). *Solar Energy, Albedo, and the Polar Regions*. Retrieved from <https://beyondpenguins.ehe.osu.edu/issue/energy-and-the-polar-environment/solar-energy-albedo-and-the-polar-regions>
- Lindfors, A. V., Kujanpää, J., Kalakoski, N., Heikkilä, A., Lakkala, K., Mielonen, T., Sneep, M., Krotkov, N. A., Arola, A., & Tamminen, J. (2018). The TROPOMI surface UV algorithm. *Atmospheric Measurement Techniques*, 11(2), 997-1008.
- Liu, H., Hu, B., Zhang, L., Zhao, X., Shang, K., Wang, Y., & Wang, J. (2017). Ultraviolet radiation over China: Spatial distribution and trends. *Renewable and Sustainable Energy Reviews*, 76, 1371-1383.
- Lucas, R. M., Gorman, S., Geldenhuys, S., & Hart, P. H. (2014). Vitamin D and immunity. *F1000prime reports*, 6.
- Lui, H., Hu, B., Wang, Y., Liu, G., Tang, L., Ji, D., Bai, Y., Bao, W., Chen, X., & Chen, Y. (2017). Two ultraviolet radiation datasets that cover China. *Advances in Atmospheric Sciences*, 34, 805-815.
- Lunde, P. J. (1980). Solar thermal engineering: space heating and hot water systems.
- Maddodi, N., Jayanthi, A., & Setaluri, V. (2012). Shining light on skin pigmentation: the darker and the brighter side of effects of UV radiation. *Photochemistry and photobiology*, 88(5), 1075-1082.
- Mateos Villán, D., de Miguel Castrillo, A., & Bilbao Santos, J. (2010). Empirical models of UV total radiation and cloud effect study. *International Journal of climatology*, 30(9), 1407-1415.
- Matuszko, D. (2012). Influence of the extent and genera of cloud cover on solar radiation intensity. *International Journal of climatology*, 32(15), 2403-2414.

- McKenzie, R. L., Björn, L. O., Bais, A., & Ilyasd, M. (2003). Changes in biologically active ultraviolet radiation reaching the Earth's surface. *Photochemical & Photobiological Sciences*, 2(1), 5-15.
- McKinlay, F., & Diffey, B. (1987). A reference spectrum for ultraviolet induced erythema in human skin 83-87. *Human Exposure to Ultraviolet Radiation*.
- Meerkötter, R., Erbertseder, T., Kammann, J., Blumenthal, R., Flore, F., Simeone, E., Licitra, G., & Tanskanen, A. (2006). The UV service of the ESA-GSE Project PROMOTE. Remote Sensing of Clouds and the Atmosphere XI,
- Miyauchi, M., & Nakajima, H. (2016). Determining an effective UV radiation exposure time for vitamin D synthesis in the skin without risk to health: simplified estimations from UV observations. *Photochemistry and photobiology*, 92(6), 863-869.
- Mostafa, W. Z., & Hegazy, R. A. (2015). Vitamin D and the skin: Focus on a complex relationship: A review. *Journal of advanced research*, 6(6), 793-804.
- NOAA. (2023). *How Do Clouds Affect Solar Energy?* Retrieved from <https://scijinks.gov/solar-energy-and-clouds/>
- Oh, S.-T., Park, D.-H., & Lim, J.-H. (2019). Designing safe general LED lighting that provides the UVB benefits of sunlight. *Applied Sciences*, 9(5), 826.
- Panwar, R. S. (2021). *Types of Orbits*. Retrieved from <https://futurewars.rspanwar.net/indias-space-programme-spacecraft-launchers-and-exploration/>
- Schlundt, C., Kokhanovsky, A., von Hoyningen-Huene, W., Dinter, T., Istomina, L., & Burrows, J. (2011). Synergetic cloud fraction determination for SCIAMACHY using MERIS. *Atmospheric Measurement Techniques*, 4(2), 319-337.
- Siani, A. M., Modesti, S., Casale, G. R., Diemoz, H., & Colosimo, A. (2013). Biologically effective surface UV climatology at Rome and Aosta, Italy. AIP Conference Proceedings,
- Solano, F. (2020). Photoprotection and skin pigmentation: Melanin-related molecules and some other new agents obtained from natural sources. *Molecules*, 25(7), 1537.
- Spencer, A. J. (1971). Part III. Theory of invariants. *Continuum physics*, 1, 239-353.
- Stopelli, E., Conen, F., Morris, C. E., Herrmann, E., Bukowiecki, N., & Alewell, C. (2015). Ice nucleation active particles are efficiently removed by precipitating clouds. *Scientific reports*, 5(1), 16433.
- Tanskanen, A., Krotkov, N. A., Herman, J. R., & Arola, A. (2006). Surface ultraviolet irradiance from OMI. *IEEE transactions on Geoscience and Remote Sensing*, 44(5), 1267-1271.
- TEMIS. (2023). *Yesterday's UV dose and archives*. Retrieved from <https://www.temis.nl/uvradiation/UVdose.php>
- Terenetskaya, I., Bouillon, R., Eisman, J., Garabedian, M., Holick, M., Kleinschmidt, J., Suda, T., Terenetskaya, I., & Webb, A. (2006). *Action Spectrum for the Production of Pre-Vitamin D in Human Skin*. I. C. o. Illumination.
- Tzoumanikas, P., Nikitidou, E., Bais, A., & Kazantzidis, A. (2016). The effect of clouds on surface solar irradiance, based on data from an all-sky imaging system. *Renewable Energy*, 95, 314-322.

- Verdebout, J. (2000). A method to generate surface UV radiation maps over Europe using GOME, Meteosat, and ancillary geophysical data. *Journal of Geophysical Research: Atmospheres*, 105(D4), 5049-5058.
- Waikato. (2007). *Radiation*. Retrieved from <https://www.sciencelearn.org.nz/resources/998-radiation>
- Waikato. (2018). *The electromagnetic spectrum*. Retrieved from https://www.sciencelearn.org.nz/image_maps/63-the-electromagnetic-spectrum
- Webb, A., Gröbner, J., & Blumthaler, M. (2006). *A practical guide to operating broadband instruments measuring erythemally weighted irradiance*. EUR-OP.
- Wikipedia. (2023a). *Aura (satellite)*. Retrieved from https://en.wikipedia.org/wiki/Aura_%28satellite%29
- Wikipedia. (2023b). *Himawari 8*. Retrieved from https://en.wikipedia.org/wiki/Himawari_8
- Wu, D. (2018). *Solar Irradiance*. Retrieved from <https://sunclimate.gsfc.nasa.gov/article/solar-irradiance>
- Zhang, X., Hu, B., & Wang, Y. (2013). Estimation of daily ultraviolet radiation in Beijing using a semiempirical method. *Photochemistry and photobiology*, 89(5), 1255-1261.
- Zhang, Y., Wijeratne, L. O., Talebi, S., & Lary, D. J. (2021). Machine learning for light sensor calibration. *Sensors*, 21(18), 6259.





VITA

NAME PRADTHANA LAIWARIN

DATE OF BIRTH 6 July 1994

PLACE OF BIRTH Nakhon Pathom

INSTITUTIONS ATTENDED 2016 B.Sc. (Physics) Silpakorn University, Thailand
2019 M.Sc. (Physics) Silpakorn University, Thailand

HOME ADDRESS 95 Moo 4, Tha Kham, Sam Phran District
Nakhon Pathom 73110, Thailand

PUBLICATION

1. Raksasat, R., Sri-iesaranusorn, P., Pemcharoen, J., Laiwarin, P., Buntoung, S., Janjai, S., Boontaveeyuwat, E., Asawanonda, P., Sriswasdi S. and Chuangsuwaniche, E. (2021). Accurate surface ultraviolet radiation forecasting for clinical applications with deep neural network. *Scientific Reports*, 11(1), 1-12.
2. Buntoung, S., Pattarapanitchai, S., Laiwarin, P., Boontaveeyuwat, E. and Janjai, S. (2022). Solar ultraviolet radiation for psoriasis treatment at Nakhon Pathom province. *Journal of Applied Research on Science and Technology (JARST)*, 21(1), 34-43.
3. Laiwarin, P., Buntoung, S., Wattan, R. and Janjai, S. (2023). A model for estimating solar ultraviolet radiation for vitamin D photosynthesis. *Journal of Physics Conference Series*, (Vol.2431, No.1, p.012009). IOP Publishing.